Top quark measurements and calibration of the Soft Muon Tagger using the ATLAS detector at the Large Hadron Collider.

Jacobo Ezequiel Blanco

Department of Physics

Royal Holloway, University of London

A thesis submitted to the University of London for the degree of Doctor of Philosophy

April 9, 2015

Declaration of Authorship

I, Jacobo Ezequiel Blanco, hereby declare that this thesis and the work presented in it is entirely my own. Where I have consulted the work of others this is always stated.

Signed: _____

Date: _____

Abstract

This thesis presents top quark measurements where b-jets are identified by searching for "soft" muons produced within them. This method, a form of soft muon tagging, discriminates between b-jets and jets from other quark types, by using the quality of the match (χ^2_{match}) between the muon tracks recorded in the inner detector and muon system of the ATLAS detector. The data/MC efficiency scale factor is obtained on ATLAS data at $\sqrt{s} = 8\,\text{TeV}$ using a tag and probe method on muons from J/ψ decays. The number of muons which are selected by the χ^2_{match}-tagger is obtained from a fit to the invariant mass of the pair. A measurement of the top quark pair production in the lepton plus jets channel using the soft muon tagger on ATLAS data at $\sqrt{s} = 7\,\text{TeV}$ is presented. The multijet background component was estimated using data-driven methods known as the matrix method and the ABCD method. The measured cross section is in good agreement with theoretical calculations and other measurements from ATLAS and CMS. The final measured cross section is:

$$\sigma_{t\bar{t}} = 165 \pm 2\,(\text{stat.}) \pm 17\,(\text{syst.}) \pm 3\,(\text{lumi.})\,\text{pb}$$

The viability of using the χ^2_{match}-based soft muon tagger in the search for boosted resonant production of $t\bar{t}$ pairs via the theoretical Z' boson is also presented. Due to the large boost in the event, the products of the top quarks merge in a collimated cone. The performance of the χ^2_{match}-tagger in identifying the W muon and as a b-tagger is tested. It is found that the tagger provides an additional acceptance to the W muon of $8\,\%$ over the current method known as mini-isolation. As a b-tagger the χ^2_{match}-tagger adds an extra $12\,\%$ more b-jets when compared to using the MV1 tagger only.

Acknowledgements

This thesis is the culmination of a few dozen people pushing a single person to the finish line. Here I name a few of my fellow backers. Firstly, I would like to thank my supervisor Dr. Veronique Boisvert for her support and guidance during tough times. To my fellow PhD students: Dan Hayden, Neil Cooper-Smith, Liam Duguid, Robert Cantrill, Matthew Rose, and Tim Brooks, thank you for sharing your wisdom and more importantly for making the office a wonderful place to work. To the other members of the ATLAS group and the JAI who have at one time or another given me advice, thank you for making me feel like part of the team. A massive thank you must go to my brothers, sisters-in-law, and nephews for all of their support and personal guidance during trying times, and their positive and loud nature during happy times. Para mis padres, Ana y Mario Blanco, no hay palabras para describir la magnitud del apoyo que me habeis dado. No hubiera podido hacer nada sin ustedes. Desde el fondo de mi corazon, los quiero mucho. Sin duda tengo los mejores padres que un hijo puede pedir. Last but not least, I want to thank my wonderful partner Ashton "Boo Face" Turnbull for your relentless belief in me, even when I did not believe in myself. Not a single page of this thesis would have existed if it wasn't for you. Thank you, I love you. To everybody, I am finally done.

Preface

This thesis describes various top measurements performed using a novel method, referred to as *soft muon tagging* (SMT), for identifying the decay of b-quarks by tagging the muons produced from the semileptonic decay of these quarks. The implementation of soft muon tagging used here relies on the quality of the match between tracks in the inner detector and muon systems of the ATLAS detector. In addition, the calibration of this methodology is also described here. Chapter 2 includes an introductory overview of the Standard Model of particle physics. Chapter 3 includes a more detailed description of top quark physics, including the production mechanisms and decay modes; the experimental signature of top events at hadron colliders; and some of the latest results in the field of top quark measurements. Chapter 4 includes: a description of the ATLAS detector and all its components relevant to the study of the top quark, including the inner detector and muon systems. This is followed by an introduction to particle physics event simulation; and object reconstruction techniques used at ATLAS including the SMT tagger in Chapter 5. The measurement of the data/simulation SMT efficiency scale-factor on 2012 ATLAS data is detailed in Chapter 6. The measurement of the top quark pair production cross section using the SMT tagger was performed and is detailed in Chapter 7. Chapter 8 includes a feasibility study measuring the potential performance of the SMT tagger in the search for theoretical particles that produce pairs of top quarks with very high momentum.

The calibration presented in Chapter 6 is based on a standard method for calibration widely used in the ATLAS collaboration. The object selection used are based on a previous calibration performed by a former member of the RHUL top quark group. This selection was however adapted to work with 2012 ATLAS data and completely reimplemented by me using up-to-date software tools and a different type of data-sample. All results, plots and/or diagrams

presented are my own unless otherwise noted. The cross section measurement presented in Chapter 7 is the result of the joint RHUL-QMUL work group and includes contributions from current and past members of the group. The multijet background estimation in the electron channel using data-driven techniques was contributed by me and is described in more detail in Section 7.3.1. I have contributed a chapter detailing this estimation to the published paper in:

J Blanco et al. "Measurement of the top quark pair production cross-section with ATLAS in pp collisions at $\sqrt{s} = 7$ TeV in the single-lepton channel using semileptonic b decays". In: ATLAS-COM-CONF-2012-056 (Mar. 2012)

Finally, Chapter 8 includes a comparison between the SMT tagger and a lepton identification technique known as mini-isolation. This technique was devised and developed by other members of the ATLAS collaboration, however the performance measurement presented here is my own work. Once again all results, plots or diagrams in this chapter are my own unless stated otherwise.

Contents

List of Figures

List of Tables

Chapter 1

Introduction and motivation

The Large Hadron Collider or LHC [2], is the most powerful collider in the world and gives scientists a probe to study the universe at an unprecedented energy level. The ATLAS experiment is a general-purpose detector serviced by the LHC designed to record and measure every aspect of the outgoing spray of particles resulting from the colliding LHC beams.

High energy research can be divided into several categories: testing the established theory known as the Standard Model of particle physics (SM) [3], improvement of previously measured parameters and the search for new physics. The SM has stood the test of time and rigorous experimental testing. A crucial part of the theory, the Higgs mechanism [4, 5, 6, 7, 8], was experimentally validated in 2012 when the ATLAS [9] and CMS [10] experiments independently confirmed the production of the Higgs boson in LHC collisions [11, 12].

Top quark physics concerns itself with the study of the heaviest known quark described by the SM. Due to its large mass the top quark does not bind to other quarks to form a composite particle known as a hadron. The top is the only quark that can therefore be studied directly on its own. The mass of the top quark is a parameter of the SM and many beyond the SM (BSM) theories, however it is not predicted and must be experimentally measured.

Due to the large centre of mass energy at the LHC, top quarks are produced in large quantities allowing for detailed studies of many top quark properties. Top quarks can be produced either in single-top events or, more likely at the LHC, into a pair with one top and one antitop ($t\bar{t}$ pair). The top quark decays overwhelmingly into a W boson and a b-quark. Subsequently the W can decay leptonically, into a lepton and lepton neutrino; or hadronically, into a pair

of quarks. Top quark pair events are classified into three groups depending on the manner in which the W bosons decay: "all-hadronic", where both W bosons decay hadronically; "dilepton", where both bosons decay into leptons; and finally, "lepton plus jets" where one boson decays leptonically and the other hadronically.

The b-quark binds with other quarks to form hadrons. This hadron then decays into a collimated shower of particles known as a jet. Identification of these b-jets is an important part of any top quark analysis and there are several methods of b-tagging in use. The *soft muon tagger* (SMT tagger), with which this thesis concerns itself, is one such b-tagger. B-hadrons can decay so as to produce a low momentum muon (also known as a soft muon) which then emerges buried within the subsequent jet. The SMT tagger uses the quality of the reconstruction of so-called combined muons, which rely on both inner detector and muon spectrometer information for reconstruction. The quality of the matching between the inner detector and muon spectrometer tracks is encapsulated in the χ^2 of the match. Muon reconstruction and the SMT tagger are described in more detail in Section 5.2.4.

Measurement of the top quark pair production probability, denoted by the cross section $\sigma_{t\bar{t}}$, is an important early measurement to make. In particular as the cross section depends on the centre of mass energy of the collision, such a measurement tests the predictive power of the Standard Model at an energy level never studied before. Any new physics processes which share the same signature as $t\bar{t}$ production will result in an excess in the cross section above the theoretically measured value.

An example of new physics include theories that posit the existence of a very heavy boson known as the Z' [13, 14, 15]. This boson could decay to a $t\bar{t}$ pair where each top quark has a large amount of momentum.

In this thesis the SMT tagger is calibrated and used as part of a cross section measurement and its performance is evaluated in searching for high momentum tops emerging from Z' decays. Measuring the top quark pair production cross section using the SMT tagger is of interest as it tests a different aspect of theory, namely the description of semileptonic b-decays, compared to lifetime-based taggers. Such a measurement was carried out and is detailed in Chapter 7.

Other soft muon tagging techniques exist, these however depend on the presence of a jet in the event to work. The SMT tagger, in its χ^2_{match} form, only relies on the presence of a muon

to measure its performance. The calibration of the tagger on 2012 ATLAS data is presented in Chapter 6.

In addition, this means that the tagger can be used to identify muons emerging from the W rather than from semileptonic b-decays. The performance of such a technique is studied in Chapter 8 where the tagger is tested in two ways. Firstly, the tagger is used to identify the muon emerging from the W boson decay. Its performance is compared to the nominal approach, as well as a novel method specifically designed for boosted top searches known as mini-isolation. Secondly, the tagger is used to identify the b-jets in the event and its performance in this regime is compared to the standard MV1 tagger.

Chapter 2

The Standard Model of particle physics

Particle physics is the study of the fundamental constituents of matter and their interactions. The best current description of these interactions is known as The Standard Model of Particle Physics (SM); a group of theories that cover all currently known particles and their interactions. The SM was developed throughout the latter half of the twentieth century and has stood the test of time and rigorous examination by numerous experiments. Many of its parameters have also been measured with great precision e.g. the electron magnetic moment g is known to 10^{-13} [16]. The last piece to be confirmed was the existence of the Higgs boson, which in turn points to the existence of the so-called Higgs field. Evidence of this particle was observed by the ATLAS and CMS experiments at CERN in 2013 [11, 12]. Despite its tremendous success, the SM cannot explain all observed phenomena in the universe. Firstly, the theory does not predict the value of all of its parameters and many of them, like the number of particle generations, must be measured empirically. The theory also does not describe gravity the most familiar of the fundamental forces. Furthermore, the SM does not provide a candidate for dark matter or dark energy, which according to recent measurements accounts for more than $90\,\%$ of the total energy density in the universe [17]. The clear asymmetry between matter and antimatter is also not fully explained in the realm of the SM. Because of these deficiencies there is a strong focus on developing theories which go beyond the standard model (BSM) to provide an answer to these open questions.

In this chapter an introductory overview of the Standard Model is provided. For a more detailed description of the theory see references [18, 3] on which this chapter is largely based.

The SM describes the interactions of the fundamental constituents of our universe in terms of the three different fundamental forces: the strong, weak and electromagnetic (EM), each described by a specific theory. The most familiar of the forces, gravity is not described. The SM classifies particles into several categories depending on their properties and allowed interactions. Particles which have a half-integer spins (e.g. $S = \frac{1}{2}, \frac{3}{2}, \ldots$) are known as *fermions*, these are the basic constituents of matter. Particles with integer spins (e.g. $S = 0, 1, \ldots$) are known as *bosons*, these mediate interactions between fermions and other bosons.

Fermions can be divided into two subgroups: quarks, which can interact via the strong, weak and electromagnetic forces; and leptons which can only interact via the weak and electromagnetic forces. There are six known leptons: electron e, muon μ and tau τ, which all have electric charge[1] $Q = 1$; and the corresponding electrically neutral neutrino ν_e, ν_μ and ν_τ. Analogously, six quark *flavours* are known: u, c and t, with electric charge $Q = +2/3$ and d, s and b, with electric charge $Q = -1/3$.

Quarks and leptons are divided into three generations which differ only by the mass and flavour of their constituent fermions, each generation being heavier than the previous. A summary of all elementary particles described by the SM can be found in Table 2.1.

For every matter fermion f there is an equivalent antimatter partner $\bar{f}$ which possesses the same characteristics as its matter companion but is opposite in electric charge. Thus 12 matter particles are combined with 12 antimatter partners for a total of 24 elementary particles which form all visible matter in the universe.

Interactions between fermions occur via the exchange of spin one particles known as bosons. As shown in Table 2.2, each force is mediated by one or more bosons. The strong force is mediated by a set of massless bosons known as the gluons, the weak by a neutral massive boson known as the Z boson and a pair of charged massive bosons known as the W bosons. Finally, the electromagnetic force is mediated by the massless photon. Each boson has an antimatter partner however some, like the photon, are indistinguishable from their matter version. A summary of the properties of the SM bosons is shown in Table 2.1.

Each fermion has a set of so-called quantum numbers which classify the type of interac-

[1]The electric charge is always stated in units of elementary charge e

tions that can occur. For example, each lepton has a *lepton number* associated with it, electrons have an electron lepton number $L_e = +1$, while the positron has $L_e = -1$. Muons and taus have their own respective lepton numbers, L_μ and L_τ. Each neutrino has lepton number $L_f = 1$ and their anti-matter counterpart have $L_f = -1$. Each of these lepton numbers is approximately conserved separately across interaction vertices. The conservation is only approximate due to the non-zero mass of neutrinos. Another example of a quantum number is *baryon number* B. Each quark has $B = \frac{1}{3}$ and antiquarks have $B = -\frac{1}{3}$.

2.1 Quantum electrodynamics

The interaction of particles via the electromagnetic force is described by *quantum electrodynamics* (QED). These interactions are mediated by the massless neutral boson known as the photon and the strength of the interaction is characterized by the fine-structure constant α. All electrically charged fermions are allowed to interact and since the photon itself is not charged, no self-interaction is allowed within QED. Figure 2.1 shows the single vertex described by QED where two fermions interact via a photon. Note that the electric charge is conserved across the vertex, so for example $\gamma \to e^+e^+$ is not allowed within QED.

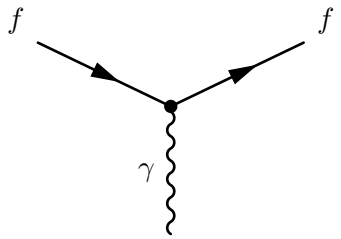

Figure 2.1: The fundamental interaction vertex described by QED. The straight-lines represent any charged fermion, while the wavy line is a photon. All possible QED vertices can be obtained by simply rotating this vertex.

By combining different forms of this vertex one can build every possible QED interaction. The interaction $e^+e^- \to e^+e^-$ is known as Bhabha scattering. Two leading order (LO) diagrams contribute to this interaction, annihilation (Figure 2.2a) and scattering (Figure 2.2b). A leading order diagram is that which has the lowest number of vertices for a given initial and final state. Adding extra vertices while retaining the initial and final state, by the addition of loops for example, produces higher-order diagrams. These are sequentially labelled as next to

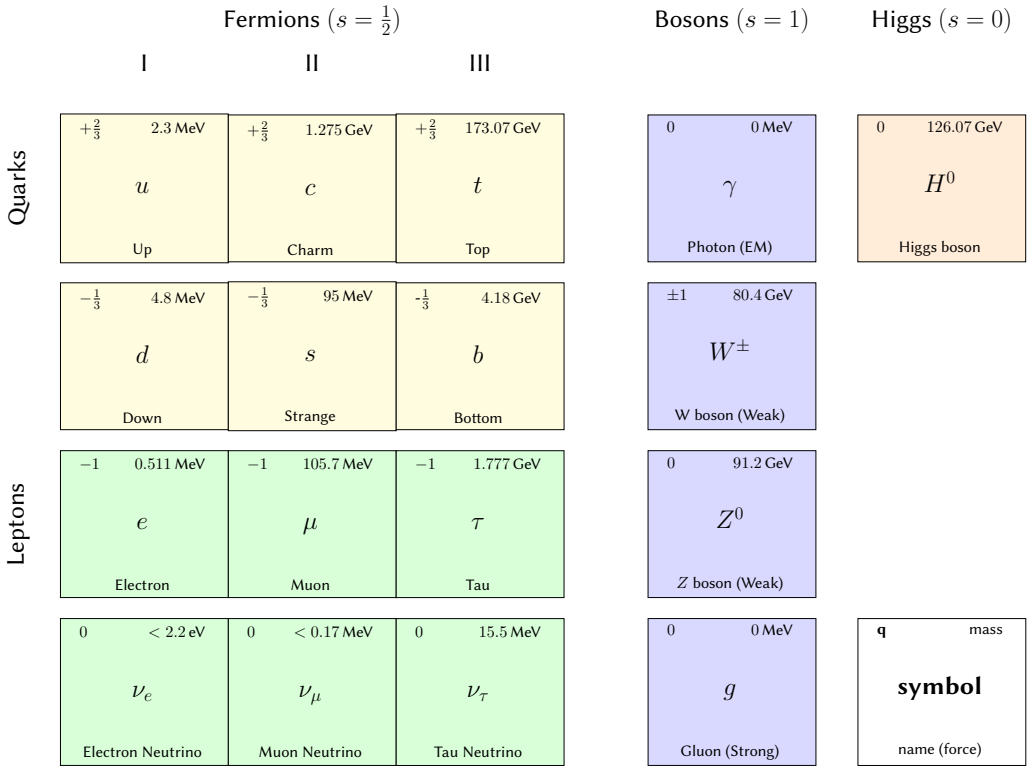

Table 2.1: A summary of all elementary particles described by the SM [19]. Note the various groupings and divisions including by spin, generation and particle type. For each particle the charge (q), mass and name are shown as per the legend on the bottom-right.

Name	Relative Strength	Boson
Strong	10^{38}	Gluons
Electromagnetic	10^{36}	Photon
Weak	10^{25}	W and Z
Gravity	1	Graviton*

Table 2.2: A summary of the four fundamental forces ordered by approximated relative strength. These are included to demonstrate the large differences in strength that span many orders of magnitude. A more accurate determination of the interaction strength depends on the details of the interaction itself. * The graviton is the theoretical boson responsible for mediating gravitational interactions and is not part of the SM.

leading order (NLO), next to next to leading order (NNLO), and so on.

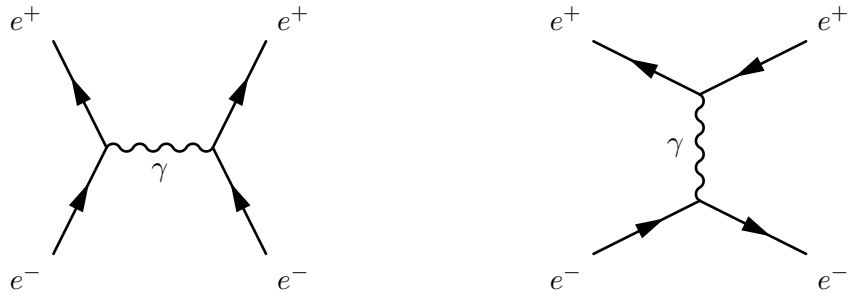

(a) Electron-positron pair annihilation. **(b)** Electron-positron pair scattering.

Figure 2.2: Feynman diagrams of the process $e^+e^- \rightarrow e^+e^-$ allowed in QED at leading order. Additional vertices can be added to produce higher-order diagrams of the same process.

2.2 Quantum chromodynamics

Interactions via the strong force are described in the theory of *quantum chromodynamics* (QCD). These interactions are mediated by a set of massless neutral bosons known as gluons. QCD introduces the concept of colour which dictates which interactions are allowed via the strong force. Colour can take three states, red (anti-red), blue (anti-blue), green (anti-green):

$$r = \begin{pmatrix} 1 \\ 0 \\ 0 \end{pmatrix}, \qquad g = \begin{pmatrix} 0 \\ 1 \\ 0 \end{pmatrix}, \qquad b = \begin{pmatrix} 0 \\ 0 \\ 1 \end{pmatrix} \tag{2.1}$$

$$\bar{r} = \begin{pmatrix} 1 & 0 & 0 \end{pmatrix}, \qquad \bar{g} = \begin{pmatrix} 0 & 1 & 0 \end{pmatrix}, \qquad \bar{b} = \begin{pmatrix} 0 & 0 & 1 \end{pmatrix} \tag{2.2}$$

Both quarks and gluons possess colour and as a result gluons can self-interact in a three gluon vertex (Figure 2.3b) or a four gluon vertex (Figure 2.3c). As with electrical charge, colour-charge must also be conserved. In the scattering process $q \rightarrow qg$, shown in Figure 2.3a, the flavour of the quark does not change but the colour-charge does. The difference in colour is carried away by the scattered gluon. Thus each gluon has two colour states associated with it, a colour state and an anti-colour state. Naively one would expect nine different types of gluons that participate in interaction, because of the nine combinations of colour and anti-colour.

However the SU(3) symmetry on which QCD is based results in a colour octet:

$$\begin{aligned} (r\bar{b} + b\bar{r})/\sqrt{2} \qquad & -i(r\bar{g} - g\bar{r})/\sqrt{2} \\ -i(r\bar{b} - b\bar{r})/\sqrt{2} \qquad & (b\bar{g} + g\bar{b})/\sqrt{2} \\ (r\bar{r} + b\bar{b})/\sqrt{2} \qquad & -i(b\bar{g} - g\bar{b})/\sqrt{2} \\ (r\bar{g} + g\bar{r})/\sqrt{2} \qquad & (r\bar{r} + b\bar{b} - 2g\bar{g})/\sqrt{6} \end{aligned} \tag{2.3}$$

and the overall colourless "colour singlet":

$$(r\bar{r} + g\bar{g} + b\bar{b})/\sqrt{3} \tag{2.4}$$

There are eight different gluons that can participate in interactions each with a different colour-charge combination, and a ninth colourless gluon that does not interact. Gluons being colour-charged has far reaching consequences for QCD.

In the realm of QED the vacuum around an electric charge becomes polarized as opposite charges get attracted and like charges are repelled. This has the effect of partially cancelling out the electric field experienced at a finite distance from the central charge. This effect is known as screening and also occurs with colour-charge. Quark-antiquark pairs screen the true colour-charge of the central real quark.

However, since gluons also carry colour they cause the opposite effect (anti-screening) to amplify and change the observed colour of the quark. Which effect, screening or anti-screening, wins out depends on the number of colours in the theory and the number of quark flavours. Currently, three colour states and six different quark flavours are known. This makes screening the overall dominant effect and as a result, the colour potential decreases with distance and quarks experience very little potential when very near to each other. This phenomenon is known as asymptotic freedom and forces quarks to form bound colourless states known as *hadrons*.

Hadrons can be divided into two categories: *mesons*, which contain a quark and an anti-quark ($q\bar{q}$); and *baryons*, which are made of three anti/quarks each with a different anti/colour-charge to result in a colourless composite particle. Common examples of baryons are protons (uud) and neutrons (udd) which are the building blocks of atomic nuclei. The pion $\pi^0 = u\bar{u}/d\bar{d}$ is a meson which is commonly produced in hadron colliders. Due to their quark configuration,

baryons have baryon number $B = +1$ while mesons have $B = 0$.

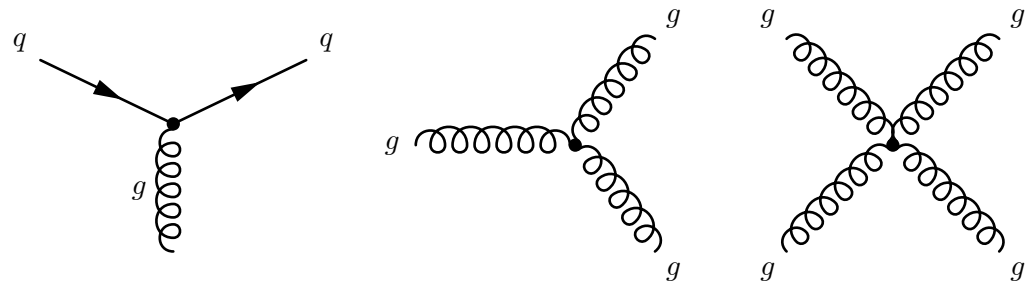

(a) Quark-gluon vertex **(b)** Three-gluon vertex **(c)** Four-gluon vertex

Figure 2.3: The fundamental interaction vertices described by quantum chromodynamics. Shown are (a) gluon emission from a quark, (b) gluon emission from a gluon, and (c) the four-gluon vertex.

2.3 Weak interactions

The final type of interaction involves the so-called weak force. The weak force is responsible for common nuclear processes such as for β^- decay ($n \rightarrow pe^-\bar{\nu}_e$). Interactions via the weak force are mediated by three massive bosons: the neutral Z^0 boson and the W^+ and W^- bosons. Since these posses mass the range of interaction is very short, unlike electromagnetic interactions via a massless photon.

All fermions can interact via the weak force, but to start let's consider weak interactions involving only leptons. A valid interaction via the weak force occurs via a combination of the fundamental vertices shown in Figure 2.4, while conserving electric charge and lepton flavour. Weak bosons also couple to each other via the vertex $Z \rightarrow W^-W^+$. As the W bosons have charge they also couple to the photon.

Weak interactions involving quarks are more complicated than those with only leptons. The neutral vertex is similar to that of the leptonic version, a quark scattering off a Z boson. However, the charged current changes the flavour of an up-type quark into a down-type quark (or vice-versa) with an associated W boson of the appropriate charge (Figure 2.4c). This change in flavour can also happen across quark generations. The semileptonic decay of b-quarks is an example of flavour changing charged weak interactions. The b-quark (in a B meson bound state) transitions into a c-quark by emitting a W boson. In order to account for such an interaction and preserve the universality of weak interactions, Nicola Cabibbo postulated [20] that

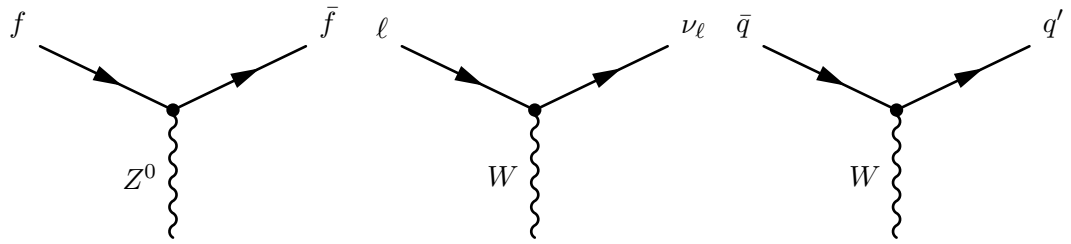

(a) Neutral vertex **(b)** Charged vertex (leptons) **(c)** Charged vertex (quarks)

Figure 2.4: The fundamental interaction vertices described the weak theory. Shown are the (a) neutral vertex, (b) charged vertex with leptons, and (c) charged vertex with quarks. Where $f = e, \mu, \tau$ and ν_ℓ is the corresponding lepton neutrino of the same flavour.

the states that couple to the charged current are really a mixture of 'rotated' quark states:

$$\begin{pmatrix} u \\ d' \end{pmatrix} \begin{pmatrix} c \\ s' \end{pmatrix} \tag{2.5}$$

where

$$d' = d\cos\theta_c + s\sin\theta_c \tag{2.6a}$$

$$s' = -d\sin\theta_c + s\cos\theta_c \tag{2.6b}$$

This introduces an arbitrary parameter into the theory known as the quark mixing angle or the Cabibbo angle θ_c. The introduction of quark mixing has the effect of attenuating the interaction strength at vertices involving multiple quark generations. Interactions which cross one generation are said to be Cabibbo Suppressed while those that cross two generations are Doubly Cabibbo suppressed.

Taking into account the three quark generations, quark mixing can be expressed in matrix notation as shown in Equation 2.7. This unitary matrix is known as the Cabibbo-Kobayashi-Maskawa matrix (CKM matrix) after Cabibbo who initially postulated quark mixing, and Makoto Kobayashi and Toshihide Maskawa who later added an additional generation, containing the top and bottom quarks, to the matrix [21]. The interaction strength at a given vertex is then proportional to $|V_{ij}|^2$.

$$\begin{pmatrix} d' \\ s' \\ b' \end{pmatrix} = V_{CKM} \begin{pmatrix} d \\ s \\ b \end{pmatrix} = \begin{pmatrix} V_{ud} & V_{us} & V_{ub} \\ V_{cd} & V_{cs} & V_{cb} \\ V_{td} & V_{ts} & V_{tb} \end{pmatrix} \begin{pmatrix} d \\ s \\ b \end{pmatrix} \tag{2.7}$$

Several parametrizations of the CKM matrix exist, the Chau-Keung parametrization [22] uses angles θ_{12}, θ_{23}, θ_{13} and a phase δ:

$$V_{CKM} = \begin{pmatrix} c_{12}c_{13} & s_{12}c_{13} & s_{13}\exp(-i\delta) \\ -s_{12}c_{23} - c_{12}s_{23}s_{13}\exp(i\delta) & c_{12}c_{23} - s_{12}s_{23}s_{13}\exp(i\delta) & s_{23}c_{13} \\ s_{12}s_{23} - c_{12}c_{23}s_{13}\exp(i\delta) & -c_{12}s_{23} - s_{12}c_{23}s_{13}\exp(i\delta) & c_{23}c_{13} \end{pmatrix} \tag{2.8}$$

where $c_{ij} = \cos\theta_{ij}$ and $s_{ij} = \sin\theta_{ij}$ for $i = 1,2,3$. This parametrization has the advantage that each angle θ_{ij} relates to a specific transition from one generation to the other. If $\theta_{13} = \theta_{23} = 0$ the third generation is not coupled to the other two and the matrix is reduced to the one postulated by Cabibbo. Note that θ_{12} is the Cabibbo angle described earlier.

Another parametrization due to Wolfenstein [23] expresses all elements in terms of the Cabibbo angle by defining $\lambda \equiv s_{12} = \sin\theta_{12}$ and then expressing the other elements in powers of λ

$$V_{CKM} \approx \begin{pmatrix} 1 - \lambda^2/2 & \lambda & A\lambda^3(\rho - i\eta) \\ -\lambda & 1 - \lambda^2/2 & A\lambda^2 \\ A\lambda^3(1 - \rho - i\eta) & -A\lambda^2 & 1 \end{pmatrix} \tag{2.9}$$

where A, ρ and η are all real numbers that express the order of magnitude differences between s_{12} and the other elements in the matrix.

All the elements should be the same irrespective of which parametrization is used. The elements of the CKM matrix have been measured and the latest accepted results [19] are summarized in Equation 2.11.

The unitarity of the CKM matrix implies that the probability of transition from any up-type

quark to any down-type is the same,

$$\sum_k |V_{ik}|^2 = \sum_i |V_{ik}|^2 = 1 \tag{2.10}$$

for all i quark generations [24]. The term V_{tb} is approximately unity and by far dominates over the other V_{tj} terms. This means that the top quark transitions almost exclusively into a b-quark ($t \to Wb$) with transitions $t \to Ws$ and $t \to Wd$ having a probability of less than 1%. The soft muon tagger which is the focus of this thesis relies on weak semileptonic decays of b-quarks. From 2.11 [19] one can see that the transition $b \to c$ dominates over $b \to u$. This thesis concerns itself with $t\bar{t}$ events in the lepton plus jets channel where one W boson decays hadronically with a rate governed by the elements of the matrix.

$$V_{CKM} = \begin{pmatrix} 0.97427 \pm 0.00015 & 0.22534 \pm 00065 & 0.00351 \,^{+\,0.00015}_{-\,0.00014} \\ 0.22520 \pm 0.00065 & 0.97344 \pm 0.00016 & 0.0412 \,^{+\,0.0011}_{-\,0.0005} \\ 0.00867 \,^{+\,0.00029}_{-\,0.00031} & 0.0404 \,^{+\,0.0011}_{-\,0.0005} & 0.999146 \,^{+\,0.000021}_{-\,0.000046} \end{pmatrix} \tag{2.11}$$

An additional unique feature of weak interactions is that the charge conjugation-parity (CP) symmetry is violated. The operator C denotes the change of a particle by its antiparticle partner and P denotes a spatial inversion. A clear violation of C and P was observed in the radioactive decay of Cobalt-60, where the resulting electrons were preferentially emitted in the opposite direction of the nuclear spin of the Cobalt [25]. Thus weak currents only couple to left-handed neutrinos (or right-handed anti-neutrinos) which is a violation of parity. Additionally charge symmetry is also violated since a left-handed neutrino is preferentially picked over a left-handed anti-neutrino. Finally in 1964 CP violation was observed in the decay of neutral kaon [26].

Thus the probability of $\bar{a} \to \bar{b}$ is not equal to that of $a \to b$. The existence of CP violation has interesting consequences for the formation of the early universe. The preferential production of matter over antimatter in CP violating interactions would shift the balance in favour of matter resulting in a universe similar to our own. In terms of the Wolfenstein parametrization of the CKM matrix, if $\eta = 0$ there is no CP violation. This parameter has been measured to

be non-zero pointing to CP violation [19].

2.3.1 Electroweak unification and the Englert-Brout-Higgs mechanism

The unification of the electromagnetic and weak theories was first proposed by Glashow and later developed by Weinberg and Salam into the electroweak theory [27, 28, 29]. The theory postulates that while at low energies the two forces are to be treated separately, at higher the two can be seen as a single force. Thus the two forces are different manifestation of the same "electroweak" interaction. There were several stumbling blocks to the unification of the forces. Firstly, the boson which drives the electromagnetic interaction, the photon, is massless while the weak bosons are both massive. Evidence for the massive nature of these bosons has been established by experimental results from the UA1 experiment at CERN [30].

Thus the symmetry of the theory must be spontaneously broken in some way. A mechanism for electroweak symmetry breaking (EWSB) was proposed and developed by Anderson, Brout, Englert, Higgs, Guralnik, Hagen, Kibble, and t' Hooft which introduces masses to the weak bosons and posits the existence of an additional scalar (spin $S = 0$) boson known as the Higgs boson.

Gauge theories

Gauge invariance is one of the underlying invariances which underpins the Standard Model. Given the so-called Dirac Lagrangian[2]

$$\mathcal{L} = i\hbar\bar{\psi}\gamma^{\mu}\partial_{\mu}\psi - m^{2}\bar{\psi}\psi \tag{2.12}$$

which describes a free particle of spin-$\frac{1}{2}$ with mass m [3]. Note that it is invariant under the transformation

$$\psi \rightarrow e^{i\theta}\psi \tag{2.13}$$

where θ is a real number, since the adjoint $\bar{\psi} \rightarrow e^{-i\theta}\bar{\psi}$ and the two terms cancel out. This is known as a *(global) gauge transformation* since θ is the same at all points of space-time. A *(local)*

[2] A Lagrangian is a mathematical function that describes the underlying dynamics of a system as a function of time and space coordinates (x^{μ}) and their time derivatives.

gauge transformation occurs when the phase is different for different points in space-time

$$\psi \rightarrow e^{i\theta(x)}\psi \tag{2.14}$$

The Dirac Lagrangian in Eq. 2.12 is not invariant under a local gauge transformation since extra terms are created by the derivative. Local gauge variance results in divergences in the theory when trying to calculated the cross-section. Thus to preserve the good behaviour of the theory local gauge invariance must be imposed. In the case of the Dirac Lagrangian, this is done by modifying the derivative to a gauge covariant derivative. This generates terms that cancel the extra terms introduced by the local gauge transformation, thereby restoring the invariance. As it turns out this results in the introduction of a new massless vector field that couples to ψ.

The new Lagrangian then describes a spin-$\frac{1}{2}$ particle with mass m that interacts with a free massless field. This new field can be identified as the electromagnetic field and the spin-$\frac{1}{2}$ particles are electrons and positrons. Thus the resulting Lagrangian describes all interactions that form part of quantum electrodynamics.

A similar procedure can be applied to the colour quark model and obtain a description of all QCD interactions. However requiring that the weak theory be a gauge theory (invariant under local gauge transformation) encounters a problem since the weak bosons are known to be massive. There must be some mechanism via which the $W^{\pm}$ and Z^0 obtain mass.

The Englert-Brout-Higgs mechanism

The Englert-Brout-Higgs mechanism[3] posits the existence of a complex scalar field doublet that when introduced into the electroweak Lagrangian results in the weak fields acquiring a mass term. In other words the $W^{\pm}$ and Z^0 interact with the Higgs field and obtain a mass. An additional consequence of introducing the Higgs field is the inclusion of a scalar boson particle, the so-called "Higgs boson". Finally, the Higgs field also couples to fermions via the Yukawa coupling generating gauge invariant mass terms for the fermions as well[4]. This coupling is dependent on the mass of the fermion involved, for a more massive particle the coupling is stronger. This is another reason for the top quark being an object of much study.

[3]Here the ATLAS naming convention is used.

[4]For a more complete description of the mathematical procedure see [3].

The SM Lagrangian in its current form including the Higgs potential is shown in Equation 2.15. This expression describes all possible particle interactions that form part of the SM, of particular interest are the fermion mass term which couples the fermion field ψ to the scalar Higgs field ϕ and the Higgs kinetic and potential terms.

$$\begin{aligned}\mathcal{L} = &- \underbrace{\frac{1}{4} W^a_{\mu\nu} W^{\mu\nu a}}_{\text{Weak Field}} - \underbrace{\frac{1}{4} B_{\mu\nu} B^{\mu\nu}}_{\text{EM Field}} - \underbrace{\frac{1}{4} G^a_{\mu\nu} G^{\mu\nu a}}_{\text{Strong Field}} \\ &+ \underbrace{\bar{\psi} i \not{D}_\mu \psi}_{\text{Fermion Kinetic}} + \underbrace{\lambda \bar{\psi} \psi \phi}_{\text{Fermion Mass}} \\ &+ \underbrace{|D_\mu \phi^2|}_{\text{Higgs Kinetic}} - \underbrace{V(\phi)}_{\text{Higgs Potential}}\end{aligned} \tag{2.15}$$

The Higgs boson, and consequently the EBH mechanism, was the last remaining piece of the SM that resisted experimental confirmation. In late 2012, the ATLAS and CMS collaborations announced [12, 11] the discovery of a Higgs-like particle with a mass around 125 GeV [31], confirming the last missing component of the SM. However, the remaining unexplained phenomenon have yet to be theoretically described and experimentally confirmed. Due to its large mass, the top quark is of much interest to BSM searches.

Chapter 3

Top quark physics

The third generation of quarks was first proposed by Kobayashi and Maskawa in a paper published in 1973 [21] as a way to explain the CP violation observed in kaon decays [26]. The existence of the third generation in the quark sector was confirmed when the lighter of the two constituents, the b-quark, was discovered in 1977 [32].

Due to its large mass, direct production of the top quark required the construction of very powerful accelerators. However, its mass was constrained in precision electroweak measurements at LEP in 1995 to be [33]:

$$m_{\text{top}} = 174 \, ^{+\,21.5}_{-\,25.5} \text{ GeV} \tag{3.1}$$

The top quark was then discovered by the CDF and D0 experiments at Fermilab in 1995 [34, 35] and then observed at CERN again in 2010 [36, 37].

The large mass of the top quark makes it a very interesting object of study. The current world average for the mass of the top quark, based on results from Tevatron and the LHC [19], is

$$m_t = 173.07 \pm 0.52\,(\text{stat.}) \pm 0.72\,(\text{syst.})\,\text{GeV}$$

Due to its mass the top quark has an extremely short lifetime $\tau \approx 0.5 \times 10^{-24}$ s, too short to interact via the strong force and hadronize into a bound state [38]. Instead the top quark decays weakly producing a W boson and a b-quark almost exclusively. This allows experimentalists to directly study the properties of a bare quark. An impossibility with the other quarks

which bind with other quarks to form hadrons. Measurement of top quark properties (mass, charge, forward-backward asymmetry, couplings, etc...) forms a large part of high energy physics research. Measurement of these properties provide rigorous tests of the SM, and could point towards the existence of new physics or exclude some BSM theories.

From an experimental perspective, top quark decays produce a very interesting signature with leptons, jets and missing energy due to the escaping neutrino[1]. Therefore, the study of top quark decays relies on all parts of a general purpose detector such as ATLAS or CMS. Finally, $t\bar{t}$ pair production also is a major background for many other SM and BSM searches, so understanding this process well is fundamental to almost all areas of HEP research.

3.1 Top quark production

Top quarks can be produced in two ways: single top production and $t\bar{t}$ pair production. In the SM the dominant top quark pair production mechanism proceeds via the strong force. The production cross section of $pp \to t\bar{t}$ depends on the mass of the top m_t, the centre of mass energy $\sqrt{s} = 2E_{\text{beam}}$ and the fraction of the momentum taken by the partons[2] of the colliding protons.

In order to produce a $t\bar{t}$ pair the total energy carried by the interacting partons must be larger than twice the mass of the top. Let us define the effective centre of mass energy $\hat{s}$ which reflects the true amount of energy available for interaction. Given two colliding partons, denoted i and j carrying x_i and x_j fractions of the centre of mass energy $\sqrt{s}$, then

$$\hat{s} = x_i\sqrt{s}x_j\sqrt{s} = x_i x_j s \tag{3.2}$$

assuming that both partons carry the same fraction of the total energy, i.e. $x_i \approx x_j$ then the minimum value of x required for $t\bar{t}$ production is

$$x \approx \frac{2m_t}{\sqrt{s}} \tag{3.3}$$

At the LHC the minimum threshold at $\sqrt{s} = 7\,\text{TeV}(14\,\text{TeV})$ is approximately 0.05(0.025).

[1] Neutrinos do not interact with the detector material and thus escape without being detected, missing energy is described in more detail in Chapter 4

[2] The constituents of hadrons: quarks and gluons

At such low values of x the fraction of proton momentum carried by the gluons is large [39] and thus gluon fusion interactions dominate as can be seen in Figure 3.1.

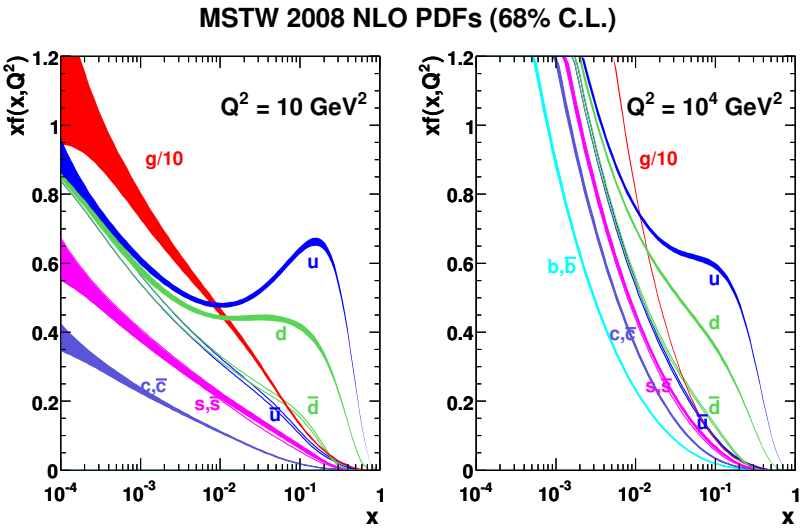

Figure 3.1: MSTW 2008 NLO parton distribution functions.

Gluon fusion processes represent $80(90)\%$ of the total cross section, with the remainder contribution coming from quark pair annihilation. The Feynman diagrams for these interactions are shown in Figure 3.2. The theoretical inclusive $t\bar{t}$ production cross sections at the LHC has been calculated to NNLO [40, 41]:

$$\sqrt{s} = 7\,\text{TeV}: \sigma_{t\bar{t}} = 158\,^{+\,13.5}_{-\,12.2}\,\text{pb}$$
$$\sqrt{s} = 8\,\text{TeV}: \sigma_{t\bar{t}} = 252.9\,^{+\,6.4}_{-\,8.6} \pm 11.7\,\text{pb}$$

Single top production occurs via the weak force almost exclusively through the Wtb vertex since $|V_{tb}| \gg |V_{ts}|, |V_{td}|$. At LO there are several production mechanisms for single-top events:

- Weak quark-antiquark annihilation forming a W which subsequently decays into a $t\bar{b}$ (Figure 3.3a).
- The so-called tW production, where a b-quark absorbs a gluon and decays to a top quark and W boson (Figure 3.3b).
- b-quark scattering off a W boson, where the b comes from gluon splitting (Figure 3.3c) or from the proton (Figure 3.3d).

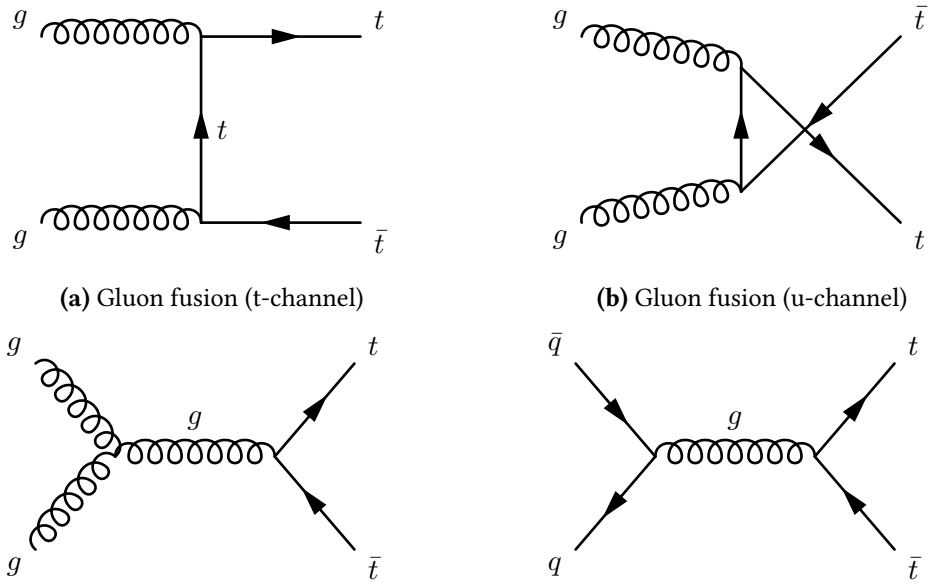

(a) Gluon fusion (t-channel)

(b) Gluon fusion (u-channel)

(c) Gluon fusion (s-channel)

(d) Quark pair annihilation

Figure 3.2: The leading order Feynman diagrams for $t\bar{t}$ production.

The cross sections for $pp \rightarrow t + X$ at the LHC have been estimated at NLO, for the t-channel [42]:

$$\sqrt{s} = 7\,\text{TeV}\text{: } \sigma_t^{\text{t-chan}} = 66 \pm 2\,\text{pb}$$
$$\sqrt{s} = 8\,\text{TeV}\text{: } \sigma_t^{\text{t-chan}} = 87 \pm 3\,\text{pb}$$

, and for tW production [43, 44, 45, 46]:

$$\sqrt{s} = 7\,\text{TeV}\text{: } \sigma_{tW} = 15.6 \pm 1.2\,\text{pb}$$
$$\sqrt{s} = 8\,\text{TeV}\text{: } \sigma_{tW} = 22.2 \pm 1.5\,\text{pb}$$

As top quark pair production can proceed via the strong force it occurs overwhelmingly more often than single top production. The production cross section of $t\bar{t}$ is approximately two times larger than the single-top cross section.

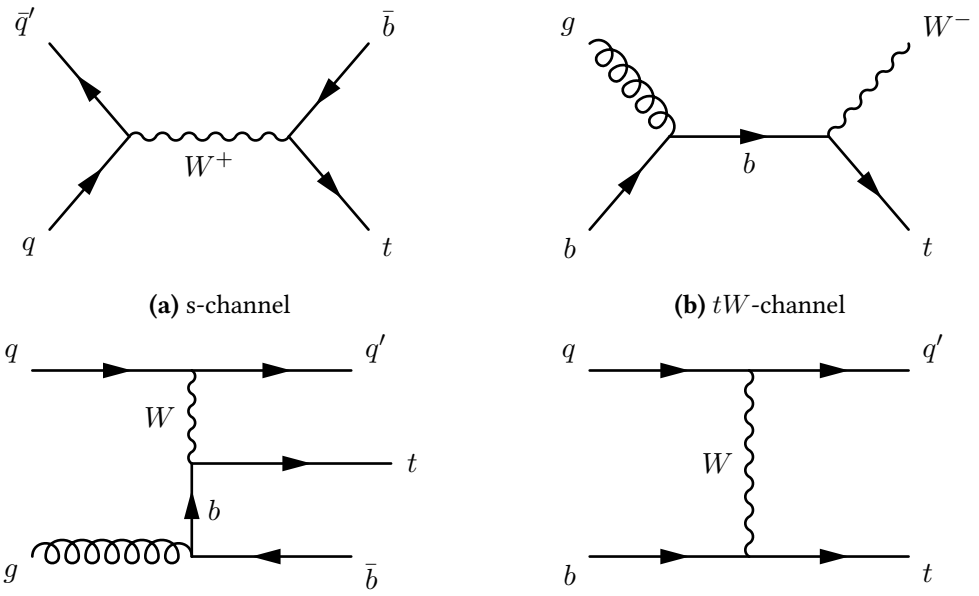

(a) s-channel

(b) tW-channel

(c) Associated with a q and $\bar{b}$

(d) Associated with a q

Figure 3.3: Example Feynman diagrams for single top quark at leading order.

3.2 Top quark decay modes

The top quark decays almost exclusively into a W boson and a b-quark. The world average measured ratio of branching ratios $\Gamma(t \to Wb)/\Gamma(t \to Wq(q = b, s, d))$ is 0.91 ± 0.04 [19]. Note that there is some tension between this measured result and the naive expectation from the CKM matrix. The measured value is 2σ away from the expected CKM result, meaning there is perhaps some room for additional quark generations not accounted for by the CKM matrix.

As the LHC collides proton-proton beams, the overwhelming majority of events produced will feature multiple hadronic *jets*, a stream of particles resulting from the hadronization of quarks in the detector, most of which will originate from "light" quarks[3]. Unlike light hadrons, B-hadrons have a sufficiently large lifetime that they travel a certain distance before decaying. Additional features such as the semileptonic decay of b-quarks can be exploited to determine the presence of such a quark in the detector. Collectively analysis techniques that permit the detection of b-jets are known as *b-tagging*. Top quark pairs will produce two b-quarks, making b-tagging techniques a central part of any $t\bar{t}$ analysis. More information on b-tagging

[3]The term light quarks usually refers to quarks in the first two generations. Light jets are those originating from those quarks

techniques, including the Soft Muon Tagger, is provided in Chapter 4.

The other part of the top decay, the W boson, is used to classify $t\bar{t}$ events. The W boson can decay leptonically ($W \to \ell\nu_\ell$) or hadronically ($W \to q\bar{q}'$) driven by the CKM vertex element. The branching ratios of W boson decays are presented in Table 3.1.

W decay to	Branching ratio [%]
$e + \nu$	10.75 ± 0.13
$\mu + \nu$	10.57 ± 0.15
$\tau + \nu$	11.25 ± 0.20
Hadrons	67.60 ± 0.27

Table 3.1: Branching ratios of W boson decay. **Hadrons** refers to all possible combinations of $q\bar{q}'$ where $\bar{q}'$ denotes the antiquark of a flavour different to that of the first quark [19].

Top quark pair events are labelled as "dilepton", "all-hadronic" or "lepton plus jets" depending on the combination of W boson decays present. The probability for a $t\bar{t}$ event to be of a given type is dependent on the branching ratios of W boson decays shown previously. As can be seen from Figure 3.4 the all-hadronic events dominate, followed by the lepton plus jets and dilepton. Each event type requires a different analysis approach due to their distinct backgrounds, branching ratio, detector signature and reconstruction requirements. Note that some lepton plus jets analyses do not explicitly treat taus directly. Nevertheless tau decays enter into these analysis via its decay to an electron or muon. Thus the true branching ratio is marginally smaller than that shown in the Figure 3.4.

The all-hadronic final state includes four light quarks which will hadronize to form four light flavour (LF) jets and two b-quarks leading to two b-jets. Due to the large hadronic activity the all-hadronic channel is very challenging. As mentioned before, hadronic collisions produce events with a large number of jets in the final state. The background to the all-hadronic channel are therefore very high. As shown in Figure 3.4 the all-hadronic channel has the largest branching ratio of the three.

The dilepton final state includes two leptons, large missing energy from two neutrinos which escape the detector and two b-jets. In contrast to the all-hadronic channel, dilepton events are very clean due to the presence of leptons and missing energy, however the branching ratio is very small and reconstruction of the top quarks is challenging due to the presence of

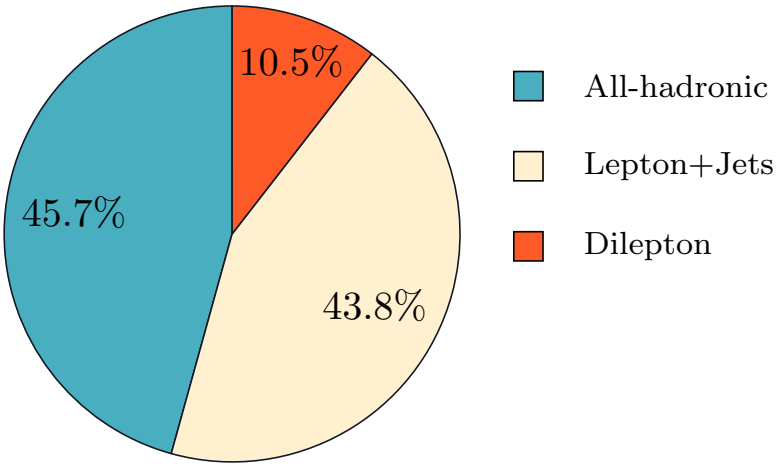

Figure 3.4: Branching ratios of all possible $t\bar{t}$ decays. These probabilities are based on the branching ratios of W boson decay shown in Table 3.1. Note that the lepton plus jets branching ratio here includes all three leptons.

the two neutrinos. Finally, the lepton plus jets channel has a larger branching ratio than the dilepton while having a distinct signature with a lepton and missing energy as well as LF jets and b-jets.

Lepton plus jets analyses do have some acceptance to τ events, but they are not usually treated as the signal lepton. The τ lepton is unstable and decays primarily via the weak force producing hadrons in the final state. Events with τ leptons enter lepton plus jets analyses when the τ decays leptonically into a muon or electron. The reconstruction of τ leptons is a complex task and τ plus jet events are treated separately with dedicated analyses. An example of the full lepton plus jets chain is shown in Figure 3.6.

The lepton plus jets channel has the advantage of a more distinct signature than the all-hadronic event as well as a suffering from less background. The branching ratio of lepton plus jets event is also approximately twice that of the dilepton channel. As a result the lepton plus jets channel has been chosen as the focus of this thesis.

3.3 Latest developments in top physics

This section discusses a few of the latest measurements in the area of top quark pair production with a focus on LHC results. Top quark decays provide the only probe to study the properties of

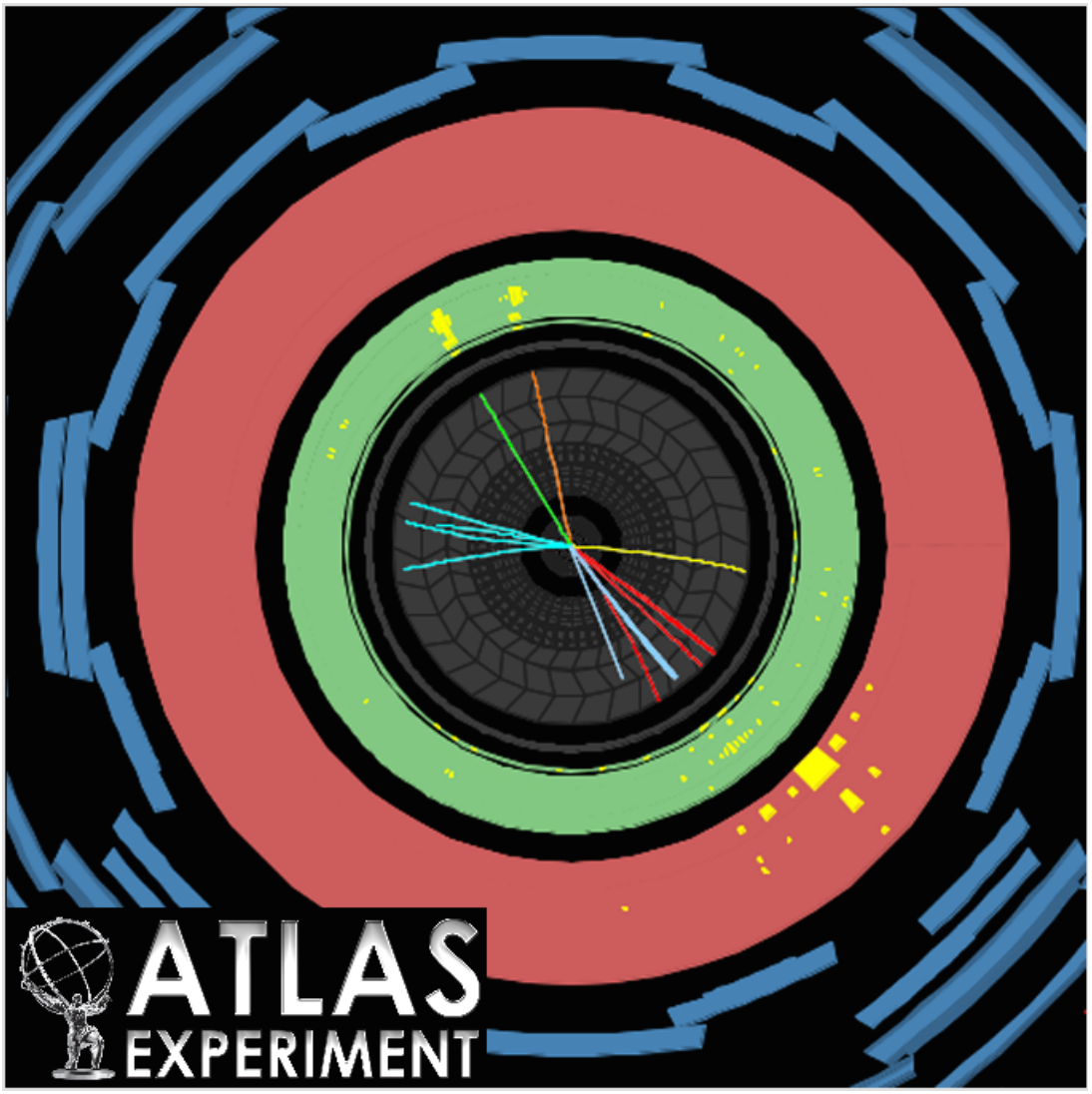

Figure 3.5: Example event display of a dilepton $t\bar{t}$ event recorded by ATLAS. The electrons are shown as yellow energy depositions in the green EM calorimeter. These are associated with a green and orange upward-pointing tracks in the ID. Some hadronic activity is noted in the red hadronic calorimeter on the opposite side.

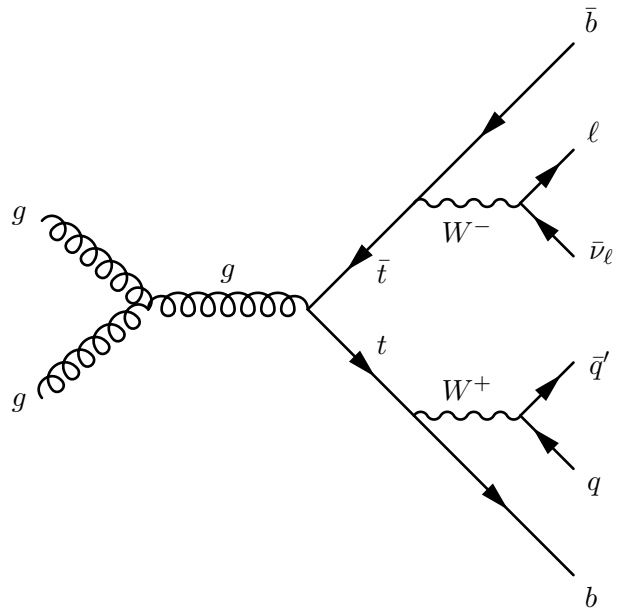

Figure 3.6: Feynman diagram of lepton plus jets channel including $t\bar{t}$ production via gluon fusion and decay with a leptonically decaying W^+. All other production mechanisms are also considered and the final state where the W^- decays leptonically is also taken into account.

a bare quark. Measurements of its properties provide a stringent test of the SM and could show hints of new physics from BSM theories. Moreover, due to its final state signature top quark pair production, particularly in the lepton plus jets channel, form the background to many searches for new physics. All parts of the detector are utilized in the reconstruction of ℓ+jets events and so it is possible to use these events to tune or *calibrate* analysis and reconstruction techniques.

Cross section measurement

Measurement of the production cross section of the top quark at different centre of mass energies[4] is a benchmark test of the SM. Any statistically significant deviation from the predicted value could point to the presence of new physics. Some BSM theories posit the existence of particles which could decay to produce a $t\bar{t}$ pair. If such theory is correct this would be observed in an increase in the cross section measured away from the predicted SM value. Precise knowledge of the cross section is also vital from an experimental perspective, for example when attempting to reduce and estimate the amount of top quark background present in other

[4]The production cross section is dependent on the centre of mass energy of the collision.

analyses. Searches for the Higgs boson exploit many different channels such as $t\bar{t}H \rightarrow t\bar{t}b\bar{b}$ which have $t\bar{t}$ events as a background. The type of events predicted by the BSM theory, supersymmetry (SUSY) include a large amount of missing energy, leptons and jets in the final state. Top quark pair events mimic these processes and constitute a large background.

A summary of all $t\bar{t}$ cross section measurements from the LHC at $\sqrt{s} = 7\,\text{TeV}$ is shown in Figure 3.7 and a comparison against the Tevatron measurement at $\sqrt{s} = 1.96\,\text{TeV}$ is shown in Figure 3.9. Early results at $\sqrt{s} = 8\,\text{TeV}$ are shown in Figure 3.8.

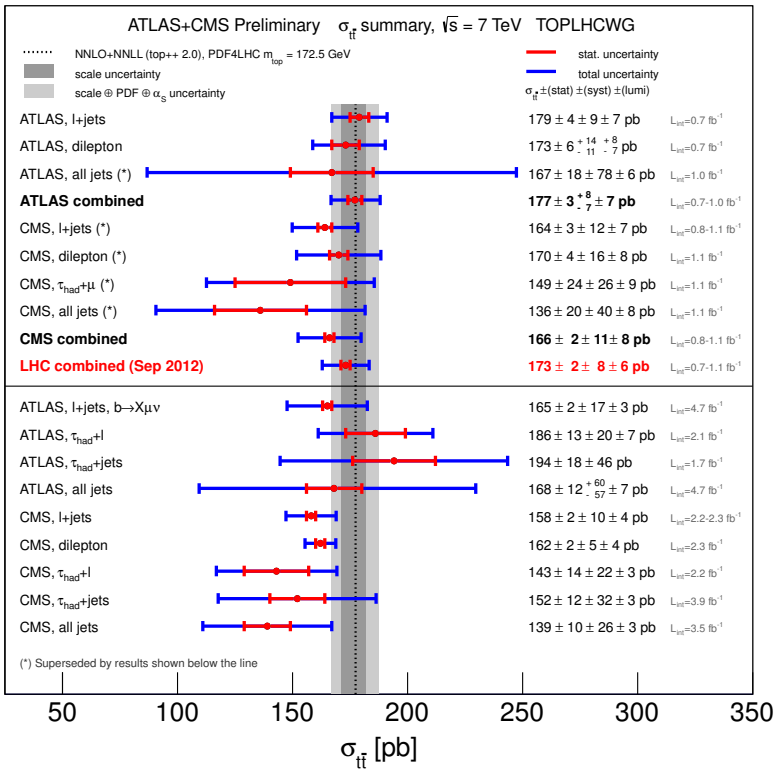

Figure 3.7: A summary of all $t\bar{t}$ production cross section measurements performed at the LHC at $\sqrt{s} = 7\,\text{TeV}$ [47]. The theory prediction shown as a dotted black line associated uncertainties as grey bands. The results shown above the black line have been statistically combined, producing the results labelled as **combined**. Many of these analyses have been superseded and the results are shown below the line. Other analyses performed but not included in the combination are also shown below the line, such as the analysis described in Chapter 7.

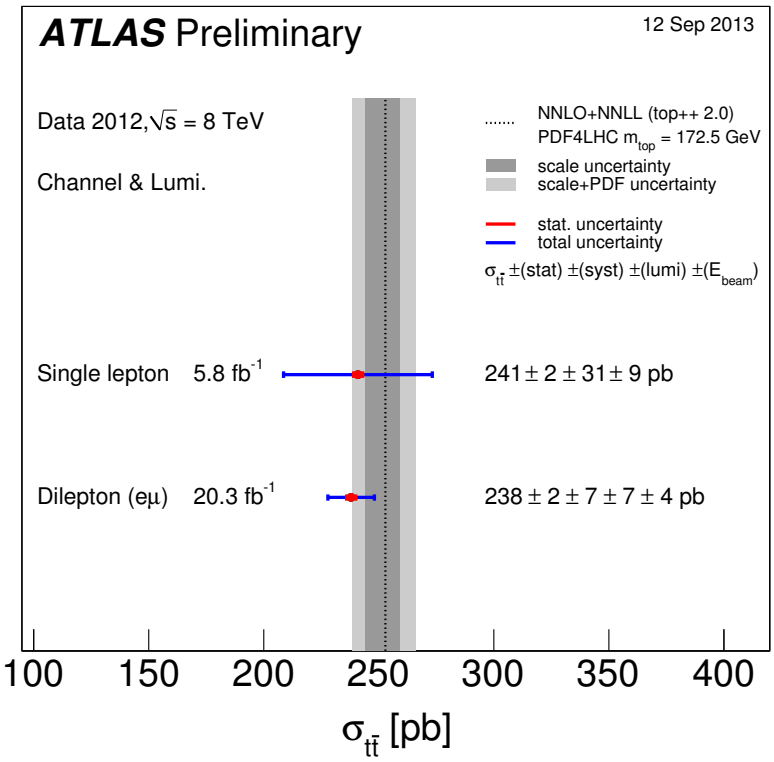

Figure 3.8: A summary of all $t\bar{t}$ production cross section measurements performed at the LHC at $\sqrt{s} = 8\,\text{TeV}$ [47]. The theory prediction is shown as a dotted line with associated uncertainties as grey bands.

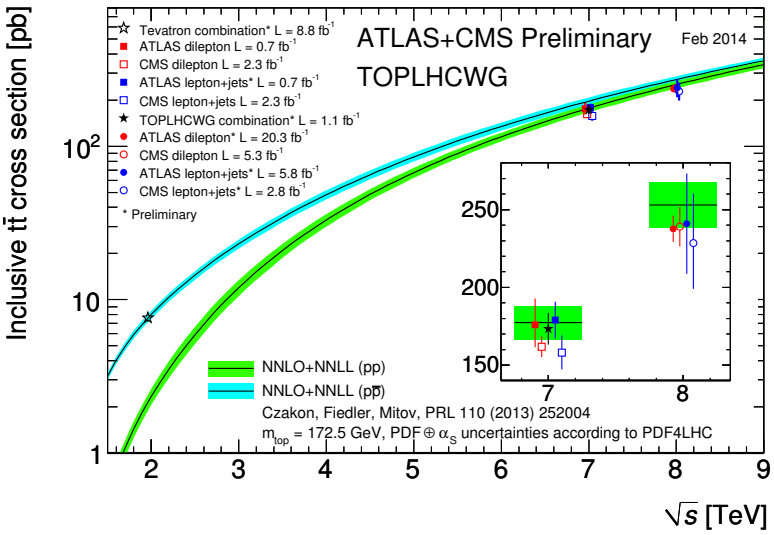

Figure 3.9: A summary of the most precise $t\bar{t}$ production cross section measurements performed at the LHC at $\sqrt{s} = 7$ and 8 TeV and the Tevatron at $\sqrt{s} = 1.96\,\text{TeV}$ compared to the theoretical prediction [47]. The Tevatron results should be compared against the prediction for $p\bar{p}$ collisions while the LHC against the pp collision predictions.

Top mass measurement

The mass of the top m_t is a fundamental parameter of the SM. Measurements of the top mass have been carried out in all $t\bar{t}$ channels at both ATLAS and CMS [48]. These results are summarized in Figure 3.10, which includes the combined LHC measurement:

$$m_t = 173.29 \pm 0.23\,(\text{stat.}) \pm 0.92\,(\text{syst.})\,\text{GeV}$$

Boosted top resonance searches

Some BSM theories predict the existence of additional particles with large masses that can decay into a pair of top quarks with very large transverse momenta. The decay products of these highly boosted tops emerge in a collimated cone. Boosted top searches have been carried out at ATLAS [49], looking for the decay products of a heavy boson known as the Z' [13, 14, 15] and Kaluza-Klein gluons [50, 51, 52, 53, 54]. A narrow leptophobic Z' with a mass of less than $1.74\,\text{TeV}$ is excluded and a Kaluza-Klein gluon is excluded for masses below $2.07\,\text{TeV}$ as shown in Figure 3.11.

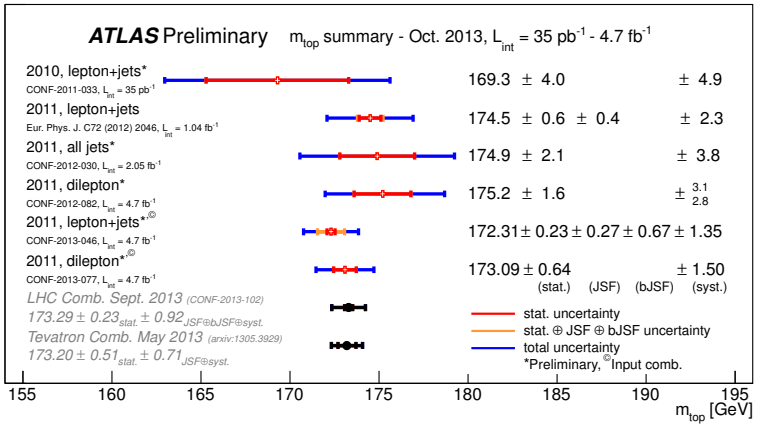

Figure 3.10: Summary of all m_t measurement results per analysis at ATLAS [47]. The statistical combination of these results are compared to the combination from Tevatron.

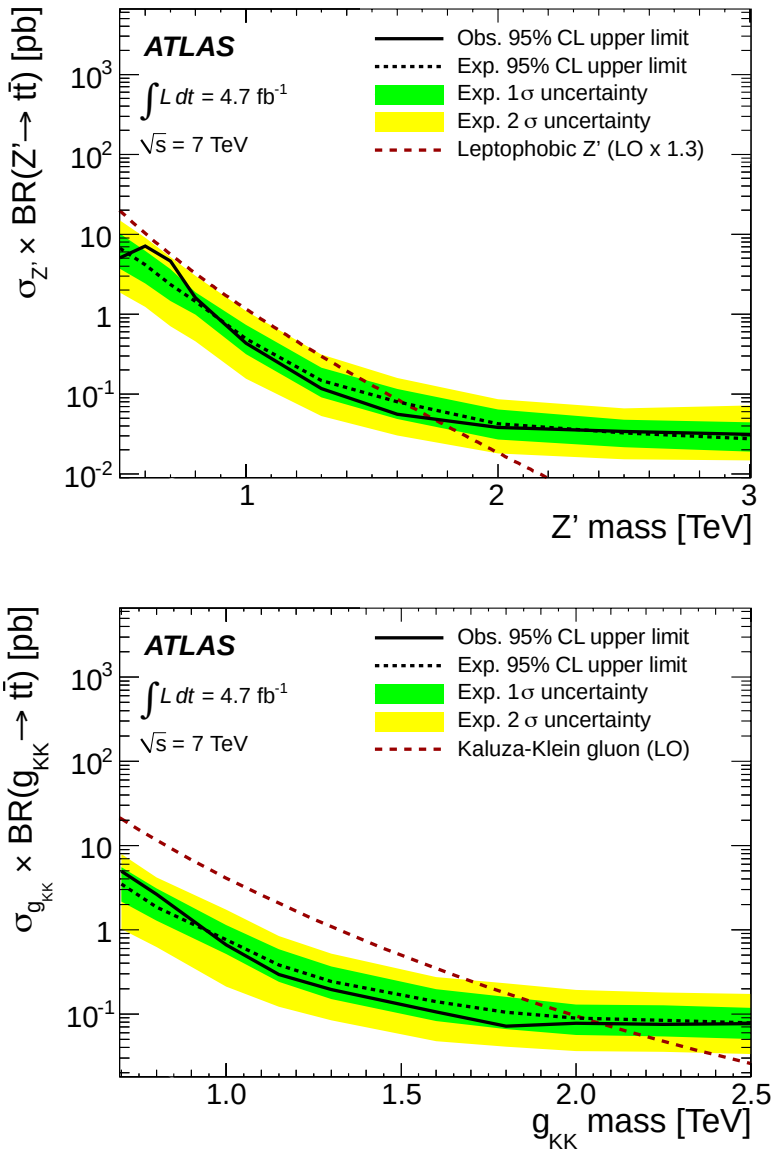

Figure 3.11: Expected (dashed line) and observed (solid line) upper limits on the cross section times the $t\bar{t}$ branching ratio of Z' (left) and Kaluza-Klein gluons (right) using the combined resolved and boosted selections. The dark (green) and light (yellow) bands show the range in which the limit is expected to lie in 68 % and 95 % of pseudo-experiments, respectively, and the smooth solid (red) lines correspond to the predicted cross section times branching fraction. Both statistic and systematic uncertainties have been included [49].

Chapter 4

The LHC and the ATLAS Detector

The Large Hadron Collider (LHC) [2] is a proton-proton ring collider located at the European Centre for Nuclear Research (CERN). The main LHC ring is housed in the tunnel which previously contained the Large Electron-Positron (LEP) collider. The LHC ring is 27 km in circumference and located as deep as 175 m underground. The LHC services seven different experiments located around the beam-pipe as shown in Figure 4.1. There are four main experiments: A toroidal LHC apparatus (ATLAS, the experiment used for this thesis), the compact muon solenoid (CMS), a large ion collider (ALICE) experiment [55], and the LHC beauty (LHCb) experiment [56].

ATLAS and CMS are general purpose detectors designed to support a varied physics programme, from SM physics like top quark measurements to BSM searches such as supersymmetry. ALICE and LHCb are more specialized experiments which focus on heavy ions and B-physics, respectively.

4.1 The large hadron collider

The LHC accelerates two beams of protons in opposite directions and then collides them at the four interaction points (IPs) where the experiments are located. The protons come from hydrogen gas where the orbiting electron is removed by an electric field, leaving behind a bare proton. The beam acceleration occurs in several stages exploiting smaller experiments present at CERN. During 2010 and 2011 protons were accelerated to a beam energy of 3.5 TeV, creating a centre of mass energy of 7 TeV and then 4 TeV per beam in 2012 for a centre of mass energy of

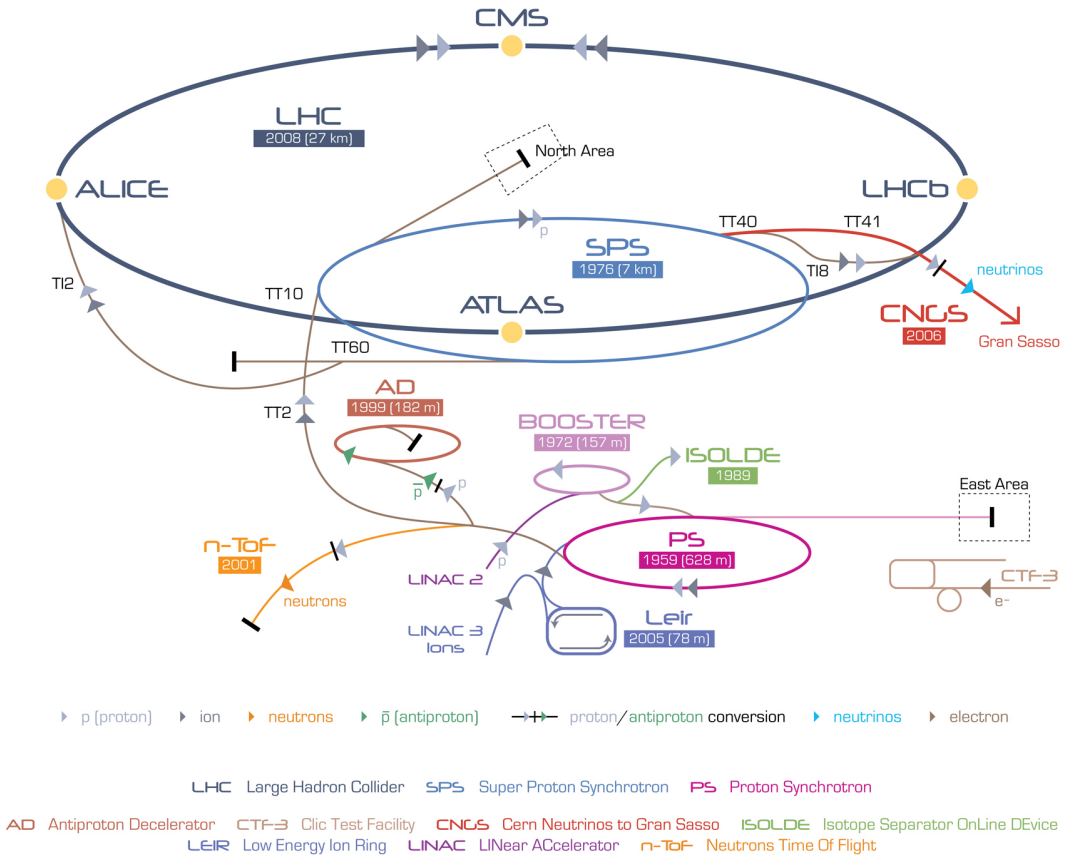

Figure 4.1: The layout of the CERN complex of experiments including the main four LHC experiments located at different points around the ring [57].

8 TeV. Each beam is made of multiple bunches of protons, with as many as hundreds of billions of protons in each bunch. Bunches are grouped into *bunch trains* with a designed *bunch spacing* of 25 ns between each of the bunches that compose a single train. The bunch spacing and size of the bunch can be altered to adjust the amount of collisions and time between collisions. During 2011 a 50 ns bunch spacing was used to allow for early low luminosity analyses to be performed. The variation in the number of colliding bunches is shown in Figure 4.2a.

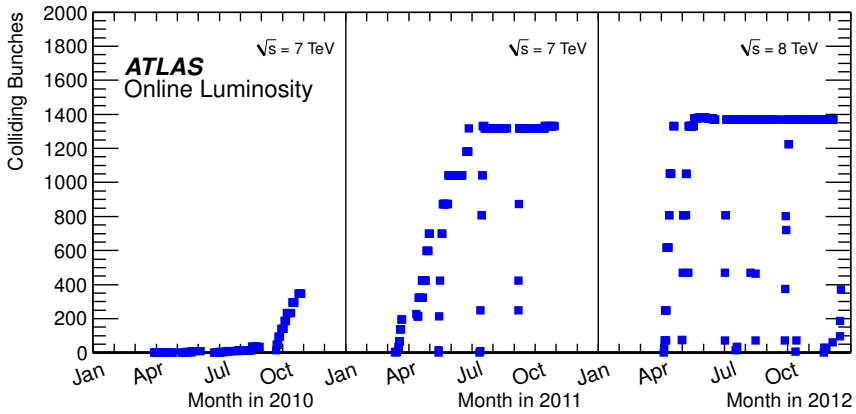

(a) The number of bunches colliding per unit time at the LHC for the 2010, 2011 and 2012 pp collision periods.

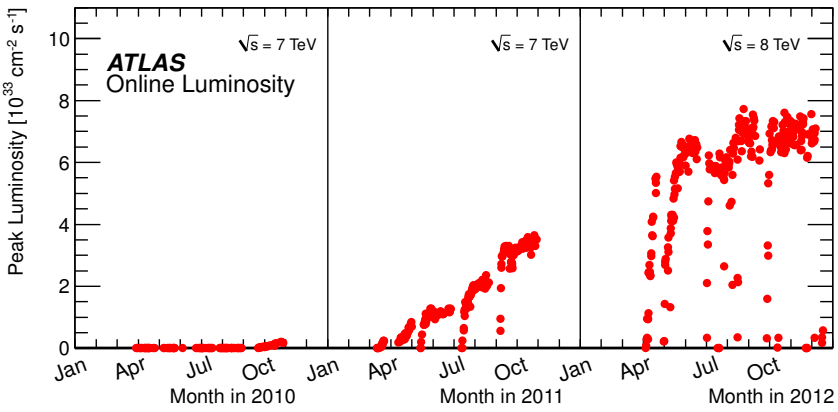

(b) The peak luminosity per unit time at the LHC for the 2010, 2011 and 2012 pp collision periods.

Figure 4.2: Shown are (a) the number of bunches colliding at the LHC and (b) the peak luminosity per unit time [58].

The acceleration of the proton beams occurs in several stages in different accelerators. The beams are first accelerated in a linear collider (LINAC 2) to an energy of 50 MeV before being injected into the proton synchrotron booster (PSB). The beams are then boosted to 1.4 GeV by a varying magnetic field in the circular PSB. Beams are then passed into the proton synchrotron

(PS) and then the super proton synchrotron (SPS) where the beam energy increases to 26 GeV and then 450 GeV. At this stage the beam is injected into the LHC and then accelerated to the final desired energy. The design energy is 7 TeV per beam for a total of 14 GeV centre of mass energy. The whole process can take a couple of hours, from the initial injection of the protons to stable beam conditions in the LHC.

As bunches overlap the protons that make up the bunches interact, the result of this interaction is known as an event. The number of events is proportional to the instantaneous luminosity $\mathcal{L}$ of the collider. $\mathcal{L}$ is a measure of the flux of particles per unit area per unit time can be defined as:

$$\mathcal{L} = f n_b \frac{N_1 N_2}{A} \tag{4.1}$$

where f is the frequency of revolution of the beam, n_b the number of colliding pairs of bunches in the beam, N_1 and N_2 are the number of particles in each colliding bunch and A is the cross section of the beam [59]. The peak luminosity evolution at the LHC is shown in Figure 4.2b.

The total amount of data collected is measured by the integrated luminosity $\mathcal{L}_{\text{int}}$ defined as the time integral of $\mathcal{L}$. Integrated luminosity has units of inverse area, usually expressed in terms of barns (b)[1]. The probability for a given process to occur is expressed as the cross section σ and the total number of events which proceed via said process is defined as:

$$\sigma \int \mathcal{L}\, \mathrm{d}t \tag{4.2}$$

The integrated luminosity delivered by the LHC and collected by the ATLAS detector in 2011 and 2012 is shown in Figure 4.3. The ATLAS detector does not record all data delivered by the LHC; approximately 6.5% was not recorded.

4.1.1 Pile-up

Due to the large number of interactions and the short time between collisions, multiple events can overlap into a single event. This has detrimental effects on physics analyses and is a determining factor in setting the instantaneous luminosity with which to perform data collection. This overlapping effect is collectively known as pile-up and is categorized into two types:

[1] $1\,\mathrm{b}^{-1}=10^{-28}\,\mathrm{m}^{-2}$

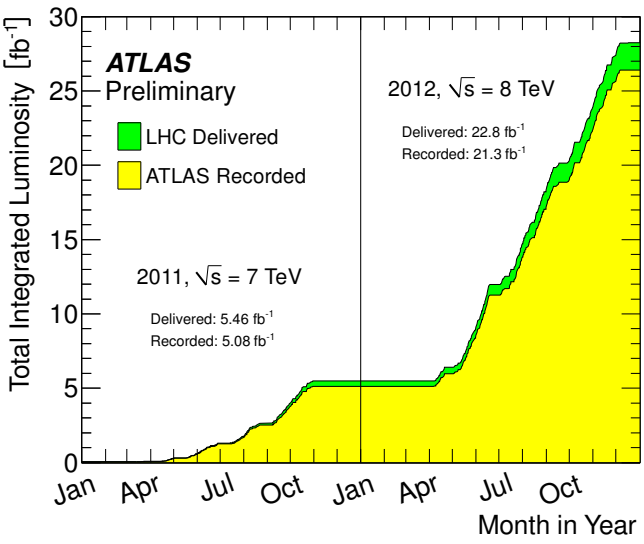

Figure 4.3: Distribution of the total integrated luminosity delivered by the LHC and the recorded by ATLAS for the 2011 and 2012 pp collision period [58, 59].

in-time pile-up, where multiple pp collisions occur during the same bunch crossing; and out-of-time pile-up, where the electric signals produced by previous collisions still remain to be read-out. This occurs when the time spacing between interactions is smaller than the read-out speed of the electronics. The number of interactions per crossing μ is shown in Figure 4.4, note that on average approximately thirty interactions occurred per bunch crossing in 2012. In comparison, in 2011 the average interactions per bunch crossing $\langle\mu\rangle$ varied from 5 in early 2011 to 15 at the end of the year.

4.2 The ATLAS detector

The ATLAS [9] experiment is a general-purpose detector which wraps around the IP providing large angular coverage. ATLAS is approximately cylindrical with a diameter of 25 m, a total length of 44 m and weighs 7000 t. The detector is made of several layers of instrumentation located at successively increasing radii as shown in Figure 4.5:

1. **Inner Detector (ID)**: Located nearest to the beam-pipe and designed to measure the track of charged-particles.

2. **EM Calorimeter**: Used for identification and measurement of electrons and photons.

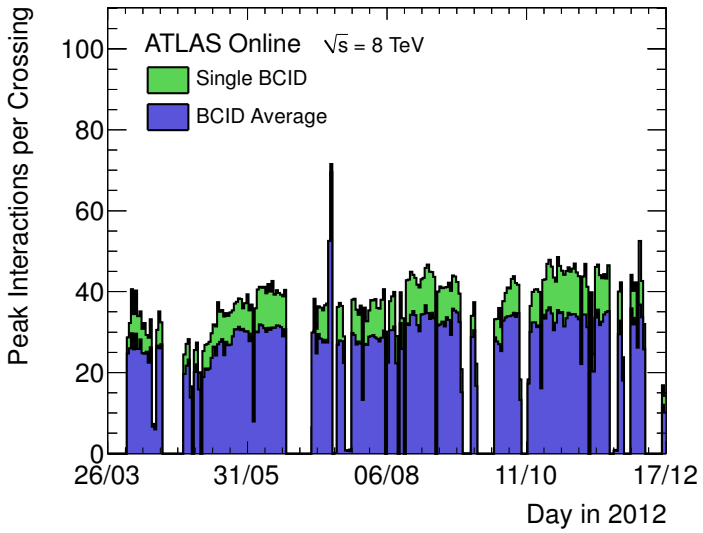

Figure 4.4: Number of interactions per bunch crossing for the 2012 pp data-taking period at ATLAS per day. Both the average number of interactions for all bunches and the maximum number of interactions are shown [58].

3. **Hadronic Calorimeter**: Used for the measurement of hadronic activity from hadronizing partons and missing transverse energy.

4. **Muon Spectrometer (MS)**: The outermost detection layer, used for muon identification and measurement.

Between these detection layers are magnets responsible for bending the path of the charged particles for the purpose of momentum measurement and particle identification. Triggering and data acquisition (TDAQ) systems also form part of the detector for the purposes of recording the data signals coming from the tracking and measurement systems. A brief description of these is provided in the coming sections. For a more detailed technical description of the detector and all subsystems see [9].

Lepton plus jets $t\bar{t}$ events produce a final state that includes hadronic activity, electrons, muons and missing energy, so all elements of the detector are used in the reconstruction of such events. Additionally, the match χ^2_{match} tagger which is central to this thesis, relies on the reconstruction and fitting of ID tracks and MS tracks. A detailed description of this algorithm is provided in Section 5.2.2.

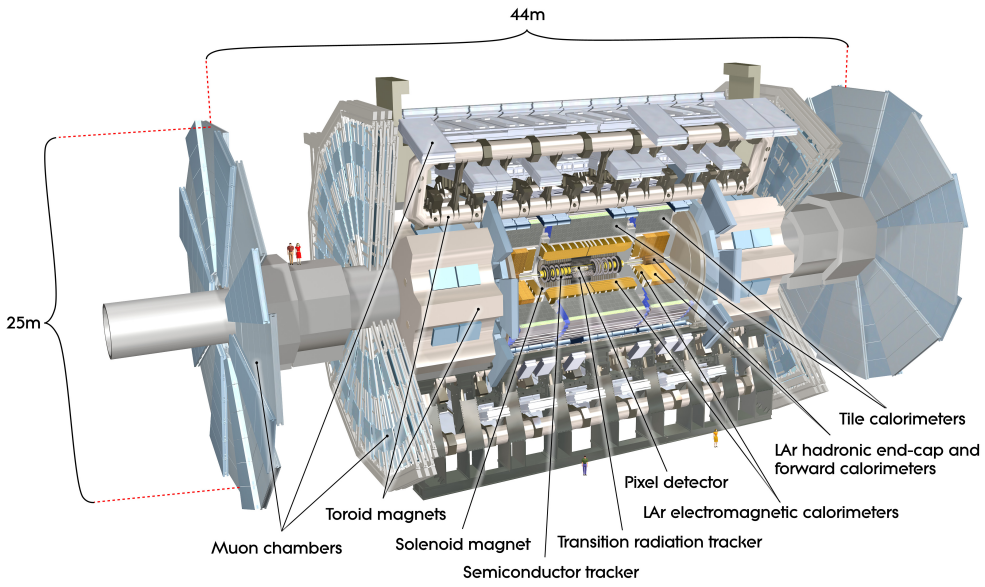

Figure 4.5: An overview diagram of the ATLAS experiment. Shown are all detection and tracking systems and the toroid magnet which encompasses them. Note also the muon system on the outside of the detector [9].

A cylindrical coordinate system as used by all ATLAS publications has been adopted here. The coordinate system is constructed so that the z-axis is parallel to the beam axis, and is positive in the direction of LHCb. The x-axis is positive in the direction going from the IP to the centre of the LHC ring, and the positive y-axis points upwards. Thus the x-y plane is transverse to the beam direction. All transverse variables such as the transverse momentum p_{T}, transverse energy E_{T} and missing transverse energy $E_{\mathrm{T}}^{\mathrm{miss}}$ are measured along this plane. The distance perpendicular to the beam-pipe is denoted by R, the azimuthal angle ϕ is measured around the beam axis, and the polar angle θ is the angle from the beam axis. The pseudorapidity is defined as $\eta = -\ln\tan(\theta/2)$. The distance in the η-ϕ plane between two objects is denoted by ΔR and defined as $\Delta R = \sqrt{\Delta\eta^2 + \Delta\phi^2}$. Finally side A of the detector is defined as the positive z side and side C is the negative z. The transverse impact parameter d_0 is defined as the distance of closest approach (perigee) of a track to the primary vertex (PV), and the longitudinal impact parameter z_0 is the distance in z between the perigee and the primary vertex.

4.2.1 Inner detector

The inner detector, shown in Figure 4.6, is a tracking detector located closest to the beam-pipe and used for momentum and impact parameter measurement, vertex and track reconstruction, and particle identification. The ID is designed to provide hermetic high-resolution tracking in the range $|\eta| < 2.5$.

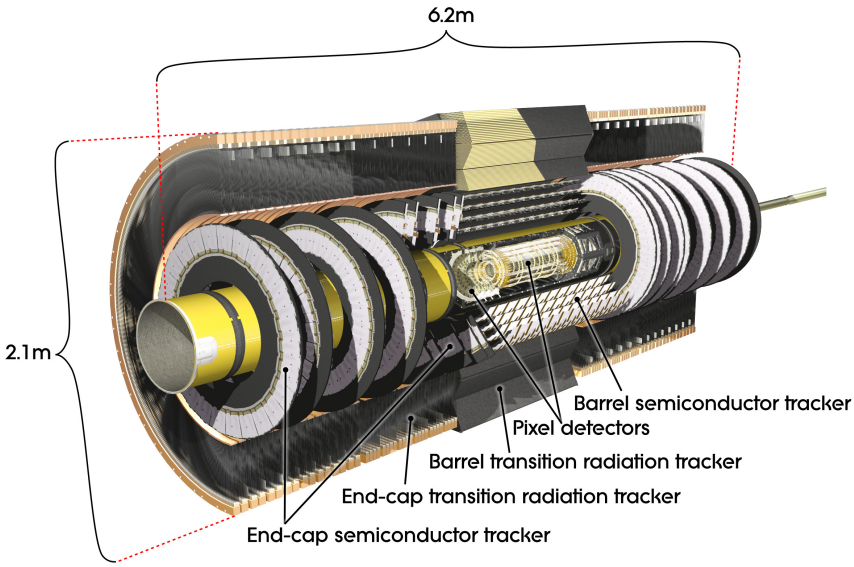

Figure 4.6: Drawing of the ATLAS inner detector [9].

The entire ID is contained within the central solenoid (CS) that generates a 2 T magnetic field for the purpose of momentum measurement. The trajectory of a charged particle is bent in the presence of a magnetic field by an amount proportional to the momentum of the particle

$$r = \frac{p_{\mathrm{T}}}{qB} \tag{4.3}$$

where r is the bending radius, p_{T} is the transverse momentum of the particle, q is the charge of the particle, and B is the magnetic field strength. Thus the momentum of the particle can be measured by reconstructing its trajectory through the detector. A particle with larger p_{T} would have a more straight trajectory than a particle with low p_{T} in the same magnetic field. For a central track with $p_{\mathrm{T}} = 5\,\mathrm{GeV}$ the relative resolution on the measured transverse momentum is $\sim 1.5\,\%$ [9].

The reconstruction of interaction vertices is paramount, particularly when considering the

large amount of pile-up observed at ATLAS. Interaction vertices are reconstructed by fitting all reconstructed tracks to a point. The primary vertex (PV) is then defined as the vertex with the largest amount of momentum associated with it. The reconstruction of secondary interaction vertices is used for the identification of short-lived particles such as B-hadrons and τ.

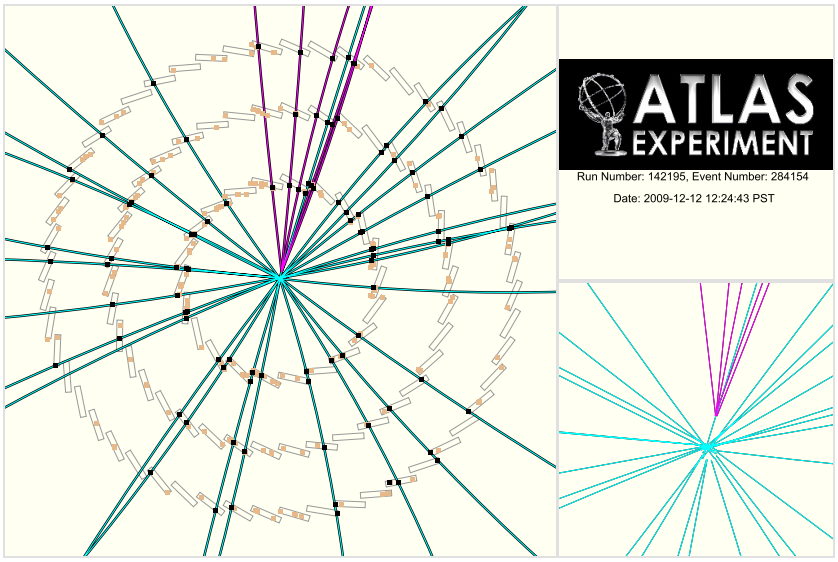

Figure 4.7: An event display of an event as reconstructed by the ATLAS inner detector [9]. Shown are the results of the vertexing algorithm where each line represents a track. The purple tracks have been fitted to a secondary vertex.

The ID is made of three separate tracking and detection systems located at increasing radii away from the beam-pipe, the full arrangement can be seen in Figure 4.8, and a plane-view is shown in Figure 4.9.

Pixel detector

The pixel detector is located nearest to the beam-pipe and provides high-granularity and precision for secondary vertex reconstruction. As a charged particle passes through a silicon pixel, several electron-hole pairs are created. The electrons and holes begin drifting in opposite directions under the influence of a voltage, and the charges are read out as a *hit* through an electrode. The pixel detector consists of three silicon pixel sensor layers in the barrel region located at approximately 5 cm, 9 cm and 12 cm from the IP, and three disks at each side located at constant R providing coverage up to $|\eta| < 2.5$. The barrel modules are overlapped in a turbine pattern to provide hermetic coverage. In the barrel region the modules provide an

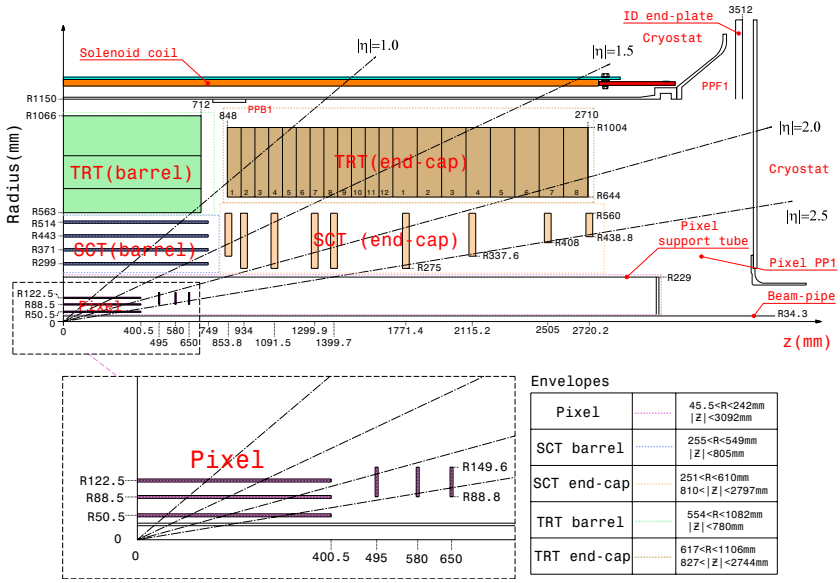

Figure 4.8: Plan-view of a quarter-section of the ATLAS ID showing the major detector elements with its active dimensions and envelopes [9]. Note also the η markers showing the maximum coverage up to $\eta = 2.5$.

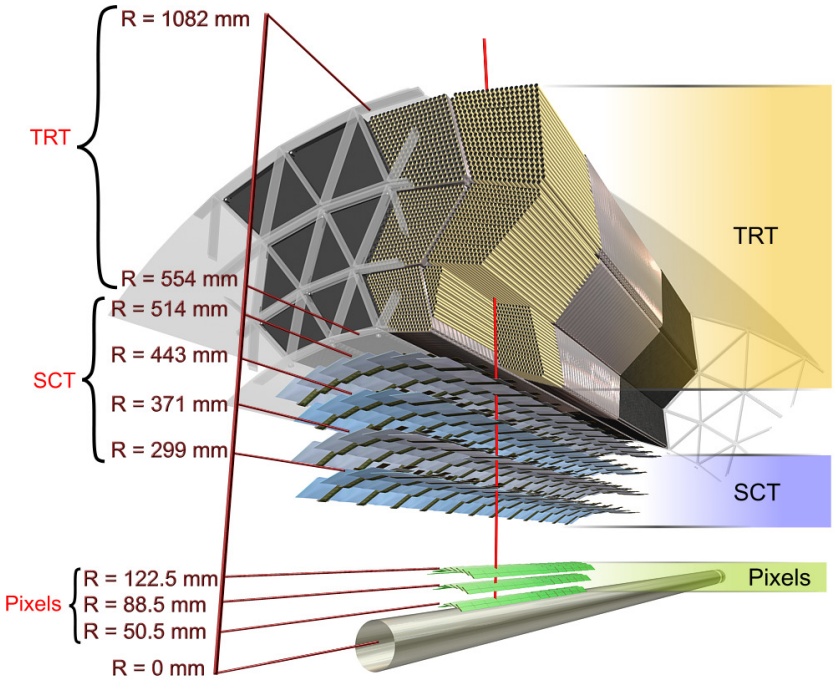

Figure 4.9: A drawing in the transverse plane of the ATLAS ID showing all major detection elements in the barrel regions [9]. A charged particle track is shown traversing all the detector elements as a solid line.

intrinsic resolution of 10 µm in R-ϕ and 115 µm in z [9]. The disk sections have an intrinsic resolution of 10 µm (R-ϕ) and 115 µm (R).

Semiconductor tracker

The semiconductor tracker (SCT) located in the intermediate radius range is designed to provide eight hits per track contributing to the measurement of momentum, impact parameter, and vertex position. The SCT is made of four layers of stereo-pair silicon micro-strip sensors in the barrel region at increasing radii. The intrinsic resolutions are 17 µm (R-ϕ) and 580 µm (z). At the end-caps nine disks of silicon micro-strip modules provide large pseudorapidity coverage with a resolution of 17 µm (R-ϕ) and 580 µm (R) [9].

Transition radiation tracker

The transition radiation tracker (TRT) is the outermost tracking layer of the ID, and acts as both a tracker and transition radiation detector. Transition radiation (TR) is produced when a charged particle crosses the boundary between two materials with different dielectric constants. The probability of producing TR photons depends on the Lorentz factor of the particle $\gamma = E/m$. Thus for two particles of the same energy, a lighter particle will, on average, emit more ionization than a heavier particle.

The TRT is designed to provide up to 36 hits per track using straw-tube sensors. Each straw is 4 mm in diameter and is made of two 35 µm thick Kapton multi-layer films bonded back-to-back. At the centre of each straw is a gold-plated tungsten wire with a diameter of 31 µm. Each straw is filled with a mixture of gas (70 % Xenon, 27 % CO_2 and 3 % O_2). The tubes are surrounded by polypropylene-polyethylene fibres that act as radiators and allow for the production of TR, which later ionizes the gas mixture and is read-out through the gold-plated wire.

In the barrel, the 144 cm long straw-tubes are arranged in modules which contain between 329 and 793 straws. The end-cap disks are made of radially distributed 36 cm long straw-tubes. Each tube provides an intrinsic resolution of 130 µm along its length [9]. The combination of a large number of hits over a large radius allows measurements in the TRT to be made with an accuracy that can complement those made by the pixel detector.

4.2.2 Calorimetry

The ATLAS calorimeter is responsible for the measurement of the energy of particles that emerge from the event. Sampling calorimeters are used for this purpose, layers of absorber material (passive) are placed in the path of the particles forcing them to interact and shower. The amount of energy lost by the incident particle depends on the type of material the particle traverses, the energy of the particle, and the type of particle. At high energy, electrons lose energy predominantly via Bremsstrahlung, while the energy of photons is dissipated via pair production. The characteristic length associated with this energy loss is a material property known as the radiation length X_0.

For electrons, the energy as a function of material length traversed is

$$E = E_0 e^{-x/X_0} \tag{4.4}$$

where E_0 is the initial energy, x is the distance traversed, and E is the energy of the particle at x. As an electron traverses one X_0 of material, its energy is reduced by a factor of $1/e$. For photons, the average number of photons traversing through a material length x is reduced exponentially by a factor of $\frac{7}{9}X_0$ [60]. Thus the longitudinal length of the shower is proportional to the logarithm of the energy of the incoming particle.

The number of shower particles changes as a function of the hadronic interaction length λ_{int} as

$$N = N_0 e^{-x/\lambda_{\text{int}}} \tag{4.5}$$

where N is the number of shower particles at length x and N_0 is the initial number of incident particles. This is the characteristic length used when discussing the construction of the hadronic calorimeter. For a given material the λ_{int} is much larger than X_0, therefore hadronic showers tend to be much broader and deeper than EM showers. Note that on average $1/3$ of the particle content of hadronic showers is electromagnetic, mostly due to pion decay into photons.

The energy of the resulting shower is measured by some sampling material (active) located behind the absorbers, this energy is proportional to the energy of the incident particle.

The type and thickness of material used is varied through the pseudorapidity range to

improve energy measurement and reduce punch-through of particles into the muon system behind. Due to the intense radiation produced during collisions, radiation hardness is also an important factor in material choice.

The ATLAS calorimeter consists of the EM calorimeter, designed to measure photons and electrons covering $|\eta| < 3.2$; the hadronic calorimeter (HCal), which measures hadronic activity at $|\eta| < 3.2$; and the forward calorimeter (FCal) which provides energy measurement capability in at $3.1 < |\eta| < 4.9$. As can be seen in Figure 4.10, the calorimetry envelopes the ID and CS providing hermetic coverage symmetric in ϕ. This is particularly important for the measurement of $E_{\mathrm{T}}^{\mathrm{miss}}$ resulting from weakly interacting particles escaping the detector.

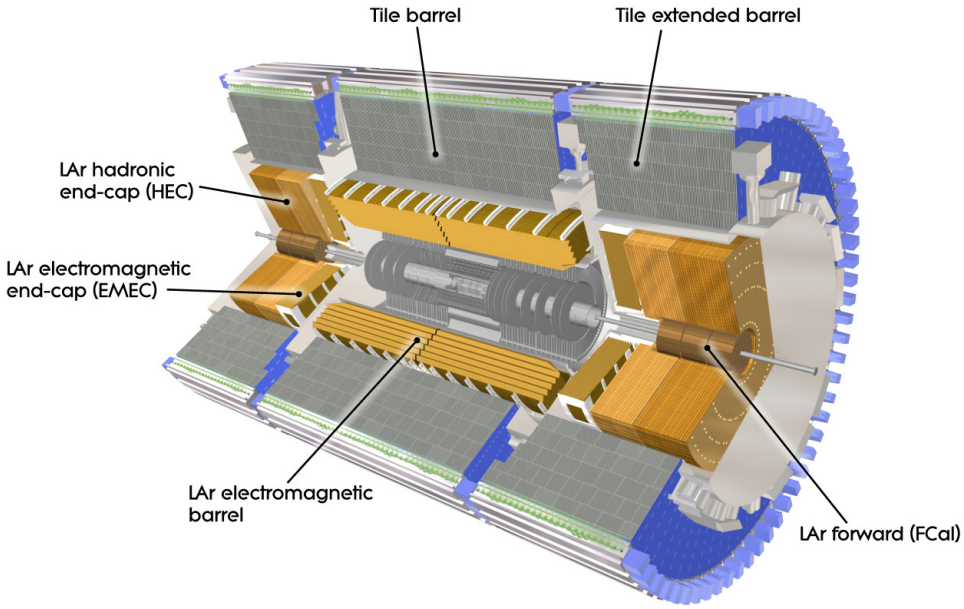

Figure 4.10: A cut-away diagram of the ATLAS detector highlighting the calorimetry system. Shown are the ECal barrel and end-cap, the HCal barrel and end-cap and the FCal end-cap [9].

Electromagnetic calorimeter

The EM calorimeter is made of a barrel section ($|\eta| < 1.475$) and two end-caps ($1.375 < |\eta| < 3.2$). The barrel consists of two half-barrels separated by a 4 mm gap at $z = 0$. The end-caps consist of two coaxial wheels, the outer ring covering $1.375 < |\eta| < 2.5$ and the inner ring covering the range $2.5 < |\eta| < 3.2$. The pseudorapidity region $1.37 < |\eta| < 1.52$, known as the "crack" region, is not used for precision physics due to the large amount of material

between the interaction point and the calorimeter.

The EM calorimeter employs liquid argon (LAr) as the active material due to its intrinsic radiation hardness and response over time, and lead as the passive material arranged in an accordion geometry for full ϕ symmetry. Particles interact with the lead absorbers creating a shower which ionizes the layers of LAr. A potential is applied across the LAr material allowing for signal read-out via Kapton/copper electrodes. The total thickness of the EM calorimeter is $> 24X_0$ in the barrel and $> 26X_0$ in the end-caps. The amount of material is optimized in pseudorapidity to enhance energy resolution. The amount of material, measured in terms of X_0, before and in the EM calorimeter is shown in Figure 4.11.

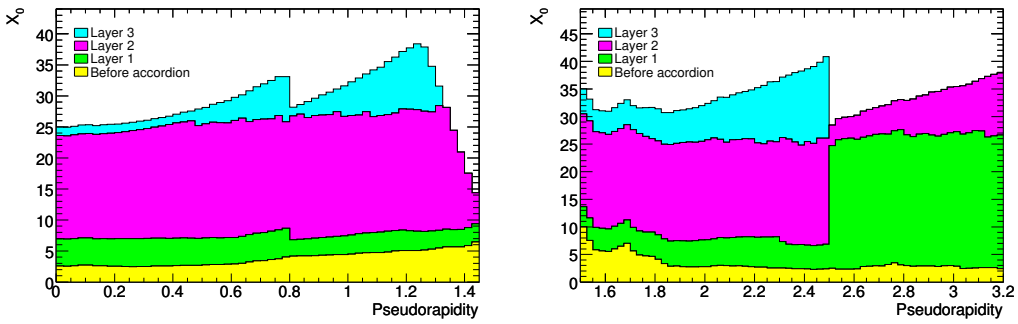

Figure 4.11: Cumulative amounts of material, in units of radiation length X_0, as a function of $|\eta|$ in front and in the EM calorimeter at the ATLAS detector [61]. The left-hand plot shows the amount of material in the barrel region and the right-hand plot shows the material in the endcap region.

In the region devoted to precision physics the EM calorimeter is divided into three segments as shown in Figure 4.12, the strip layer is designed to improve particle identification and pseudorapidity measurement. The design energy resolution for all components of the calorimeter are shown in Table 4.1.

Hadronic calorimeter

The hadronic calorimeter uses different types of passive and active material to accommodate for the varying conditions in different regions of the detector. The structure of the detector and the materials used must provide good energy resolution, full symmetric coverage for the purpose of $E_{\mathrm{T}}^{\mathrm{miss}}$ measurement, full containment of all hadronic activity to prevent punch-through to the muon system, and be sufficiently radiation hard. The hadronic calorimeter

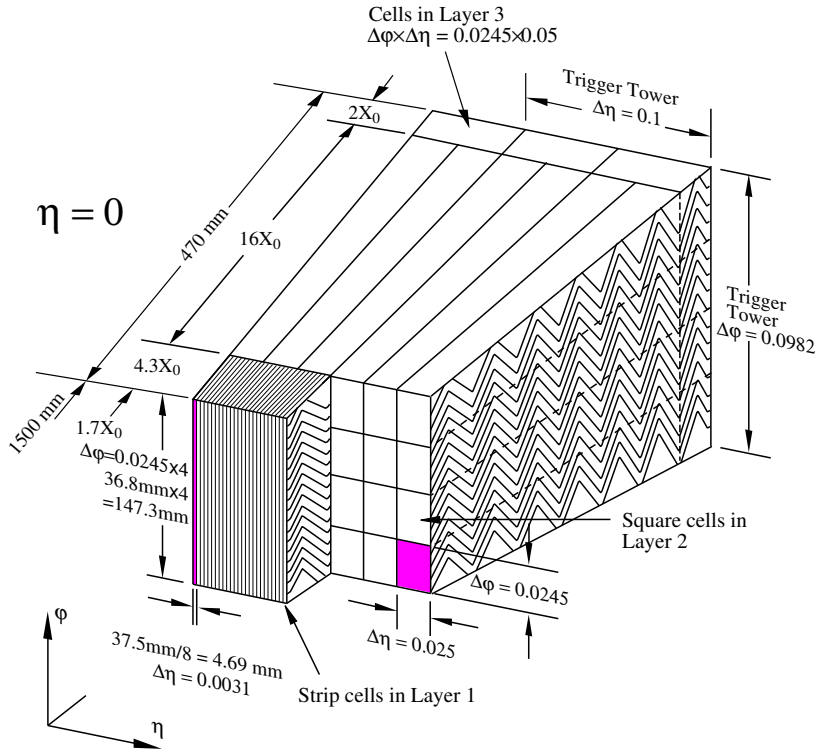

Figure 4.12: Cut-away diagram of the EM calorimeter barrel at $\eta = 0$ [9]. Shown are the three different layers with varying cell structures. The strip section is designed to enhance particle identification and position measurement in η.

Section	Resolution
EM barrel	$\frac{10\%}{\sqrt{E}} \oplus 0.7\%$
EM endcap	$\frac{10\%}{\sqrt{E}} \oplus 0.7\%$
HCal barrel & endcap	$\frac{50\%}{\sqrt{E}} \oplus 3\%$
Forward	$\frac{100\%}{\sqrt{E}} \oplus 10\%$

Table 4.1: Design energy resolution of all ATLAS calorimeter components [9]. The resolution is made of a sampling term ($1/\sqrt{E}$) associated with the choice of passive and active materials and the construction of the layers, and a constant term associated with the depth of the detector, cracks and dead material.

consists of two parts: a scintillator tile calorimeter in the barrel region and a LAr calorimeter in the end-cap.

The tile calorimeter is located directly outside the EM calorimeter. The barrel portion covers $|\eta| < 1.0$ and the two extended barrels cover the range $0.8 < |\eta| < 1.7$. The tile calorimeter uses steel as the passive material and scintillating tiles as the active material. The resulting hadronic showers enter the scintillating tiles and produce photons which are passed to photomultiplier tubes. The total detector thickness which is tile-instrumented is $9.7\lambda_{\text{int}}$ at $\eta = 0$.

The hadronic end-cap (HEC) uses LAr technology due to its radiation-hardness in this challenging high pseudorapidity region. The HEC consists of two independent wheels per end-cap covering the range $1.5 < |\eta| < 3.2$ overlapping the tile calorimeter at low pseudorapidity and the forward calorimeter located at high pseudorapidity.

Forward calorimeter

The forward calorimeter (FCal) is responsible for energy measurement in the very high pseudorapidity range $3.1 < |\eta| < 4.9$ of both electromagnetic and hadronic activity. Due to the large amount of radiation in this region, LAr is employed as the active material. The FCal consists of three layers: the first made primarily of copper, designed mostly for the measurement of electromagnetic activity, while the two outer tungsten layers are responsible for hadronic activity measurement.

4.2.3 Muon spectrometer

The muon spectrometer is the outermost layer of the ATLAS detector (Figure 4.13) and is responsible for the precision measurement of p_{T} of charged-particles that pass-through the ATLAS calorimetry. It is designed to have a precision of $10\,\%$ at a momentum of $1\,\mathrm{TeV}$ [9]. Muon tracking performance is vital to the SMT tagger described in Section 5.2.4, as it relies on the precise reconstruction of muon tracks in the ID and MS.

Due to their larger mass, muons tend to have a larger transverse momentum and do not lose as much energy through photon emission. As a result, muons tend to traverse the hadronic calorimeter and escape the detector volume. The muon system provides measurement of these particles up to $|\eta| < 2.7$ and triggering up to $|\eta| < 2.4$. Measurement of p_{T} is facilitated by the magnetic field generated by the large toroid magnet in the barrel region $|\eta| < 1.4$ and two smaller end-cap magnets in $1.6 < |\eta| < 2.7$. In the transition region at $1.4 < |\eta| < 1.6$, deflection is provided by both barrel and end-cap fields.

The structure of the MS is delimited by the magnet system. In the barrel region, three cylindrical layers of precision-tracking chambers are located in and on the coils of the barrel toroid magnet at radii of $5\,\mathrm{m}$, $7.5\,\mathrm{m}$ and $10\,\mathrm{m}$. End-cap region coverage is provided by three chamber planes perpendicular to the z-axis. These are located in front and behind the end-cap toroid magnet at distances $|z| \approx 7.4\,\mathrm{m}$, $10.8\,\mathrm{m}$, $14\,\mathrm{m}$ and $21.5\,\mathrm{m}$ from the interaction point.

The MS contains four different types of chambers responsible for precision-tracking and/or triggering in various pseudorapidity ranges, as shown in Table 4.2. The arrangement of these chambers is shown in Figure 4.14.

In the barrel region, precision-measurement is performed by monitored drift tube (MDT) chambers. These chambers consist of three to eight pressurized aluminium drift tubes, each containing a tungsten-rhenium wire anode and a mixture of argon and carbon dioxide gas. An average spatial resolution of $80\,\mu\mathrm{m}$ per tube and $35\,\mu\mathrm{m}$ per chamber is achieved. The end-cap region is instrumented with cathode-strip chambers (CSC) due to their higher rate capability and time resolution. CSCs are multi-wire chambers with cathode planes segmented into strips in orthogonal directions, this allows both coordinates to be measured simultaneously. The resolution of a chamber is $40\,\mu\mathrm{m}$ in the bending plane (R-z) and $5\,\mathrm{mm}$ in the transverse plane. Triggering on muon tracks is another essential role of the muon spectrometer. To this end, each precision-measurement chamber is complemented with fast triggering chambers. As with

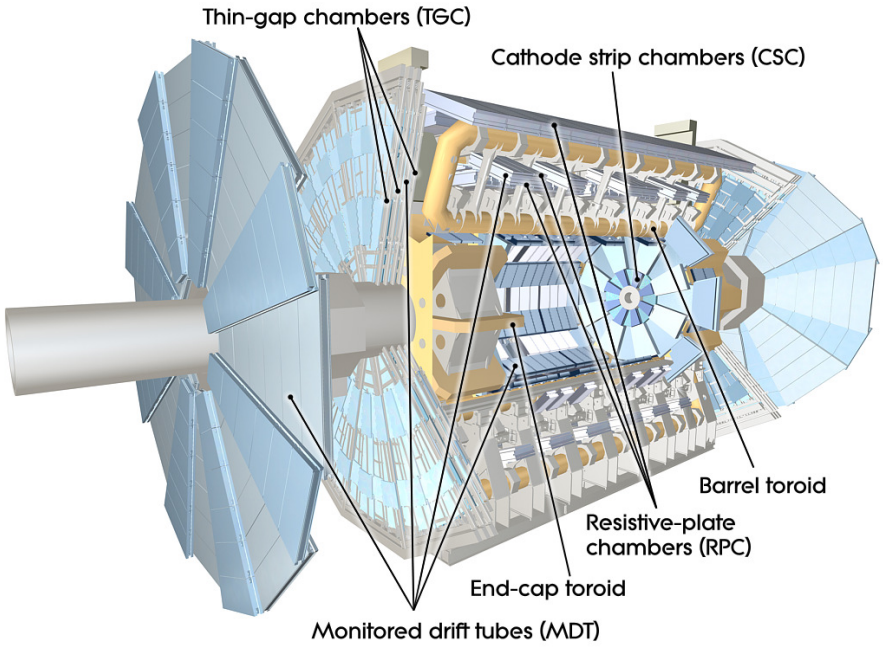

Figure 4.13: Cut-away drawing of the ATLAS muon system [9].

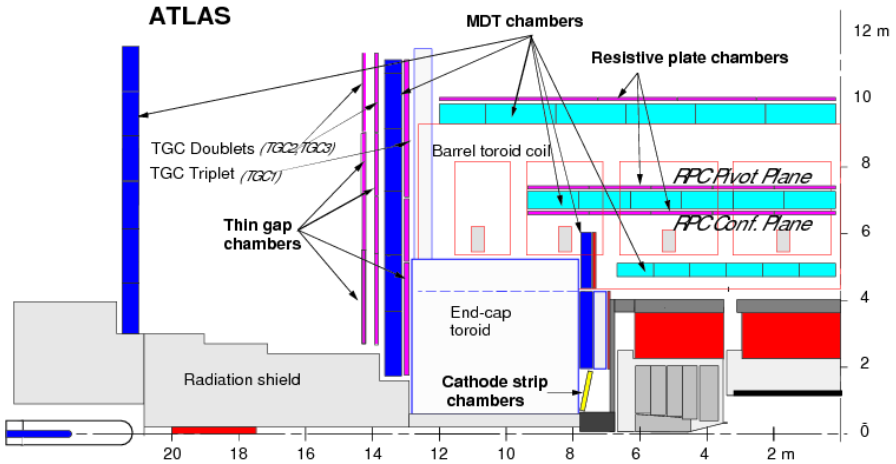

Figure 4.14: Plan view of quarter-section of the ATLAS muon spectrometer [62].

Monitored drift tubes	**MDT**
— Coverage	$\|\eta\| < 2.7$ (innermost layer: $\|\eta\| < 2.0$)
— Number of chambers	1150
— Function	Precision tracking
Cathode strip chambers	**CSC**
— Coverage	$2.0 < \|\eta\| < 2.7$
— Number of chambers	32
— Function	Precision tracking
Resistive place chambers	**RPC**
— Coverage	$\|\eta\| < 1.05$
— Number of chambers	606
— Function	Triggering, second coordinate
Thin gap chambers	**TGC**
— Coverage	$1.05 < \|\eta\| < 2.7$ (2.4 for triggering)
— Number of chambers	3588
— Function	Triggering, second coordinate

Table 4.2: Main parameters of the muon system [9].

the measurement layers, two different types of chambers are used for the barrel and end-cap regions. In the barrel region ($|\eta < 1.05$), resistive plate chambers (RPC) are attached to the same support structure as the MDTs. The RPCs are made of two resistive plates, 2 mm apart, between which a potential difference is applied. The gap between the plates is filled with a mixture of $C_2H_2F_4$/Iso-C_4H_{10}/SF_6. The signal is read out via metallic strips mounted to the outer faces of the resistive plates. The end-cap region ($1.05 < |\eta| < 2.4$) is populated with thin gap chambers (TGC). TGCs are multi-wire chambers like those used in the CSC, however the distance between the wire and the cathode is smaller in the TGC. A summary of the spatial and temporal resolution for the measurement and triggering layers is shown in Table 4.3.

4.2.4 Magnet system

The structure of the ATLAS detector is defined by its large magnet systems as shown in Figure 4.16. The system consists of two sets of magnets: the CS and three air-core toroids.

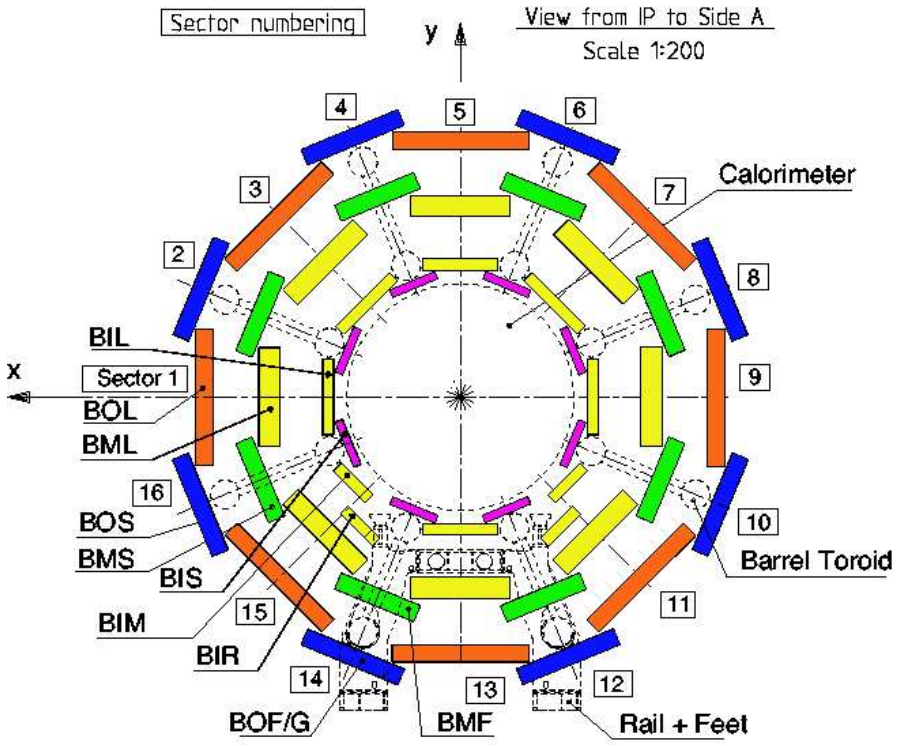

Figure 4.15: Transverse view of the muon system [9].

The CS is located nearest to the beam and provides a 2 T magnetic field for the ID for the purpose of tracking, particle identification and p_{T} measurement.

The barrel toroids extend to $|\eta| < 1.4$ and are made of eight coils, generating a $0.5\,\mathrm{T}$ magnetic field for the MS. In the high pseudorapidity range, magnetic deflection is provided by two end-cap toroids extending from $1.6 < |\eta| < 2.4$. As in the barrel, the end-cap toroids are made of eight coils offset by $22.5°$ with respect to the barrel coils. Each end-cap generates a $1\,\mathrm{T}$ magnetic field for the MS. The so-called transition region between the two magnets is covered by the overlap of the end-cap and barrel fields.

4.2.5 Beam-pipe

The beam-pipe section located within the ATLAS experiment is approximately 38 m in length and made of seven parts. The central chamber has an inner diameter of 58 mm and is constructed from $0.8\,\mathrm{mm}$ thick beryllium due to the material's transparency to particles, high specific stiffness and compatibility with ultra-high vacuum. The beam-pipe is centred around the IP and integrated with the pixel detector. The additional layers are made of stainless steel

Chamber	Resolution in		
	R/z	ϕ	Time
MDT	35 µm (z)	—	—
CSC	40 µm (R)	5 mm	7 ns
RPC	10 mm (z)	10 mm	1.5 ns
TGC	2-6 mm (R)	3-7 mm	4 ns

Table 4.3: Summary of spatial and temporal resolutions per chamber for all chamber types used in the ATLAS muon spectrometer. Adapted from [9].

located symmetrically on both sides of the IP.

4.2.6 Triggering and data-acquisition

At the design luminosity of the LHC $\mathcal{L} = 10 \times 10^{34}\,\mathrm{cm}^{-2}\,\mathrm{s}^{-1}$, the expected bunch crossing rate is approximately 40 MHz. At an average event size of 1.3 MB per event, the total amount of data produced at ATLAS is $50\,\mathrm{TB\,s}^{-1}$. The maximum rate of data storage at ATLAS is approximately $300\,\mathrm{MB\,s}^{-1}$, so the rate must be reduced.

The trigger and data acquisition system (TDAQ) is responsible for reducing the rate by recording only "interesting" events. This is known as *online selection* as it happens before the data is stored. In contrast, *offline selection* happens after the data has been recorded, for example when performing a cross section measurement. The overwhelming majority of events produced at the LHC are of no interest to physics analysis.

At ATLAS, trigger decisions are carried out in three sequential levels: *Level 1* (L1), *Level 2* (L2) and *Event Filter* (EF), each successive level reduces the rate by applying more complex selection criteria. The hardware-based L1 trigger, performs the initial selection based on reduced-granularity information from the MS trigger chambers and all calorimeters. Data from the calorimeter trigger towers, shown in Figure 4.12, is used to search for high transverse-momentum muons, photons, electrons, hadronic decays of τ leptons, hadronic jets, large missing transverse energy, and large total transverse energy. The central trigger processor applies the trigger 'menu' which includes a combination of selection criteria. Events which are of interest to physics analyses can be produced at such a rate as to overwhelm the capabilities of the DAQ. A trigger can be configured with a so-called *prescale* that reduces the amount of data

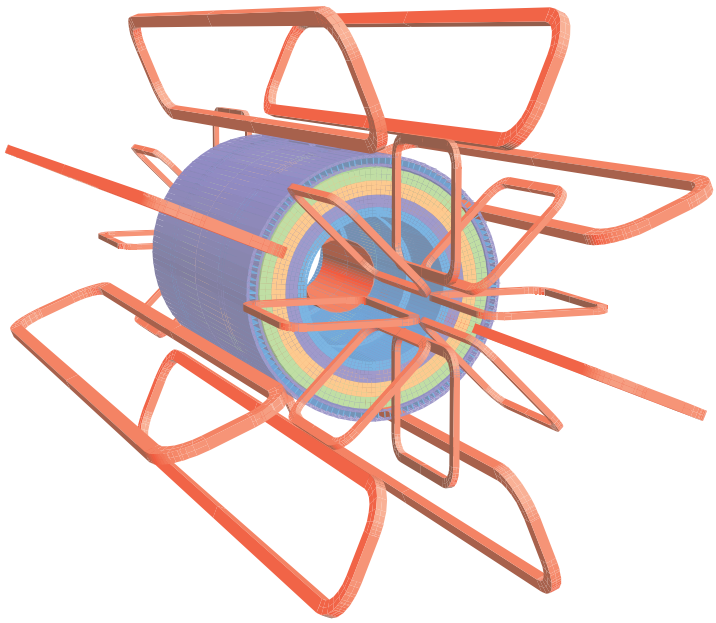

Figure 4.16: Diagram of the ATLAS toroid magnet system [9]. The red central solenoid is located closest to the beam surrounded by layers of tile calorimetry. The eight barrel toroid magnets are shown along with the offset end-cap toroids at each end.

recorded. There are two types of prescale, a deterministic prescale that records one event in every S events firing the trigger, and a non-deterministic prescale which records events with a probability $1/S$ based on the outcome of a pseudo-random number generator [63].

The L1 trigger also constructs *regions of interest* (RoIs) around the detector where interesting features have been found. The η and ϕ information of the RoI along with information about the decision is stored and passed to the higher level triggers.

The L2 selection makes use of RoIs and the full granularity of the detector to further reduce the event rate to approximately 3.5 kHz, and finally the EF implements selections commonly used for offline analysis to reduce the rate to 200 Hz.

Chapter 5

Data Simulation and Object Selection

5.1 Monte Carlo simulation

The simulation of data is paramount to HEP research, from the initial detector design phase all the way through to finalized analyses. Monte Carlo (MC) generators simulate various interactions, creating kinematic collision event data that reflect our best understanding of nature. These processes are then passed through detector simulation and all the object reconstruction algorithms, resulting in a dataset with an identical format to collision data. More information on the ATLAS simulation infrastructure can be found in [64].

The simulation of data happens in three phases: event generation, detector simulation and digitization.

5.1.1 Event generation

Event generators model complex physics processes that occur during a particle collision. Many different generators exist to model a variety of beam types (pp, $p\bar{p}$, e^+e^-, etc...) and event types. Hadronic event generators simulate all components of the interaction: the hard scattering process, parton showering, hadronizing, hadronic decay, the underlying event, and photon radiation [65]. A schematic diagram of a hadronic event as modelled by an event generator is shown in Figure 5.1.

First, the *hard interaction* of a pair of partons originating from the colliding protons is simulated. An example of such an interaction is $q\bar{q} \to Z/\gamma^* \to e^+e^-$. Calculating the cross

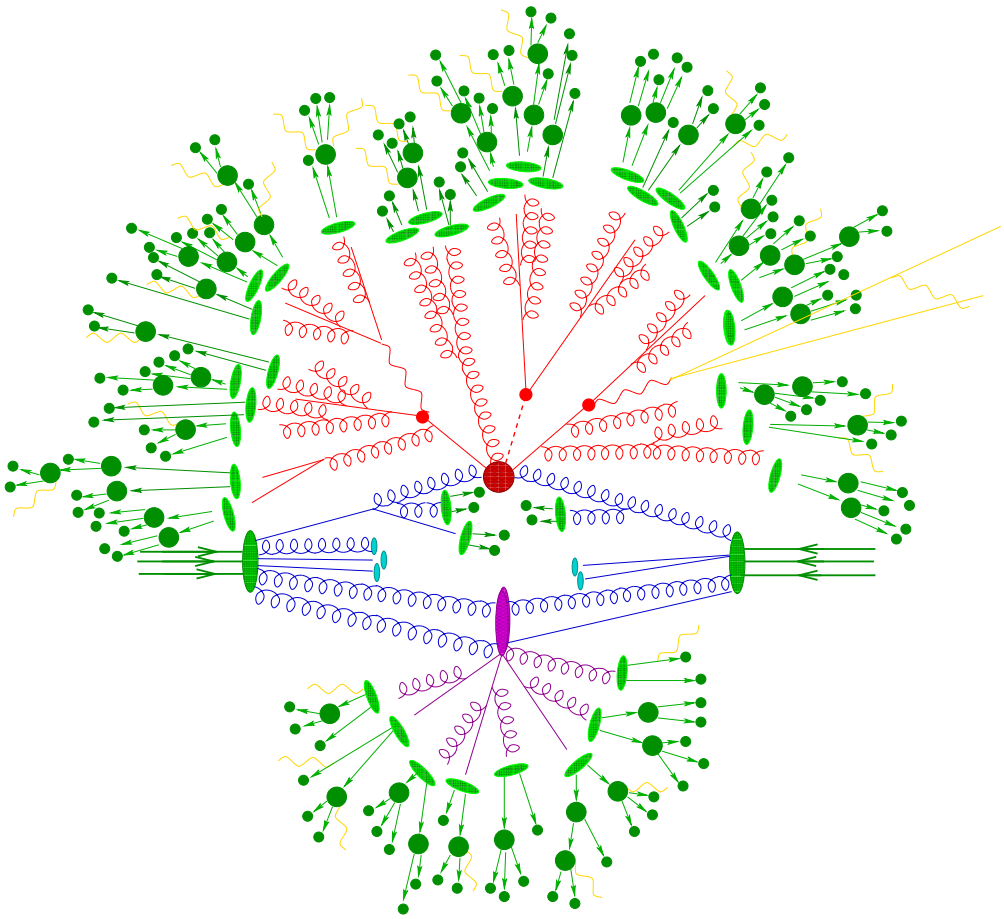

Figure 5.1: Sketch of a proton-proton collision as modelled by the event generator [66]. Shown are the incoming protons beams as green arrows on the left and right sides of the diagram. The partons shown in blue, interact in the hard interaction (red blob) producing a parton shower, also depicted in red, which eventually hadronize (light green blobs) and finally decay into final state particles shown in dark green. The *underlying event* is shown at the bottom of the diagram as the purple blob, note also the beam remnants as light blue blobs that also form part of the underlying event. Photon emission is shown in yellow and occurs at all stages of the event generation.

section for such an interaction involves the convolution of the parton density function (PDF) and the *matrix element* (ME).

The PDF $f_i(x, Q^2)$, describes the probability of finding, within the proton, a parton of flavour i carrying a fraction x of the proton momentum, via a hard interaction with energy scale Q. The ME describes the interaction between the two partons and corresponds to one or more of the Feynman diagrams associated with the interaction[1]. Different generators are capable of treating diagrams at different orders, though the hard interaction is usually modelled at LO or NLO.

The next step is *parton-showering* which simulates the emission of gluons by coloured partons and gluon splitting. A cascade of partons is produced, as shown in Figure 5.1, and modelled by perturbation theory for energies above 1 GeV. All coloured objects are then combined into colourless hadrons in a process known as *hadronization*, these hadrons are subsequently allowed to decay. Finally, the remaining coloured partons not involved in the hard interaction, are allowed to interact forming the *underlying event*. The kinematic information of the original event without the effects of the detector is kept in the data set and is usually referred to as the *truth information*.

5.1.2 Detector simulation

The generated events are then passed through a detector simulation that mimics the response of the detector to particles traversing through it. A description of the entire detector is implemented in the GEANT4 tool-kit [67], including a map of the magnetic fields, the position of the detector components and material description. The software then simulates the signal voltages produced in all tracking and calorimeter components of the detector, these are then passed through a simulation of the read-out electronics and TDAQ taking into account known losses and inefficiencies. All of this information is then passed on to the reconstruction software that "rebuilds" the physics objects from the detector hits.

[1]For a rigorous discussion of matrix elements and the Feynman rules, see [18, 3]

5.2 Object reconstruction

The process of converting the raw data from the detector into physics objects (electrons, muons and so on) is known as *object reconstruction*. The reconstruction algorithms are identical for both collision data and simulated data. As lepton plus jets decays of $t\bar{t}$ are the focus of this thesis, the reconstruction procedures of all types of objects (excluding photons) are relevant. This includes electron, muon and jet reconstruction as well as b-tagging algorithms. The soft muon tagger relies on *STACO combined* (STACO CB) muons, therefore some details of the muon reconstruction algorithms are discussed here.

5.2.1 Electron reconstruction

The electron reconstruction [68] procedure at ATLAS depends on the pseudorapidity of the candidate. Only electrons that lie within the coverage of the ID are used here, therefore only the relevant procedure is described. The algorithm used in the central region identifies energy deposits in the EM calorimeter and associates them with reconstructed ID tracks. Firstly, clusters are seeded from energy deposits with total E_{T} above 2.5 GeV using a sliding-window algorithm with window size 3×5 in units of 0.025×0.025 in (η,ϕ) space. Tracks with $p_{\mathrm{T}} > 0.5$ GeV are then extrapolated to the middle layer of the EM calorimeter[2] and matched to the cluster seed using cuts in the (η,ϕ) space. In case of multiple matches, tracks with pixel or SCT hits are given priority and the match with the smallest ΔR distance is chosen. Finally, the size of the cluster associated with the candidate electron is enlarged to 3×7 and 5×5 in the barrel and end-cap regions respectively. The energy of the electron is then the sum of four contributions taking into account energy deposited before the EM material, and leakages to other clusters as well as beyond the EM calorimeter.

Electron identification for central electron candidates is done by applying sequential cuts on calorimeter, tracking and combined track-cluster variables. Several sets of selection criteria, labelled *loose*, *medium* and *tight*, are designed for use in analyses. These sets provide increasing background-rejection power at the cost of efficiency by introducing new cuts at each stage, or by tightening previous cuts. The cut definitions are listed in Appendix A.

Additional requirements can be made on the so-called isolation of the electron. Three sets

[2] As it absorbs the largest fraction of the shower energy

of isolation strategies are used at ATLAS [69]:

- **Calorimeter isolation**: The calorimeter isolation $E_{\mathrm{T}}^{\mathrm{cone}\Delta R}$ is defined as the sum of transverse energy deposited in the cells around the electron in a cone of size ΔR. The contribution from the electron itself is removed within $\Delta\eta\times\Delta\phi = 0.125\times0.175$ around the electron cluster barycentre. It is corrected for energy leakage from the electron into the isolation cone and for the effect of pile-up. At ATLAS the nominal cone sizes used are ΔR=0.2, 0.3 and 0.4.

- **Track isolation**: The tracking isolation $N_{\mathrm{trk}}^{\mathrm{cone}\Delta R}$ is defined as the number of tracks in a cone around the electron, excluding the track of the electron itself.

- **Momentum isolation**: The momentum isolation $p_{\mathrm{T}}^{\mathrm{cone}\Delta R}$ is defined by the sum of the transverse momentum of tracks with $p_{\mathrm{T}} > 0.4\,\mathrm{GeV}$ in a cone around the electron, excluding the electron track itself.

5.2.2 Muon reconstruction

Muon reconstruction makes use of the information provided by both the inner detector and the muon spectrometer systems. Several different strategies exist [70]:

- **Standalone reconstruction**: Uses MS information only, first constructing *segments* from several hits in a given chamber and then fitting segments from all three stations to hits from the four MS components. Tracks are then extrapolated back to the interaction point taking into account energy loss and multiple scattering.

- **Tagging ID tracks reconstruction**: Uses MS or calorimeter information to tag ID tracks as muons. An ID track is segment-tagged (ST) if, once extrapolated to the MS, it is associated with at least one local track segment in the MDT or CSC chambers. An ID track is calorimeter-tagged (CaloTag) if it could be associated to an energy deposit in the calorimeter compatible with a minimum ionizing particle.

- **Combined track reconstruction**: Standalone muon tracks are extrapolated back to the vertex and matched to ID tracks within ($|\eta| < 2.5$) and combined. This results in an improved momentum sensitivity from ID and MS information.

These strategies can be implemented in a variety of ways. There are two prominent families, STACO and MUID, that contain reconstruction packages which exploit one or a combination of these strategies. The STACO combined algorithm is used by the SMT tagger and is described in more detail below.

STACO Combined algorithm

The STACO package [71] combines ID and MS tracks by performing a statistical combination of the two independent tracks using track parameters (η, ϕ, p_{T}, d_0, and z_0) and their covariance matrices. The quality of the fit is represented in the resulting χ^2_{match}:

$$\chi^2_{\mathrm{match}} = (\mathbf{T}_{\mathrm{MS}} - \mathbf{T}_{\mathrm{ID}})^T (\mathbf{C}_{\mathrm{MS}} + \mathbf{C}_{\mathrm{ID}})^{-1} (\mathbf{T}_{\mathrm{MS}} - \mathbf{T}_{\mathrm{ID}}) \tag{5.1}$$

where $\mathbf{T}_{\mathrm{MS}}$ and $\mathbf{T}_{\mathrm{ID}}$ contain the track parameters for the MS track and the ID track respectively,

$$\mathbf{T}_{\mathrm{MS\ or\ ID}} = \begin{pmatrix} \eta \\ \phi \\ p_{\mathrm{T}} \\ d_0 \\ z_0 \end{pmatrix} \tag{5.2}$$

and $\mathbf{C}_{\mathrm{MS}}$ and $\mathbf{C}_{\mathrm{ID}}$ are the covariance matrices, defined as

$$\mathbf{C}_{ij} = (\mathbf{T}_i - \langle \mathbf{T}_i \rangle)(\mathbf{T}_j - \langle \mathbf{T}_j \rangle) \tag{5.3}$$

where $\langle \mathbf{T}_i \rangle$ is the expectation value of $\mathbf{T}_i$. The full covariance matrix is shown in Appendix C.

If more than one possible combination per track exists, the best combined χ^2_{match} is chosen and then the track is removed from the pool of tracks to be matched. The algorithm continues making associations until no more tracks remain.

Finally, tracking, calorimeter and momentum isolation variables are defined in a similar way as with electrons.

MUID algorithm

The MUID reconstruction package [61] implements all muon reconstruction strategies described before. The MUID standalone (SA) algorithm uses tracks and segments reconstructed at the muon spectrometer by the Moore algorithm [72], and extrapolates inwards to obtain track parameters at the vertex. The MuGirl algorithm [73] searches for MS tracks and segments using an ID track as a seed. If the full track refit is successful a combined muon is made, otherwise a tagged muon is made. The MUID family also contains a combined muon algorithm that use a global fit of the tracks reconstructed in the ID and in the MS.

5.2.3 Jet reconstruction

As quarks and gluons hadronize and fragment they produce a large number of soft hadrons and high energy photons. This process results in an object known as a "jet". A jet reconstruction algorithm attempts to recombine all these components to reconstruct the four-momentum vector of the original quark/gluon. The reconstructed jets are the closest physical representation of a hard quark or a gluon available to experimentalists. The development of jet reconstruction algorithms is driven by theoretical and experimental requirements. From a theoretical perspective, it is crucial that jet algorithms be *infra-red and collinear* (IRC) safe. The probability of gluon emission approaches infinity in the collinear and soft regime. These infinities cancel out with virtual gluon emission. If jets resulting from hard particles are merged or split due to soft emission or collinear splitting these probabilities do not cancel and a divergence occurs. A jet algorithm is said to be IRC safe when the reconstructed jets remain unchanged under the addition of a soft emission or a collinear splitting. Jet algorithms should also be able to work given parton, hadron, or calorimeter information. From an experimental perspective, jet algorithms should be stable under increased luminosity or centre of mass energy, be computationally efficient and fast, and work independently of detector technology.

There are many different jet reconstruction algorithms such as the Cambridge/Aachen, k_{T} and SISCone, however only the ATLAS default known as the anti-k_{T} algorithm is used here.

Anti-k_{T} algorithm

The anti-k_{T} algorithm is a clustering algorithm that sequentially combines objects to form cone-shaped jets [74]. This algorithm has been found to be more resilient to the effects of pile-up and underlying event, and the shape of the jet is unaffected by soft radiation producing circular jets. It is also computationally efficient and fast given a smart implementation [75].

The clustering process begins by measuring two distances: the distance between all particles d_{ij}, and the distance between particle i and the beam d_{iB} defined as

$$d_{ij} = \min(k_{\mathrm{T},i}^{-2}, k_{\mathrm{T},j}^{-2}) \frac{\Delta_{ij}^2}{R^2}$$
$$d_{iB} = k_{\mathrm{T},i}^{-2}$$

where $\Delta_{ij}^2 = (y_i - y_j)^2 + (\phi_i - \phi_j)^2$, and $k_{\mathrm{T},i}$, y_i and ϕ_i are the transverse momentum, rapidity, and azimuthal angle of object i. The parameter R defines the characteristic cone size of the jet, note that by construction not all anti-k_{T} jets are conical. For every object both distances are calculated, if d_{ij} is the smallest then objects i and j are combined forming proto-jets, if q_{iB} is smallest the object is labelled as a final jet and removed from the list of objects to be combined. This process continues until all objects are removed.

In general, soft particles will tend to combine with hard objects before combining with other soft objects. If two hard objects lie at $2R$ from each-other, they will both form conical shapes with radius R. Otherwise partially conical jets will form depending on the relative magnitudes of k_{T} of each particle. The standard value of R used for ATLAS analyses is 0.4, this is used here unless stated otherwise.

Jet calibration

The process of jet calibration corrects the jet energy as measured in the detector with the intention of recovering the energy of the original stable particle jet that entered the detector. Clusters of energy deposits in the calorimeter, known as topo-clusters, are constructed from topologically connected calorimeter cells [76]. Calorimeter jets are constructed from topo-clusters that enter the clustering algorithm as massless particles.

These clusters are initially reconstructed at the EM scale, which correctly measures the energy of particles in EM showers. If jet reconstruction is carried on these clusters the jets

are known as EM jets. An additional collection of topo-clusters is created by calibrating the calorimeter cells to correctly reconstruct the response of the calorimeter to hadrons. The main calibration scheme is known as *local cluster weighting* (LCW) [76]. In this scheme each topo-cluster is classified as electromagnetic or hadronic based on shower shape variables, then simulation-derived corrections are applied to each cluster. These correct for the effects of non-compensation, signal losses due to threshold effects, and energy loss in non-instrumented regions of the calorimeter. These corrected topo-clusters are then used in the jet reconstruction algorithms, to build LCW jets.

Additional corrections are applied to topo-clusters at either EM or LCW scale in an attempt to restore the *jet energy scale* (JES) to that of jets reconstructed from simulated stable particles. Additional corrections are applied to compensate for the effects of pile-up, align the jet to point to the primary vertex rather than the ATLAS centre, and other corrections derived from MC simulations. Jets corrected in this way are said to be at the EM+JES scale or LCW+JES scale depending on the scale of the topo-clusters. Each calibration methodology has some uncertainties associated with it, which vary with jet p_{T} and η [77].

5.2.4 b-jet tagging techniques

Identification of heavy flavour (HF) jets, from b- or c-quarks, is very important in the study of many types of events including $t\bar{t}$ events. Identification of b-jets is generally known as b-tagging. Many b-taggers have been developed at ATLAS to achieve the highest efficiency along with strong rejection of LF jets. These algorithms exploit a variety of strategies including impact parameters (IP3D), secondary vertex reconstruction (SV1) and the topology of the b- and c-hadron decays (JetFitter). The output of these variables are used as inputs into multivariate algorithms to provide enhanced b-tagging capabilities. The default algorithm at ATLAS is known as the MV1 tagger is one such algorithm. Finally, *soft lepton tagging* (SLT) exploits the production of leptons within some b-jets to provide separation from LF. The performance of these b-taggers is shown in Figure 5.2. The tagger used in this thesis is an implementation of soft lepton tagging described in more detail below.

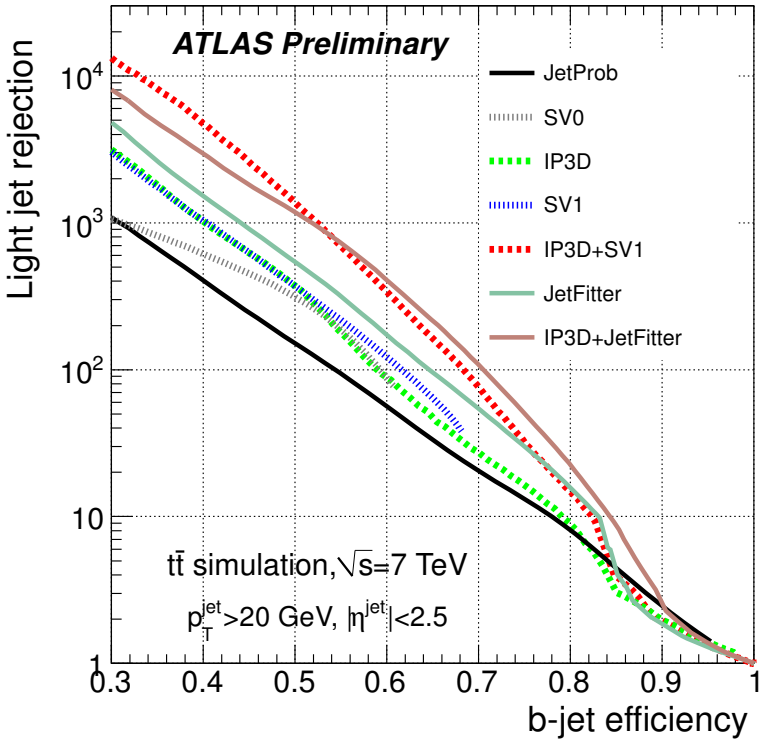

Figure 5.2: Light jet rejection as a function of the b-jet tagging efficiency, comparing some of taggers used at ATLAS as measured in simulated $t\bar{t}$ events [78].

The SV0 and SV1 algorithms

The SV0 algorithm [79] reconstructs secondary vertices using tracks within the cone of the candidate jet. These secondary vertices are located at a decay length L from the primary vertex. A cut is then applied on the decay length significance $L/\sigma_L < 5.72$, this is an operating point that yields a b-tagging efficiency of $50\,\%$ as measured on simulated inclusive $t\bar{t}$ events.

The SV1 algorithm is an extension of the SV0 algorithm. In order to improve the tagging performance, three properties of the secondary vertex are used as inputs to a likelihood ratio: the invariant mass of the tracks associated to the vertex, the ratio of the sum of the energies of the tracks in the vertex to the sum of the energies of the tracks in the jet, and the number of two-track vertices. The ΔR between the jet axis and the line joining the primary and secondary vertices is also used.

The JetFitter algorithm

The JetFitter algorithm [78] uses a Kalman filter to find a line along which the b quark, c quark, and the primary vertices lie along with their position on the line, giving an approximated flight-path for the B-hadron. Discrimination is based on a likelihood using similar variables as in the SV1 algorithm and variables such as the flight length significances of the secondary vertices.

The IP3D algorithm

The IP3D algorithm makes use of the transverse and longitudinal impact parameter significances in two-dimensional histograms to discriminate between b, c and LF jets. A likelihood-ratio method is used: the IP significances are compared to pre-defined smoothed and normalized distributions for b- and light-jets hypotheses. This produces a weight distribution for each model and a cut is applied to select jets. The IP3D algorithm is often combined with the JetFitter (IP3D+JetFitter) or SV1 algorithm (IP3D+SV1) to provide additional discriminating power.

The MV1 algorithm

The MV1 algorithm uses the output weights of the IP3D, SV1 and JetFitter algorithms as inputs to an artificial neural network. The working point used at ATLAS is defined so as to achieve a b-tagging efficiency of 70 % with an associated mistag rate of less than $1.5\,\%$ [80] depending on

the pseudorapidity and transverse momentum of the jet in question. Note that this efficiency is not constant with respect to the jet p_{T} as can be seen from Figure 5.3. The performance at low p_{T} degrades as the decay length is shorter so finding the secondary vertex is more difficult.

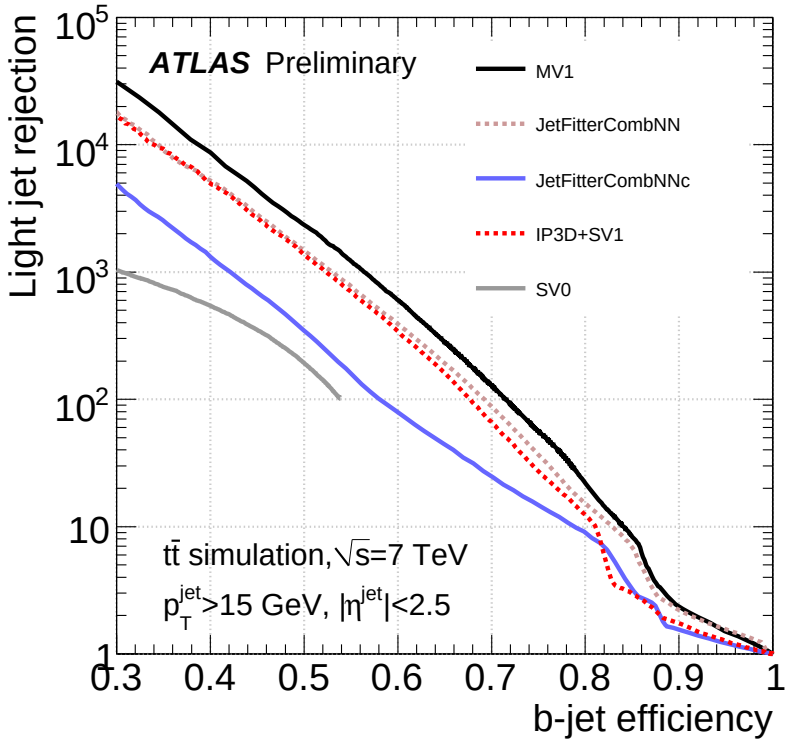

Figure 5.3: The light jet rejection factor as a function of b-tagging efficiency as measured in simulated $t\bar{t}$ events for the MV1, SV0, IP3D+SV1, and the JetFitterCombNN taggers [81].

Soft lepton tagging

Soft lepton tagging (SLT) algorithms attempt to identify leptons produced in the semileptonic decay of b and c quarks for the purpose of determining the presence of HF quarks. The term "semileptonic" here refers to the decay of a B-hadron in such a way as to produce a lepton-neutrino pair with an additional hadron. The lepton produced is known as a *soft* lepton due to its relatively low transverse momentum.

A soft muon can be produced in a variety of ways starting from a b-quark, either directly via $b \to \mu\bar{\nu}_{\mu}X$, where X is any hadron; or indirectly, via a c, $\bar{c}$ or a τ lepton. The direct and indirect via a c production mechanisms are shown in Figure 5.4. The branching ratio for each

of these decays is shown in Table 5.1. The total BR for the production of a soft muon from a b quark is $20.1 \pm 1.0\,\%$, thus the probability for a $t\bar{t}$ event to contain at least one semileptonic b decay is approximately $36\,\%$.

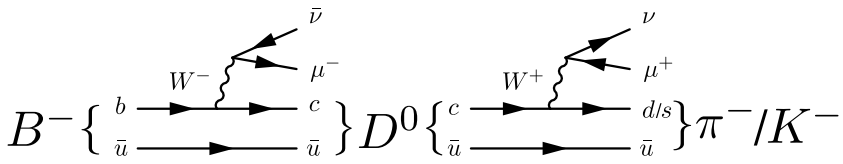

Figure 5.4: Feynman diagram of one of the mechanisms for lepton production via semileptonic b decay. Shown are the direct $b \to \mu$ and indirect $b \to c \to \mu$.

Mode	Muon BR [%]
$b \to \mu^-$	$10.95\ ^{+\,0.29}_{-\,0.25}$
$b \to c \to \mu^+$	8.02 ± 0.19
$b \to \bar{c} \to \mu^-$	1.6 ± 0.5
$b \to \tau^- \to \mu^-$	0.42 ± 0.04
All modes	21.0 ± 1.0

Table 5.1: Branching ratio for the production of a muon from a b-quark in both direct and indirect modes [19].

The soft muon tagger used in this analysis is based on the quality of the fit between the ID track and MS track as represented by the χ^2_{match}. Several tagger-specific cuts (summarized in Table 5.2) are placed on the candidate muons and jets. Candidate SMT muons are required to lie within the coverage of the ID and have sufficient transverse momentum for reliable reconstruction. Requirements are made on the impact parameters of the muon ID track to remove contributions from spurious matches between ID and MS tracks, and from pile-up vertices. Finally, the main cut on the quality of the fit $\chi^2_{\text{DoF}} = \chi^2_{\text{match}}/N_{\text{DoF}}$ is set at less than 3.2. This is an operating-point that provides a b-jet (semileptonic b-jet) identification efficiency of $10\,\%$ ($50\,\%$) and a LF rejection factor of 200 per jet. Candidate jets are required to have more than three charged tracks associated with them or a jet EM fraction smaller than 0.8. These criteria ensure that the jet did not originate from the muon itself. Finally, the muon is associated to the jet with a cut $\Delta R^{\text{jet}}_{\mu} < 0.5$. The following chapter describes the calibration of the SMT tagger.

Muon cuts	
Muon to jet association	$\Delta R_{\mu}^{\text{jet}} < 0.5$
Reconstruction	$\lvert\eta\rvert < 2.5$
	$p_{\text{T}} > 4\,\text{GeV}$
Pile-up reduction	$\lvert d_0\rvert < 3\,\text{mm}$
	$\lvert z_0 \sin\theta\rvert < 3\,\text{mm}$
Track matching quality	$\chi^2_{\text{DoF}} < 3.2$
Muon-jet rejection	Jet $N_{\text{trk}}^{\text{charged}} > 3$ **or**
	Jet EM fraction < 0.8

Table 5.2: Jet and muon SMT Cuts.

5.2.5 Missing energy reconstruction

Missing energy is reconstructed by combining information from energy depositions in the calorimeter, as well as information from the muon spectrometer [82]. An energy imbalance in the detector is then treated as missing energy. The two components of the vector $\boldsymbol{E}_{\text{T}}^{\text{miss}}$ are calculated thus:

$$E_{x(y)}^{\text{miss}} = E_{x(y)}^{\text{miss,calo}} + E_{x(y)}^{\text{miss},\mu} \tag{5.4}$$

ID tracking information is used to recover low-p_{T} that are missed in the calorimeters, and for muons in regions not covered by the MS. The magnitude of the missing energy $E_{\text{T}}^{\text{miss}}$, which is normally used in event selections, are calculated as:

$$E_{\text{T}}^{\text{miss}} = \sqrt{(E_x^{\text{miss}})^2 + (E_y^{\text{miss}})^2} \tag{5.5}$$

The calorimeter term is constructed by associating calorimeter cells with reconstructed and identified high-p_{T} objects in order: electrons, photons, hadronically decaying τ-leptons, jets, and muons. Calorimeter cells not associated are also included in the summation as $E_{x(y)}^{\text{miss,CellOut}}$. Thus each components of the calorimeter term of the missing energy are the linear sum of each contribution:

$$E_{x(y)}^{\text{miss,calo}} = E_{x(y)}^{\text{miss},e} + E_{x(y)}^{\text{miss},\gamma} + E_{x(y)}^{\text{miss},\tau} + E_{x(y)}^{\text{miss,jets}} + E_{x(y)}^{\text{miss,softjets}} + E_{x(y)}^{\text{miss,CellOut}} + (E_{x(y)}^{\text{miss},\mu}) \tag{5.6}$$

where the muon term is not always added [82].

Each component is calculated as the negative sum of calibrated cell energies for each corresponding object, as:

$$E_x^{\text{miss,term}} = -\sum_{i=1}^{N_{\text{cell}}^{\text{term}}} E_i \sin\theta_i \cos\phi_i \tag{5.7}$$

$$E_y^{\text{miss,term}} = -\sum_{i=1}^{N_{\text{cell}}^{\text{term}}} E_i \cos\theta_i \sin\phi_i \tag{5.8}$$

where E_i, θ_i, and ϕ_i are the energy and angular position of the cell.

The muon term of the missing transverse energy is calculated as the negative sum of the momenta of muon tracks reconstructed in $|\eta| < 2.7$:

$$E_{x(y)}^{\text{miss},\mu} = -\sum_{\text{muons}} p_{x(y)}^{\mu} \tag{5.9}$$

For muons in the region covered by the ID, only combined muons are considered to remove contributions from fake muon sources such as energetic hadrons that "punch through" the calorimeter. In this region, muons which are well separated from jets, $\Delta R > 0.3$, are treated separately from muons which are non-isolated:

- **Isolated muons:** The combined track p_{T} corrected for energy losses in the calorimeter is used the summation. The muon calorimeter energy term is not included to avoid double-counting.
- **Non-isolated muons:** The muon momentum as measured in the spectrometer after energy loss is used. The muon term $E_{x(y)}^{\text{miss},\mu}$ is then added to the calorimeter term in Equation 5.6.

Outside of the coverage of the ID ($2.5 < |\eta| < 2.7$) there is no combined track requirement and the p_{T} as measured in the MS is used for both isolated and non-isolated muons. For more information on the measurement and calibration of $E_{\text{T}}^{\text{miss}}$ at ATLAS see [82].

Chapter 6

Calibration of the soft muon tagger for 2012 ATLAS data

High-energy physics relies heavily on the use of simulated data to inform the development of analysis techniques. It is paramount that the simulation describe nature as closely as possible. However, the simulation cannot perfectly recreate conditions within the detector and some kinematic variables are not accurately simulated. This includes the quality of matching between ID and MS tracks which are fundamental for the SMT tagger.

Selection and reconstruction techniques are said to be calibrated when the discrepancy between simulation and collision data is quantified. This process has to be repeated on new collision data and/or when simulation is changed in a relevant and significant way.

The difference in efficiency between collision data and simulation of the muon reconstruction procedure and the χ^2_{match} tagger selection are accounted for by a scale factor (SF),

$$\text{SF} = \frac{\epsilon^{\text{Data}}}{\epsilon^{\text{MC}}} \tag{6.1}$$

which is used to rescale the simulation so that it matches the data more closely.

One of the advantages of using the χ^2_{match} tagger over other forms of b-tagging is that the presence of a jet is not required to measure the χ^2_{match} of a muon. This means that the calibration can be performed on isolated muons such as those from $J/\psi \to \mu\mu$ or $Z \to \mu\mu$ using the so called tag and probe method. This calibration relies on muons with low p_{T} from J/ψ decays. Within ATLAS, the nominal calibration of the reconstruction efficiency is performed

on $Z \to \mu\mu$ due to the smaller uncertainty using high p_{T} muons. The SF at low p_{T} are obtained by extrapolating back into the low momentum range.

The tag and probe method is implemented as follows: a STACO combined muon is designated as the *tag*, this muon must pass a stringent set of cuts implying that it is indeed a muon from a J/ψ. The second muon, which is designated as the *probe*, is simply an ID track. To ensure that the probe is the second muon from the J/ψ decay, the invariant mass of the combined tag and probe system is required to be in a window centred around the J/ψ mass. The complete selection used in the calibration is detailed in Section 6.1. These probes are used to measure the reconstruction efficiency and the χ^2_{match} tagger efficiency by using a fit to their invariant mass distribution as described in Section 6.2. This procedure is performed in various bins of kinematic variables such as transverse momentum and angular position. The binning is described in more detail in Section 6.3.2. The results of this analysis are then presented in Section 6.3.

The procedure used here is based on a previous calibration of the χ^2_{match} tagger performed on 2011 ATLAS collision data detailed in [83]. It differs from the 2011 calibration in several ways which will be highlighted and explained.

Software, collision data and simulated samples

The dataset used is made of those luminosity blocks selected by the recommended standard *good runs list* (GRL) which corresponds to all pp collision periods in 2012. The GRL selects only those luminosity blocks where detector conditions are appropriate for physics data-taking. This requires that all relevant detector components are operational, and that stable beam conditions have been achieved. In total this represents an integrated luminosity of $20.1\,\mathrm{fb}^{-1}$.

The efficiency scale factor is measured against a sample containing almost 10 million $J/\psi \to \mu\mu$ events. At event generation, filters are applied so the sample only contains events where both truth muons have a momentum of at least $4\,\mathrm{GeV}$ and they must lie within the pseudorapidity range $|\eta| < 2.5$. This selection matches the object selection used by most analyses.

6.1 Tag and probe selection

The tag and probe procedure is as follows: first, require the presence of a STACO CB muon which passes a very stringent selection. This strongly implies that this is a real muon and thus is labelled as the tag. A very loose selection is then applied to all ID tracks to construct a pool of candidate probes. Pairs of tag and probes are formed by requiring that the combined invariant mass lie within a J/ψ mass window and the pair pass additional pairing cuts. This then implies that the probe is likely the other muon from the J/ψ decay and as such is a suitable test-bed to measure the performance of the muon reconstruction algorithm. All selection criteria are detailed and explained in Section 6.1.2.

Probes which are reconstructed into STACO CB muons are labelled as muon probes. The reconstruction performance is quantified by the portion of probes, which are likely to be real muons, that are reconstructed into muons. The performance of the χ^2_{match} tagger is estimated in a similar way, by measuring the proportion of muon probes which are selected by the χ^2_{match} algorithm.

6.1.1 Trigger requirements

In order for an event to be included in the analysis it must have fired at least one of the trigger chains listed in Appendix D. Only the primary trigger, EF_mu6_Trk_Jpsi_loose which contributes the majority of events, is described here.

As stated in the trigger name, this is an EF trigger which requires the presence of a muon with a momentum of at least 6 GeV and an ID track with a combined invariant mass in the range $2.6\,\text{GeV} < m_{\text{inv}} < 3.6\,\text{GeV}$. This mass window is loose enough to contain the entirety of the J/ψ peak and side-bands that allow for background removal. Double muon triggers are not used to avoid introducing a bias by requiring the presence of two good muons.

While all triggers are operational in all periods, most are heavily prescaled by a factor which is period dependent. This does not have a first-order effect on the efficiency as only ratios of event yields are compared between collision data and simulation. However, the effective integrated luminosity is reduced to approximately $200\,\text{nb}^{-1}$ as a result of the prescale. A short study was carried out to examine the effects of multiple prescaled triggers on the scale factors. The measurement was carried out using only the primary trigger and the results were

Tag selection	
Reconstruction cuts	STACO combined muon
	$\lvert\eta\rvert < 2.5$
	$p_{\mathrm{T}} > 4\,\mathrm{GeV}$
Pileup reduction	$\lvert d_0\rvert < 0.3\,\mathrm{mm}$
	$\lvert z_0\rvert < 1.5\,\mathrm{mm}$
	$\lvert d_0/\sigma_{d_0}\rvert < 3$
	$\lvert z_0/\sigma_{z_0}\rvert < 3$

Table 6.1: Tag selection criteria.

compared to the nominal calibration which included all the triggers, no significant discrepancy between the two was observed.

6.1.2 Selection cuts

The selection criteria for tags, probes, muon probes and SMT muons are listed and detailed below. All cuts are applied on the kinematic properties as measured in the ID due to its better resolution. Also note that all objects must pass a set of track quality criteria as recommended by the ATLAS *muon combined performance* (MCP) group. These cuts require a certain number of detector elements be active to ensure good quality track reconstruction. The selection criteria are listed in Appendix E.

The tag selection is summarized in Table 6.1. The tag is a STACO combined muon with a pseudorapdity and transverse momentum that allow for reliable reconstruction. The requirements on the impact parameter variables are in place to remove spurious muons from pile-up events and the decay-in-flight of long-lived hadrons. Finally, the tag muon is required to have fired at least one of the triggers under which the event was recorded. This is done by matching the reconstructed trigger object to the tag muon via a ΔR cut of less than 0.01.

The probe selection is a subset of the tag selection and only requires an ID track with $|\eta| < 2.5$ and $p_{\mathrm{T}} > 4\,\mathrm{GeV}$.

The pairing selection, summarized in Table 6.2, is designed to construct pairs of tag and probe candidates which likely come from the same J/ψ decay. The main component of the selection is the invariant mass window cut. The tag and the probe are required to be well

separated in η-ϕ space to prevent the objects from entering each others isolation cones.

Pairing criteria	
Opposite charge	$q_{\text{tag}} \neq q_{\text{probe}}$
Mass window	$\lvert m_{J/\psi} - m_{\text{tag, probe}}\rvert \leq 2\,\text{GeV}$
Overlap reduction	$0.2 < \Delta R^{\text{tag}}_{\text{probe}} < 3.5$
Pileup reduction	$\Delta z_0 < 0.2\,\text{mm}$

Table 6.2: Pairing criteria.

In the 2011 calibration analysis, the track of the tag and the probe were refitted to a common vertex and the quality of the refit, expressed by a χ^2, was part of the pairing criteria. This cut is meant to reduce the effects of pile-up on the measurement by ensuring both objects have a common origin. Due to operational reasons it is not possible to perform the refitting in this case. Instead, a cut on $\Delta z_0 = \lvert z_{0,\text{ tag}} - z_{0,\text{ probe}}\rvert$ is applied. If several pairings are made for a single tag, the pair with the smallest Δz_0 is used.

The STACO CB reconstruction efficiency is not measured by applying the algorithm on the probe collection but rather a probe is said to be a muon probe if it matches a combined muon from the STACO collection. This is done by requiring the ΔR between the probe and the STACO CB muon be less than 0.01. Probes which are matched become the numerator of the reconstruction efficiency and the denominator is defined as the number of probes:

$$\epsilon_{\text{reco}} = \frac{N_{\text{muon probe}}}{N_{\text{probe}}} \tag{6.2}$$

A muon probe is said to be an SMT muon if it passes the selection listed in Table 6.3 that matches the cuts defined in Section 5.2.4. The χ^2_{DoF} distribution of muon probes is shown in Figure 6.1.

SMT selection	
Pileup reduction	$\lvert d_0\rvert < 3\,\text{mm}$
	$\lvert z_0 \sin(\theta)\rvert < 3\,\text{mm}$
Match quality	$\chi^2_{\text{match}}/N_{\text{DoF}} < 3.2$

Table 6.3: SMT criteria.

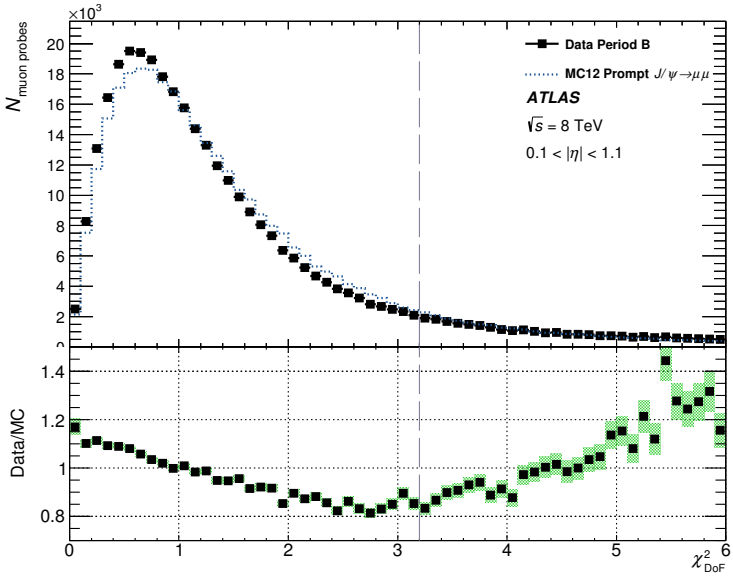

Figure 6.1: The distribution of χ^2_{DoF} for all muon probes for ATLAS collision data (solid dots) and simulated prompt J/ψ (dotted line). Note that the collision data distribution includes sources of background.

The denominator of the SMT efficiency is the number of muon probes and the numerator is the number of muon probes which pass the SMT selection:

$$\epsilon_{\text{SMT}} = \frac{N_{\text{SMT}}}{N_{\text{muon probe}}} \tag{6.3}$$

6.2 Invariant mass fitting

The pairing criteria are very effective at selecting J/ψ events, however non-J/ψ background events also pass the selection. These include combinatorial background where the wrong tag and probe pair is constructed, and Drell-Yan which appears as a continuum below the J/ψ peak.

The number of probes is extracted from a fit to the invariant mass of the dimuon system. The invariant mass is fitted with the sum of a quadratic polynomial, for the background; and a Gaussian function, for the signal. The yield is obtained by subtracting the integral of the background function from the binned data, this is used instead of relying on an accurate fit to the signal peak.

The integration is performed in a window with a width three times larger than the width of the fitted Gaussian, denoted as 3σ in Figure 6.2. The composite fit line, the background-only distribution and the implied signal Gaussian peak are also shown.

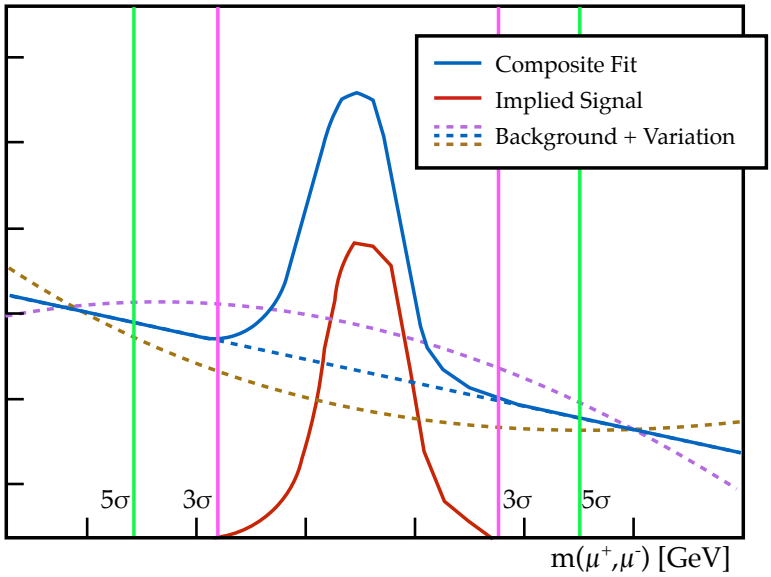

Figure 6.2: Drawing of the components of the fitting procedure. The composite fit is shown along with the corresponding implied signal and background. The two variations of the background shape are also shown, these are exaggerated for illustration purposes.

The J/ψ peak does not follow a Gaussian shape exactly, but rather the best fit is obtained by the so-called Crystal Ball function shown in Figure 6.3. This is a convolution of a Gaussian function with a power tail at low invariant mass to account for the energy loss due to photon emission.

Different combinations of signal and background functions were tested to determine the most stable combination. For the signal, the sum of two Gaussian functions was tested, while for the background a linear function, an exponential function, and the sum of two exponential functions were tried. It was found that none of these yielded good stable fits in the entire pseudorapidity range. For example, the linear function resulted in a mismodelling of the background at the probe level which led to negative efficiencies or extremely large uncertainties.

From an operational perspective, using a Gaussian function allowed for good stable fits over the hundreds of bins used, and simplified the fitting procedure as a whole. Any mismodelling of the background because of the choice of a Gaussian in lieu of the Crystal Ball fit, is

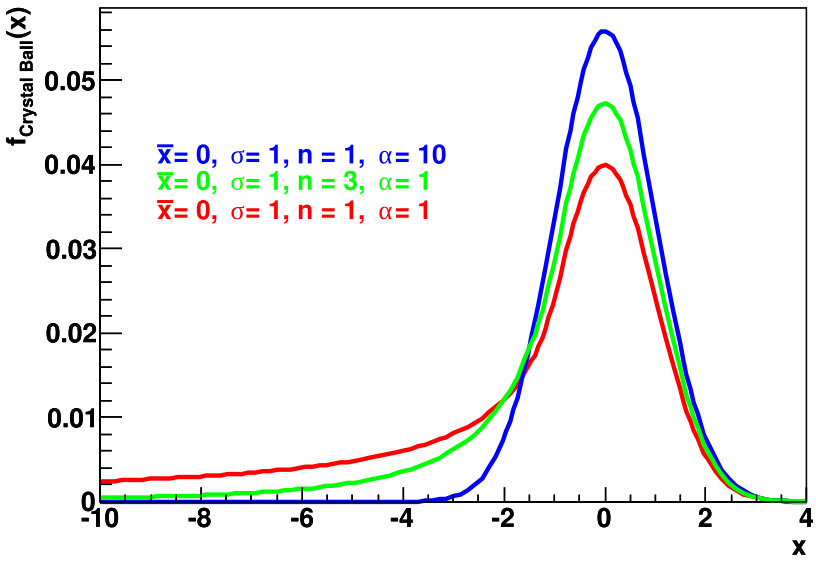

Figure 6.3: Diagram of crystal ball distributions with varying tail sizes [84]. The parameters $\bar{x}$ and σ are the mean and width of the Gaussian, while α and n respectively determine the start and shape of the power-tail.

taken into account by the background uncertainty described in the next section.

Several different sets of initial fit conditions were tested and those which yielded the best and most stable fits across the entire η and p_{T} range were used.

The width at the probe level is obtained from the fit and is then used in the fits to the muon probe and SMT distributions. The mean is obtained independently from the fit to each individual distributions. The mean is expected to lie very close to the true J/ψ mass, however this is not forced in the fitting procedure. Instead the fit is allowed to set the mean in a window with a width of approximately $1.2\,\mathrm{GeV}$.

6.2.1 Uncertainty measurement

The uncertainty on the efficiency is made up of three components: the statistical uncertainty on the efficiency is estimated as a binomial error,

$$\sigma_{\text{stat.}} = \sqrt{\frac{\epsilon(1-\epsilon)}{N}} \tag{6.4}$$

where ϵ is the measured efficiency and N is, in this case the denominator of the efficiency measured.

The second component of the efficiency uncertainty quantifies the error in the background fit. The uncertainty is determined by constructing two functions that denote the maximum upward and downward fluctuation of the background fit. The efficiency is measured using one of these fluctuations and the result is compared to the nominal efficiency.

After the fit of the composite function is carried out, a downward variation of the background is defined as:

$$f^{\text{down}}(x) = a_{\text{min}}x^2 + b_{\text{max}}x + c_{\text{min}} \tag{6.5}$$

where the maximum and minimum the parameters ($X_{\text{min / max}}$) are obtained by varying the central value by the uncertainty obtained from the fit, $X_{\text{max / min}} = X_{\text{central}} \pm \sigma_X$

The upward variation of the background fit is defined as the opposite:

$$f^{\text{up}}(x) = a_{\text{max}}x^2 + b_{\text{min}}x + c_{\text{max}} \tag{6.6}$$

These background variations result in the maximum deviation from the nominal integral (Figure 6.2). The uncertainty on the efficiency is determined by obtaining the maximum efficiency in both directions. If the nominal efficiency is defined as

$$\epsilon_{\text{nominal}} = \frac{N^{\text{nominal}}_{\text{numerator}}}{N^{\text{nominal}}_{\text{denominator}}} \tag{6.7}$$

then the variations are defined as,

$$\epsilon_{\text{up}} = \frac{N^{\text{up}}_{\text{numerator}}}{N^{\text{down}}_{\text{denominator}}}, \qquad \epsilon_{\text{down}} = \frac{N^{\text{down}}_{\text{numerator}}}{N^{\text{up}}_{\text{denominator}}} \tag{6.8}$$

where $N^{\text{up/down}}$ are the yields obtained from the integration of the upward/downward variations of the background function.

Finally the uncertainty on the background is given by the average of the differences between ϵ_{up} and ϵ_{down}, and the nominal efficiency:

$$\sigma_{\text{bkg}} = \frac{1}{2}(|\epsilon_{\text{up}} - \epsilon_{\text{nominal}}| + |\epsilon_{\text{down}} - \epsilon_{\text{nominal}}|) \tag{6.9}$$

The final component of the uncertainty is obtained by varying the integration window. The nominal value is defined as $3\sigma_{\text{gaus}}$ away from the centre of the fitted Gaussian. An uncertainty

is constructed by measuring the efficiency with a wide integration window corresponding to 5σ. The integration window uncertainty is defined as:

$$\sigma_{\text{sig.}} = |\epsilon_{5\sigma} - \epsilon_{3\sigma}| \tag{6.10}$$

The total uncertainty on the efficiency is given by the sum in quadrature of all the uncertainty components. The uncertainty on the efficiency is then carried over to the scale factor determination. As expected the invariant mass distribution for all probes contains a large amount of background, particularly in data (Figure 6.4). The "shoulders" at each side of the J/ψ peak are the result of the main J/ψ trigger which includes a mass window cut more stringent than that required by the pairing selection. Requiring that the probe match a STACO CB muon greatly reduces the amount of background. Applying the SMT requirements also reduces the background though not as substantially.

6.3 Efficiencies

The efficiency is monitored as a function of a variety of kinematic variables, including the isolation, transverse momentum, azimuthal angle, and the pseudorapidity of the probe.

6.3.1 The 2011 calibration

The selection and fitting procedure used for this calibration are based on the 2011 analysis [83]. In that calibration, the efficiencies measured exhibited no dependence on ϕ, an asymmetric dependence on η particularly in the forward regions of the detector, and a dependence on p_{T}. The scale factors were close to unity within their uncertainty across the entire η and p_{T} range examined as shown in Table 6.4.

6.3.2 Efficiency binning

The binning in most variables is governed by the amount of data required to produce stable, good quality fits. The binning in pseudorapidity, summarized in Table 6.5, corresponds with different regions of the ATLAS detector and differentiates between the positive and negative sides. The chosen p_{T} binning is shown in Table 6.6.

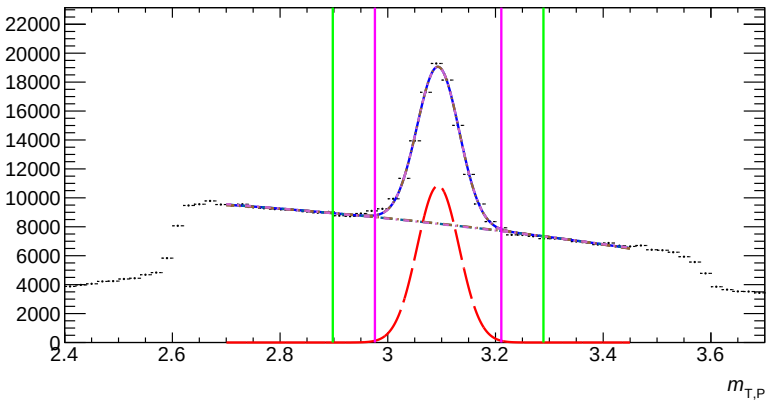

(a) Probe level

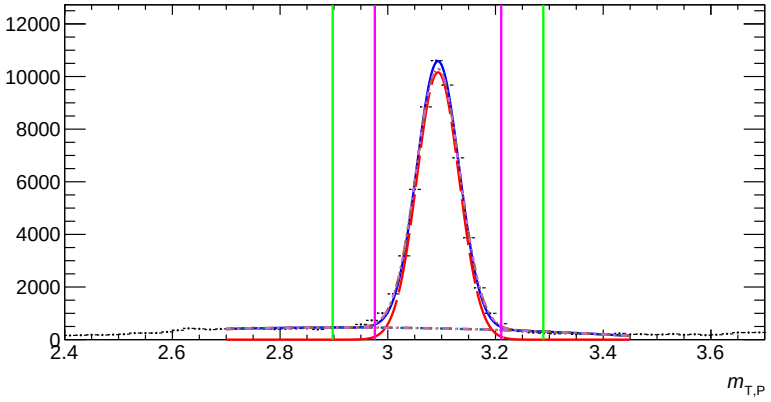

(b) Muon probe level

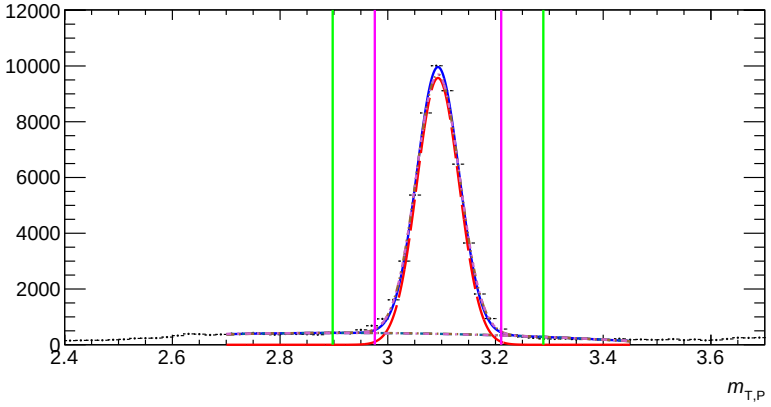

(c) SMT probe level

Figure 6.4: Invariant mass distributions of tag and probe pairs at (a) probe level, (b) muon probe level, and (c) SMT level in collision data for probes in barrel A with a p_T of 5 to 6 GeV. Shown are all the components of the fit including: composite nominal fit (solid curve), nominal background (dashed curve), background variations (dashed-dot curves), implied J/ψ peak (long dashed red curve), the 3σ and 5σ integration windows used for systematics (vertical lines).

p_{T} range [GeV]	Scale Factor in				
Side A	Crack	Barrel	Transition	End-cap	Forward
4–5	0.974 ± 0.009	0.981 ± 0.003	0.987 ± 0.007	0.981 ± 0.003	0.991 ± 0.005
5–6	0.996 ± 0.008	0.983 ± 0.003	0.987 ± 0.008	0.988 ± 0.004	0.980 ± 0.006
6–7	0.990 ± 0.009	0.984 ± 0.003	0.960 ± 0.010	0.984 ± 0.005	0.981 ± 0.006
7–8	0.966 ± 0.013	0.987 ± 0.004	0.978 ± 0.008	0.990 ± 0.006	0.982 ± 0.007
8–10	0.983 ± 0.011	0.981 ± 0.003	1.005 ± 0.009	0.988 ± 0.005	0.954 ± 0.008
10–12	0.928 ± 0.019	0.979 ± 0.004	1.002 ± 0.009	0.991 ± 0.006	0.984 ± 0.011
Side C	Crack	Barrel	Transition	End-cap	Forward
4–5	0.984 ± 0.008	0.978 ± 0.003	0.992 ± 0.007	0.979 ± 0.003	1.005 ± 0.006
5–6	0.992 ± 0.007	0.991 ± 0.002	0.982 ± 0.009	0.986 ± 0.004	1.012 ± 0.007
6–7	0.989 ± 0.008	0.981 ± 0.003	0.980 ± 0.008	0.990 ± 0.005	1.003 ± 0.010
7–8	0.931 ± 0.017	0.983 ± 0.003	0.970 ± 0.053	0.985 ± 0.006	1.047 ± 0.010
8–10	0.981 ± 0.017	0.987 ± 0.003	0.968 ± 0.009	0.990 ± 0.005	1.100 ± 0.008
10–12	0.974 ± 0.015	0.976 ± 0.004	0.970 ± 0.011	1.002 ± 0.006	1.083 ± 0.010

Table 6.4: Data/MC Scale Factors for 2011 Data in all five regions of the detector as a function of p_{T}. The uncertainties include systematic and statistical components as described in [83].

Name	$\lvert\eta\rvert$ range
Crack	0.0–0.1
Barrel	0.1–1.1
Transition	1.1–1.3
End-cap	1.3–2.0
Forward	2.0–2.5

Table 6.5: Pseudorapidity regions of the ATLAS detector.

6.4 Results

The reconstruction and χ^2_{match} tagging efficiencies are presented in the following pages as a function of η, ϕ and p_{T}. The STACO CB reconstruction efficiencies and scale factors as measured in side A and C of the detector are shown in Figure 6.5 and Figure 6.6 respectively. The efficiencies exhibit a strong dependence on transverse momentum and pseudorapidity.

The reconstruction efficiency for muons in the crack region appears to suffer from low data particularly in the high-p_{T} range, this is expected due to the MS being only partially equipped in the region around $\eta = 0$. In the transition region the MS coverage in ϕ is not uniform due to some chambers not being installed.

The χ^2_{match} tagging efficiency exhibits an asymmetric dependence on the muon probe pseudorapidity, but no dependence on the azimuthal angle ϕ (Figure 6.7). As expected, there is a strong dependence on the transverse momentum of the muon probe (Figure 6.8). As in the 2011 analysis it was decided to bin the SF as a function of p_{T} and η, distinguishing between side A and C of the detector. The scale factor and efficiency distributions are presented in the next pages for the crack region (Figure 6.9), the barrel region (Figure 6.10), the transition region (Figure 6.11), the endcap region (Figure 6.12), and the forward region (Figure 6.13).

The SMT scale factors and their total uncertainties are summarized in Table 6.6. As an example of the typical uncertainties obtained, the SMT efficiencies measured for muon probes with p_{T} in the range 5–6 GeV in the positive barrel region are

$$\epsilon_{\text{Data}} = (94.15 \pm 0.32\,(\text{bkg.}) \pm 0.02\,(\text{sig.}) \pm 0.10\,(\text{stat.}))\%$$
$$\epsilon_{\text{MC}} = (89.01 \pm 0.01\,(\text{bkg.}) \pm 0.01\,(\text{sig.}) \pm 0.07\,(\text{stat.}))\%$$

As expected, the background uncertainty dominates in collision data while in simulation it represents the smallest source of uncertainty. The width of the J/ψ peak increases for forward probes, overwhelming the background distribution delimited by the trigger "shoulders". This is reflected in increased fit parameter uncertainties and a larger background uncertainty.

Isolation dependence

The muons from the J/ψs used in this calibration are produced in isolation, meaning there is very little energetic activity surrounding them in the detector. In contrast, muons from

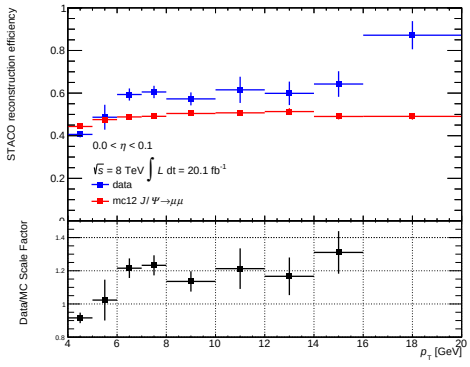

(a) Crack A.

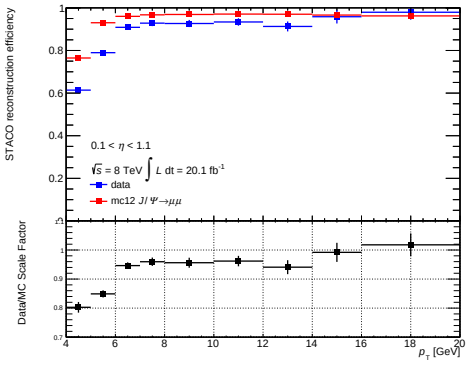

(b) Barrel A.

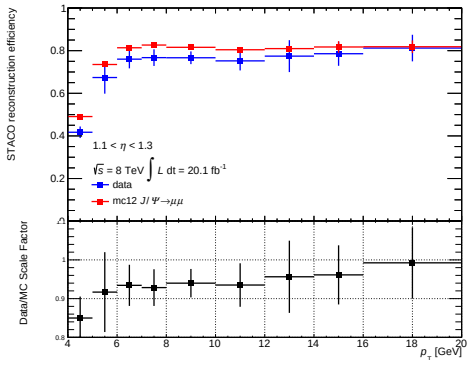

(c) Transition A.

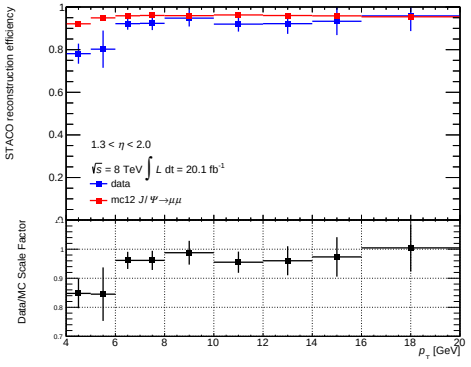

(d) End-cap A.

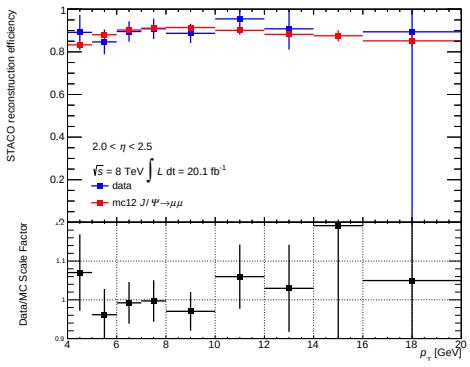

(e) Forward A.

Figure 6.5: Distribution of the STACO CB reconstruction efficiency as measured in data and MC, and the associated scale factor as a function of the probe p_{T} measured in side A for all detector regions.

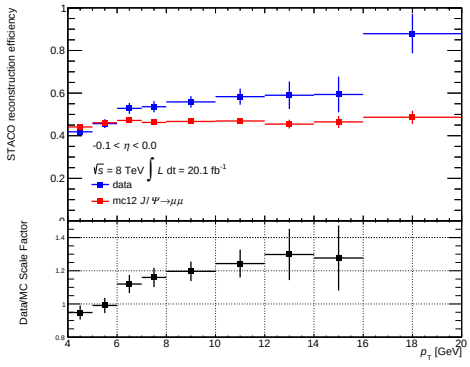

(a) Crack C.

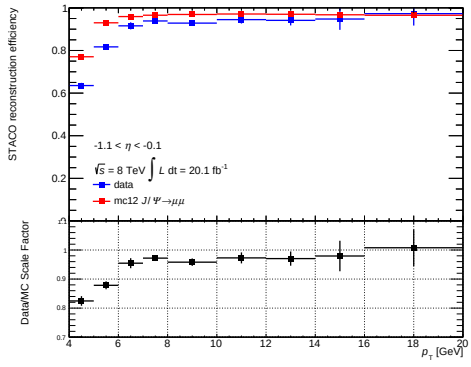

(b) Barrel C.

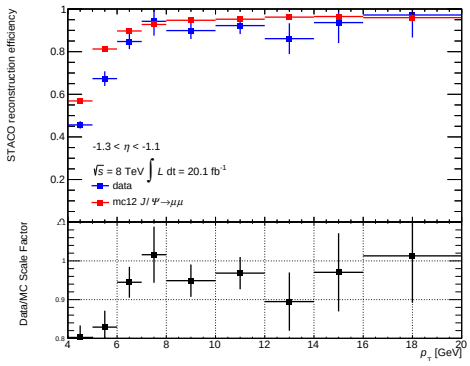

(c) Transition C.

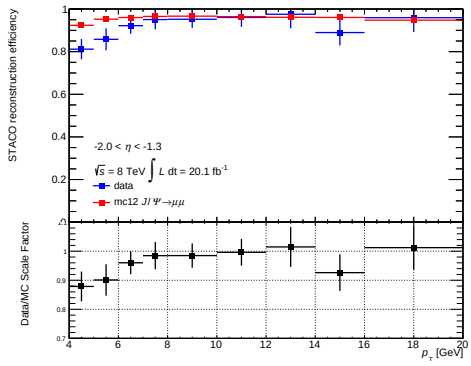

(d) End-cap C.

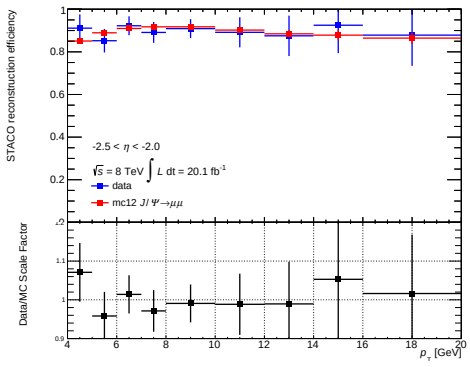

(e) Forward C.

Figure 6.6: Distribution of the STACO CB reconstruction efficiency as measured in data and MC, and the associated scale factor as a function of the probe p_{T} measured in side C for all detector regions.

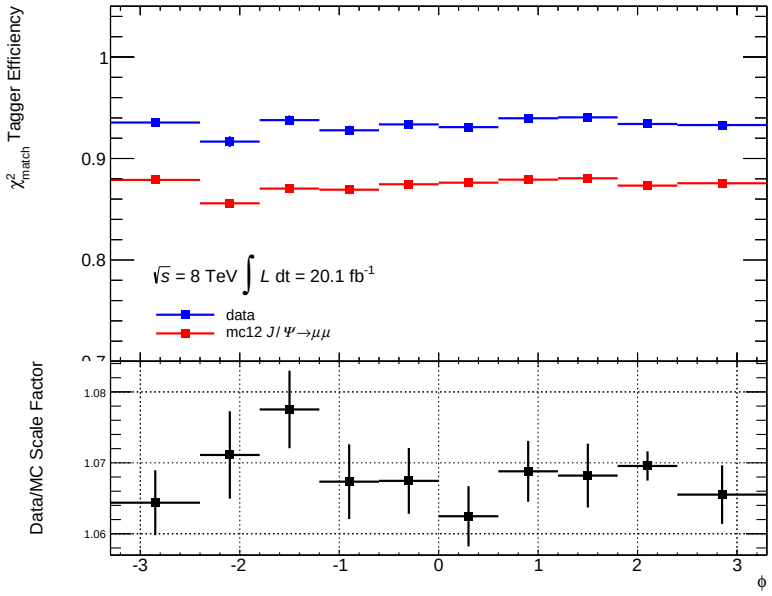

(a) χ^2_{match} efficiency and scale factor as a function of the azimuthal angle ϕ of the probe muon.

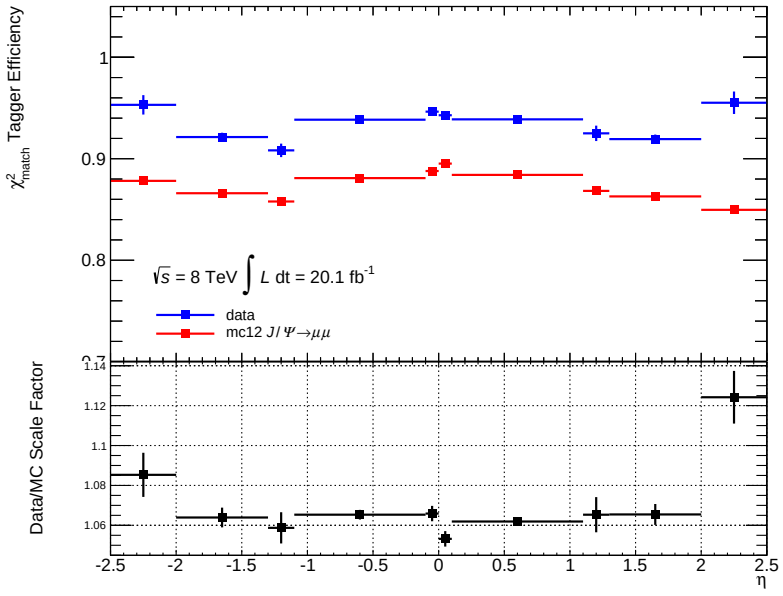

(b) χ^2_{match} efficiency and scale factor as a function of the pseudorapidity η of the probe muon.

Figure 6.7: Distribution of the χ^2_{match} efficiency as measured in data and MC, and the associated scale factor with respect to the (a) azimuthal angle ϕ and (b) the pseudorapidity η of the muon probe.

p_{T} range [GeV]	Scale Factor in				
Side A	Crack	Barrel	Transition	End-cap	Forward
4–5	1.051 ± 0.014	1.053 ± 0.001	1.045 ± 0.005	1.059 ± 0.002	1.088 ± 0.002
5–6	1.051 ± 0.005	1.058 ± 0.001	1.057 ± 0.005	1.062 ± 0.010	1.106 ± 0.003
6–7	1.068 ± 0.006	1.066 ± 0.001	1.069 ± 0.004	1.066 ± 0.002	1.132 ± 0.003
7–8	1.061 ± 0.006	1.063 ± 0.001	1.065 ± 0.004	1.062 ± 0.002	1.142 ± 0.003
8–10	1.061 ± 0.016	1.063 ± 0.001	1.068 ± 0.004	1.063 ± 0.002	1.161 ± 0.003
10–12	1.057 ± 0.024	1.071 ± 0.006	1.062 ± 0.007	1.060 ± 0.015	1.171 ± 0.006
12–14	1.059 ± 0.016	1.062 ± 0.003	1.070 ± 0.010	1.057 ± 0.020	1.178 ± 0.012
14–16	1.043 ± 0.068	1.069 ± 0.013	1.076 ± 0.043	1.069 ± 0.006	1.204 ± 0.013
16–20	1.027 ± 0.077	1.077 ± 0.006	1.112 ± 0.019	1.067 ± 0.004	1.208 ± 0.009
Side C	Crack	Barrel	Transition	End-cap	Forward
4–5	1.044 ± 0.014	1.055 ± 0.001	1.053 ± 0.004	1.056 ± 0.002	1.064 ± 0.005
5–6	1.069 ± 0.005	1.057 ± 0.001	1.050 ± 0.015	1.061 ± 0.008	1.083 ± 0.003
6–7	1.080 ± 0.005	1.068 ± 0.004	1.065 ± 0.004	1.065 ± 0.002	1.095 ± 0.003
7–8	1.064 ± 0.017	1.068 ± 0.005	1.061 ± 0.005	1.066 ± 0.002	1.100 ± 0.004
8–10	1.070 ± 0.007	1.067 ± 0.004	1.054 ± 0.005	1.061 ± 0.002	1.101 ± 0.003
10–12	1.089 ± 0.010	1.073 ± 0.003	1.083 ± 0.022	1.062 ± 0.003	1.107 ± 0.006
12–14	1.095 ± 0.015	1.069 ± 0.009	1.063 ± 0.028	1.049 ± 0.005	1.114 ± 0.008
14–16	1.059 ± 0.032	1.076 ± 0.006	1.085 ± 0.014	1.061 ± 0.006	1.107 ± 0.013
16–20	1.109 ± 0.032	1.088 ± 0.003	1.096 ± 0.021	1.050 ± 0.004	1.120 ± 0.009

Table 6.6: Data/MC Scale Factors for 2012 Data in all five regions of the detector as a function of p_{T}. The uncertainties include systematic and statistical components as described in Section 6.2.1.

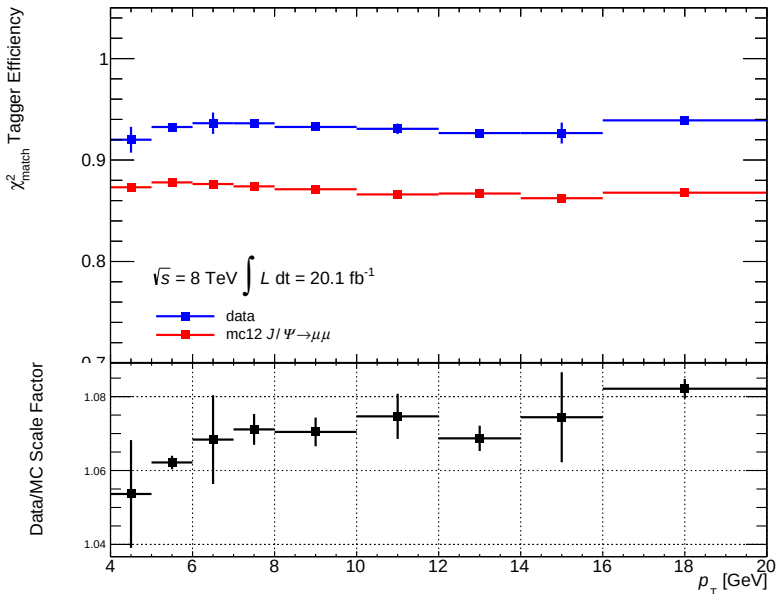

Figure 6.8: Distribution of the χ^2_{match} efficiency as measured in data and MC, and the associated scale factor with respect to the transverse momentum of the muon probe.

semileptonic decay of b-quarks in $t\bar{t}$ events are produced amongst the tracks associated with the b-jet.

For the results of the calibration on J/ψ to be applicable, the performance of the χ^2_{match} tagger must not affected by the isolation of the muon. In this calibration, the nine isolation variables defined in Section 5.2.1 are considered.

The isolated nature of muons in J/ψ events limits the number of muons available at higher isolation values. This is more significant in simulation compared to the collision data which contains non-isolated muons. There appears to be no dependence on any of the isolation variables examined (Figures 6.14, 6.15 and 6.16).

Dependence on d_0

The dependence on the impact parameter d_0 was examined and no direct dependence is observed. The scale factor shows no structure with respect to d_0 when binned in p_{T} (Figure 6.17). Since the scale factors are binned in η and p_{T}, the correlation between d_0 and p_{T} is taken into account.

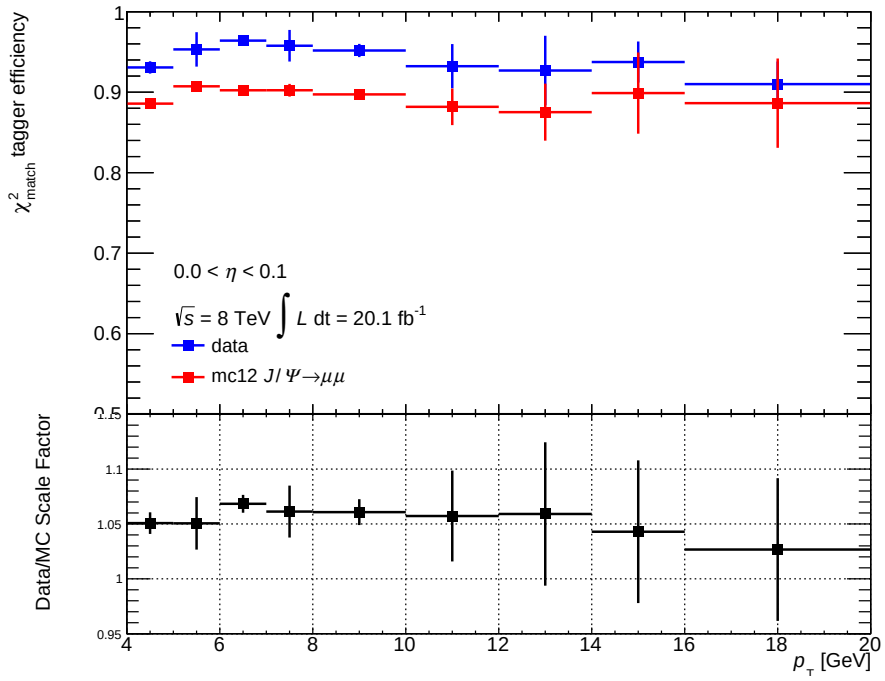

(a) Crack A Region.

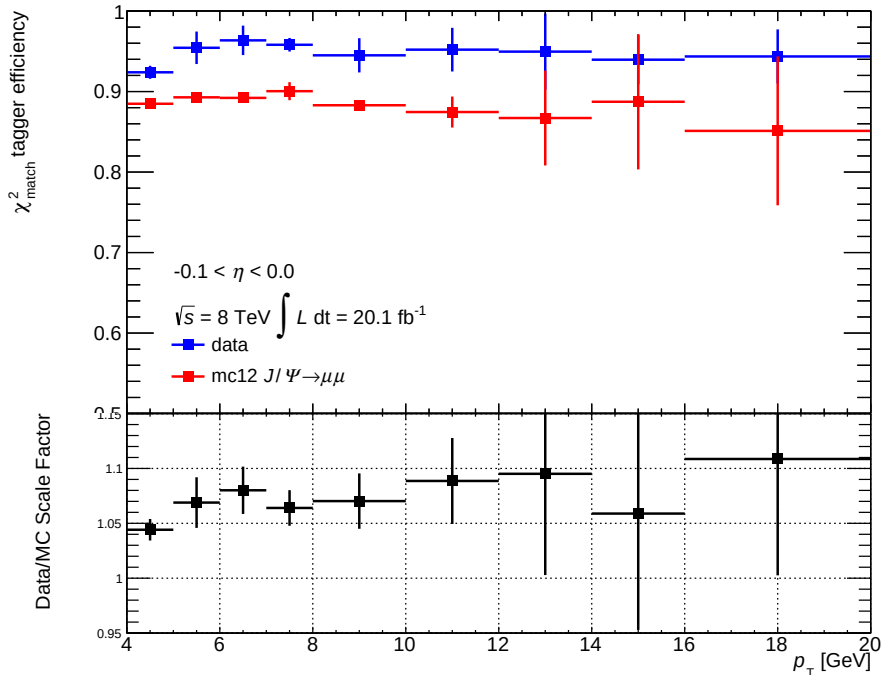

(b) Crack C Region.

Figure 6.9: χ^2_{match} efficiencies and scale factors in the crack region of the detector for side (a) A and (b) C.

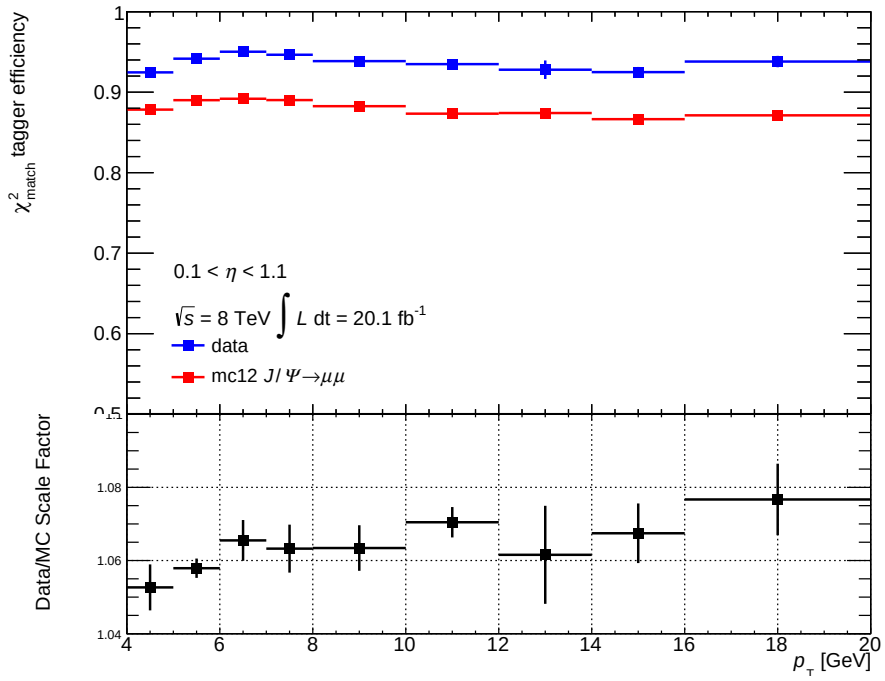

(a) Barrel A Region.

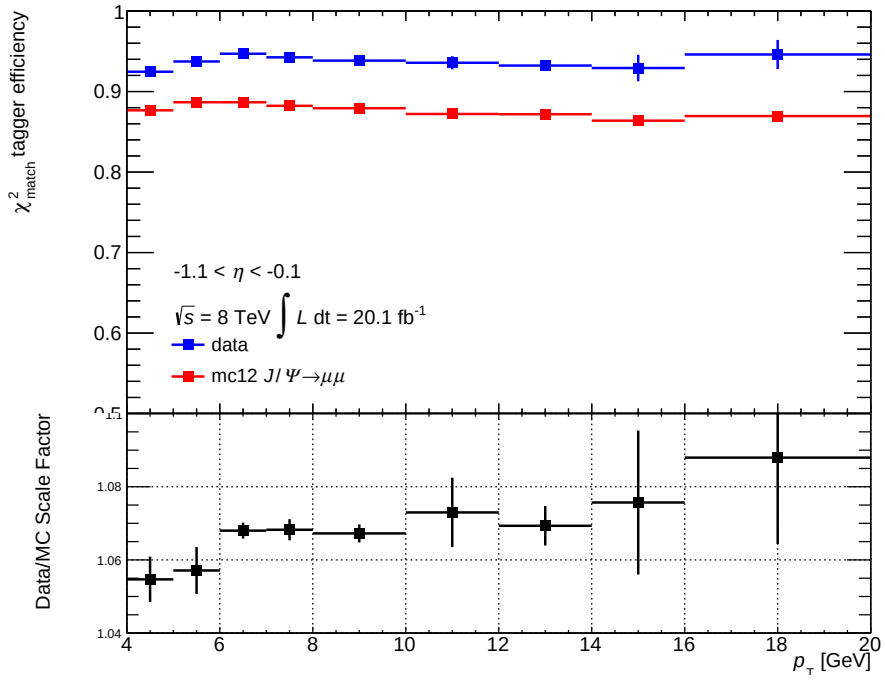

(b) Barrel C Region.

Figure 6.10: χ^2_{match} efficiencies and scale factors in the barrel region of the detector for side (a) A and (b) C.

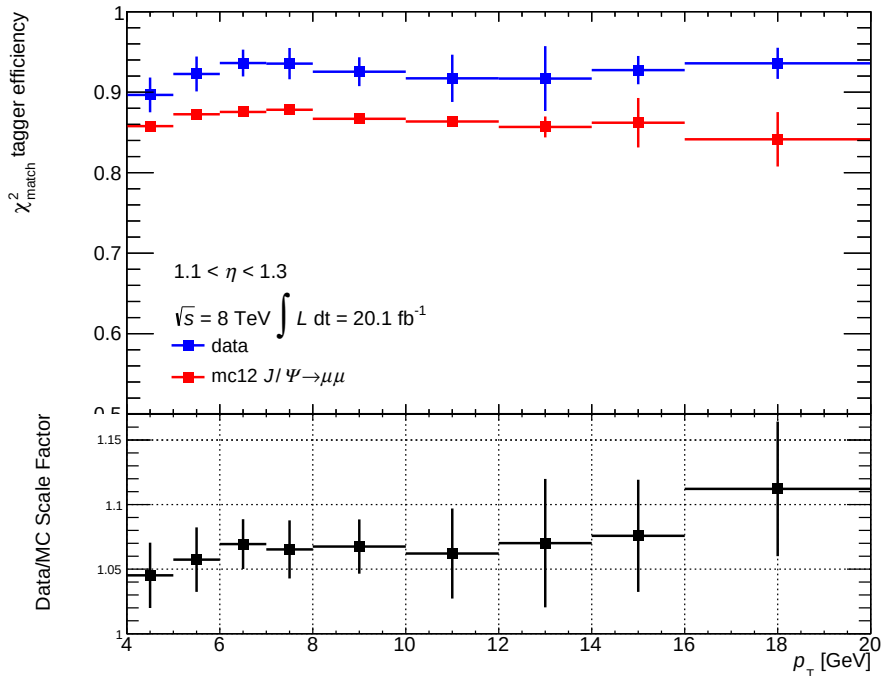

(a) Transition A Region.

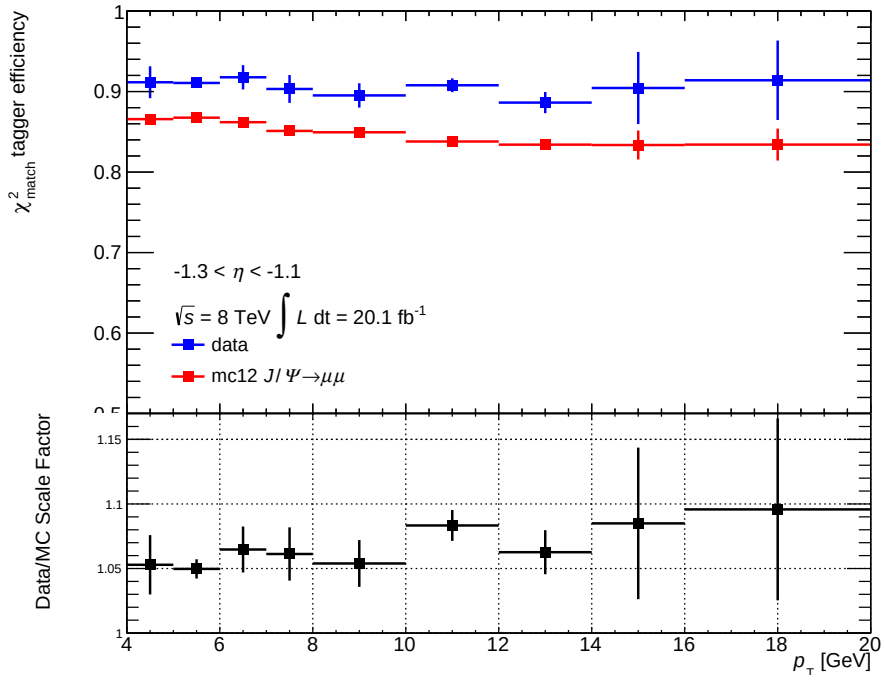

(b) Transition C Region.

Figure 6.11: χ^2_{match} efficiencies and scale factors in the transition region of the detector for side (a) A and (b) C.

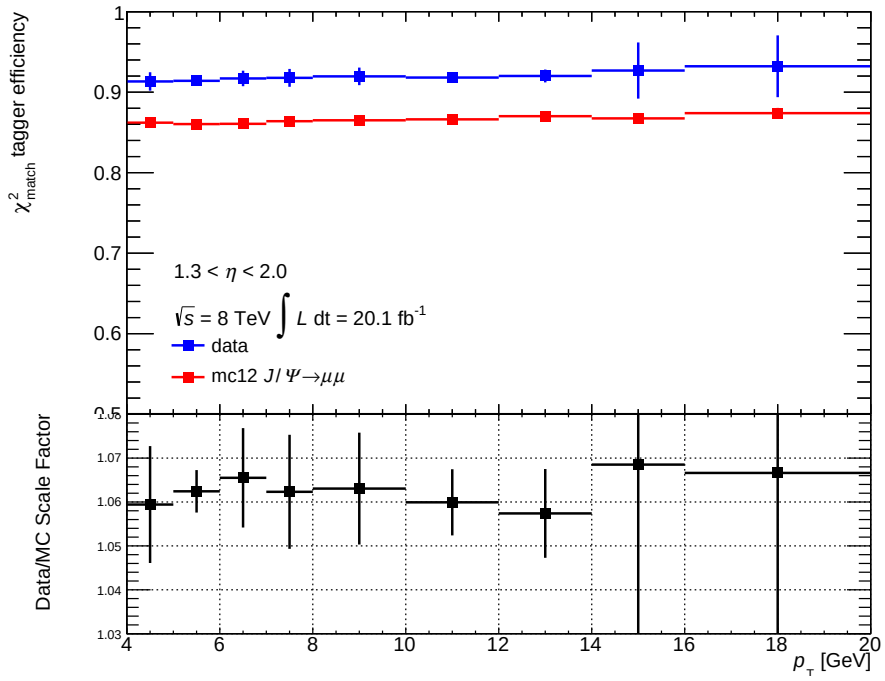

(a) End-cap A Region.

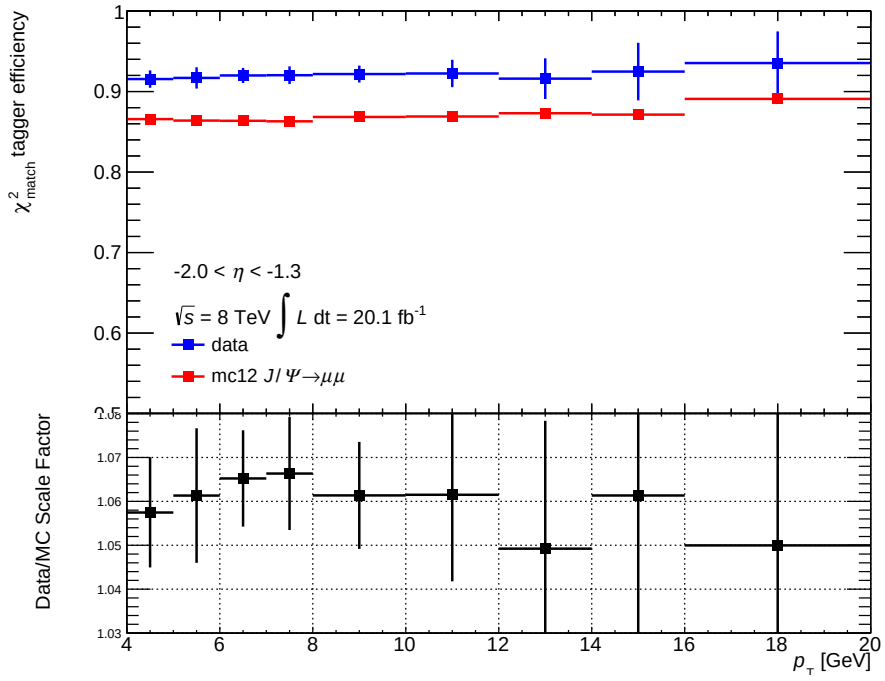

(b) End-cap C Region.

Figure 6.12: χ^2_{match} efficiencies and scale factors in the end-cap region of the detector for side (a) A and (b) C.

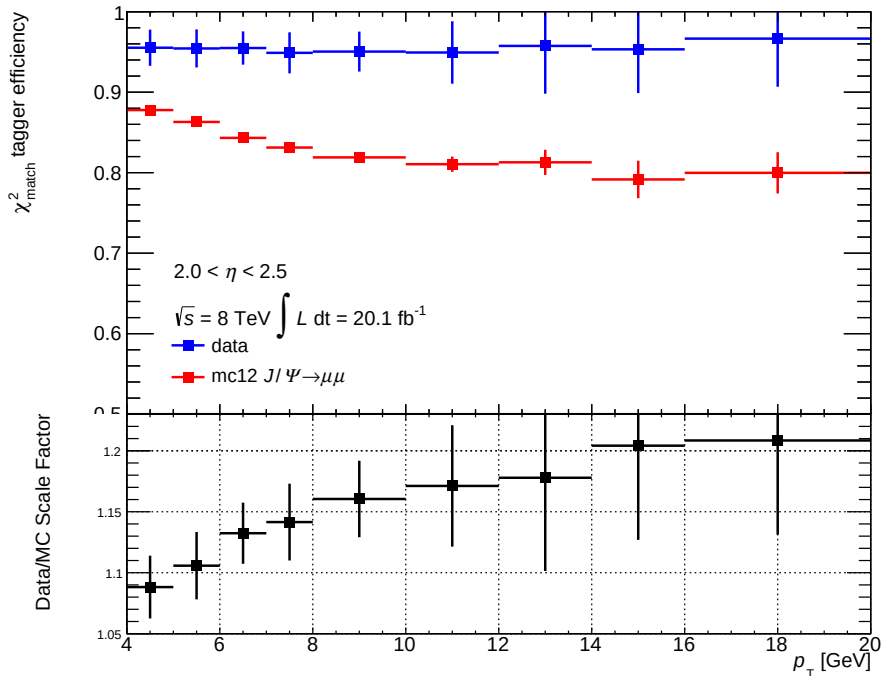

(a) Forward A Region.

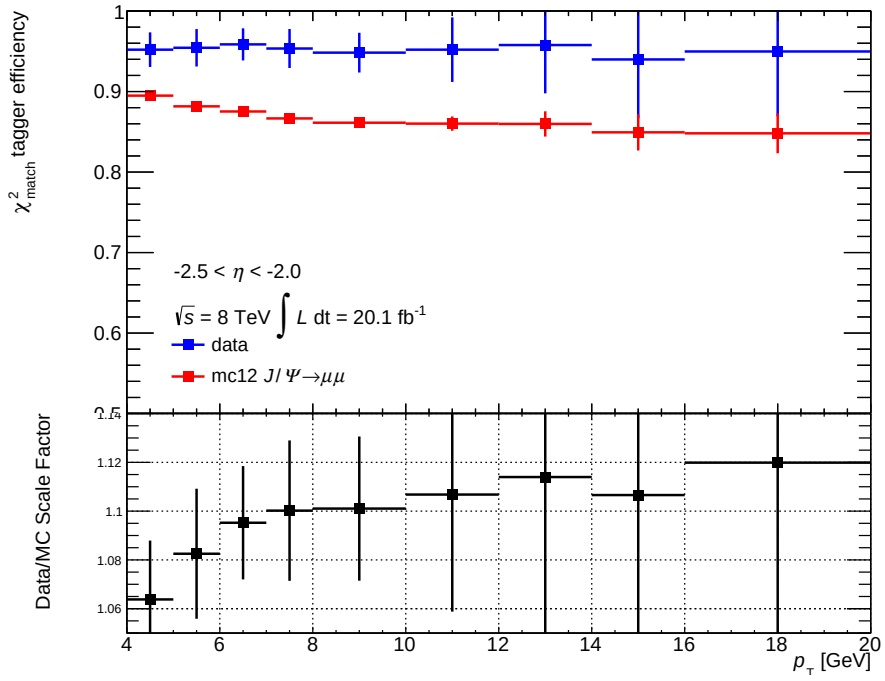

(b) Forward C Region.

Figure 6.13: χ^2_{match} efficiencies and scale factors in the forward region of the detector for side (a) A and (b) C.

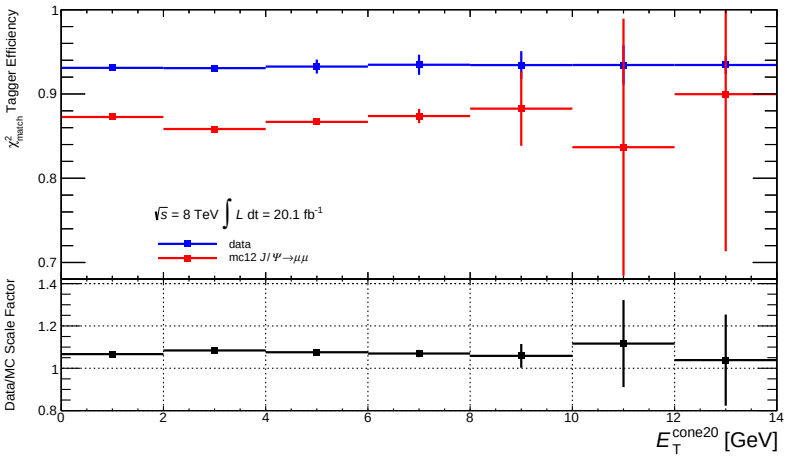

(a) $\sum E_{\mathrm{T}}$ in cone $\Delta R = 0.2$

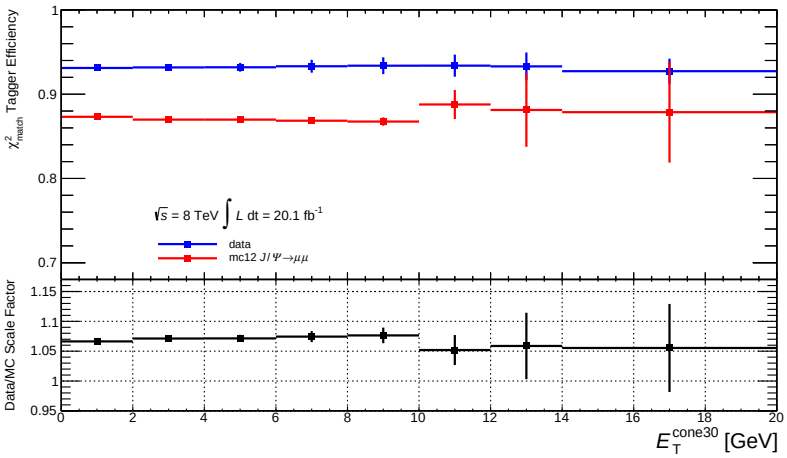

(b) $\sum E_{\mathrm{T}}$ in cone $\Delta R = 0.3$

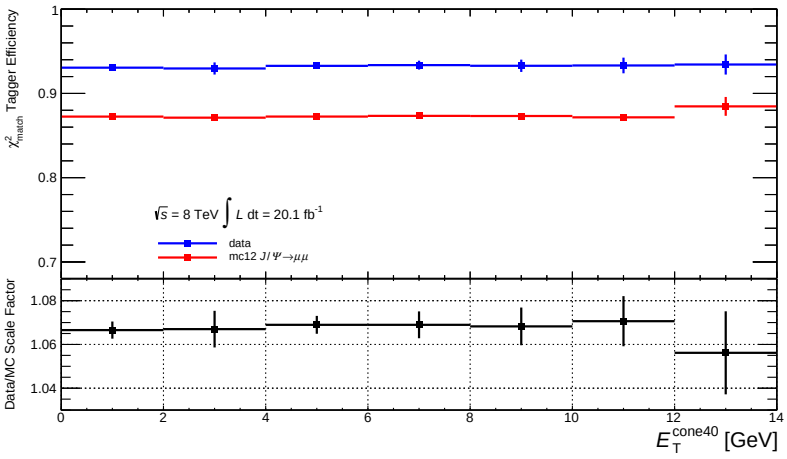

(c) $\sum E_{\mathrm{T}}$ in cone $\Delta R = 0.4$

Figure 6.14: χ^2_{DoF} efficiencies and scale factor with respect to $\sum E_{\mathrm{T}}$ for a muon probe that passes the SMT requirements.

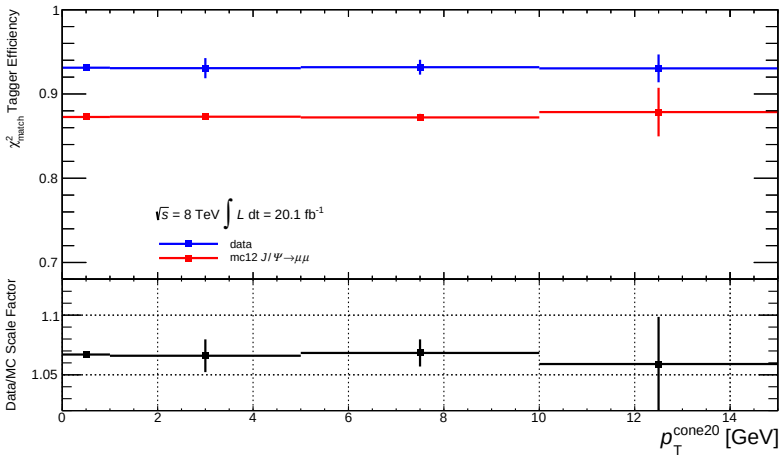

(a) $\sum p_{\mathrm{T}}$ in cone $\Delta R = 0.2$

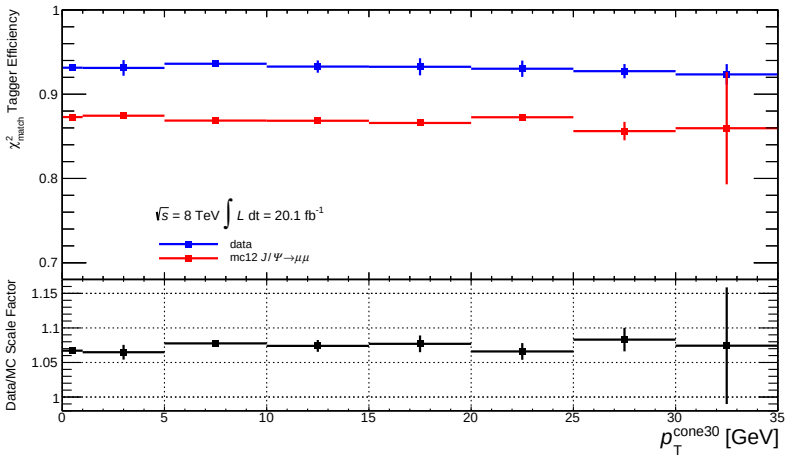

(b) $\sum p_{\mathrm{T}}$ in cone $\Delta R = 0.3$

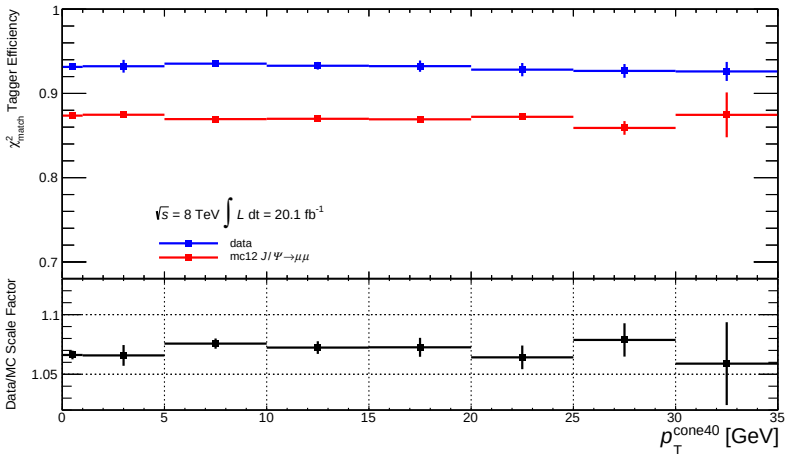

(c) $\sum p_{\mathrm{T}}$ in cone $\Delta R = 0.4$

Figure 6.15: χ^2_{DoF} efficiencies and scale factor with respect to $\sum p_{\mathrm{T}}$ for a muon probe that passes the SMT requirements.

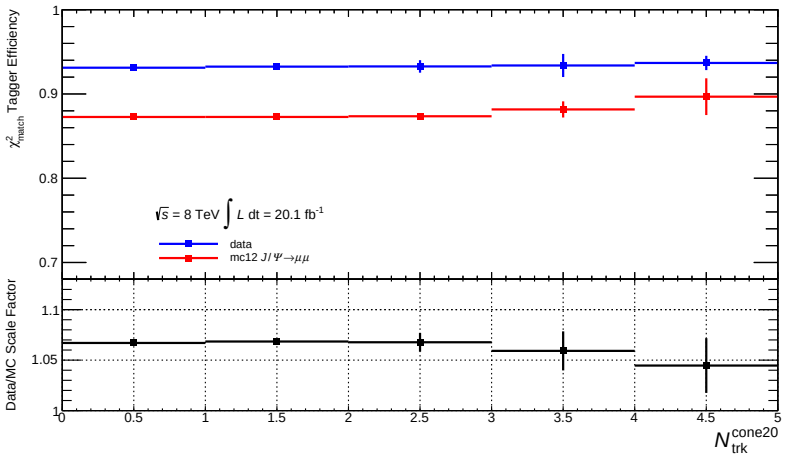

(a) N_{trk} in cone $\Delta R = 0.2$

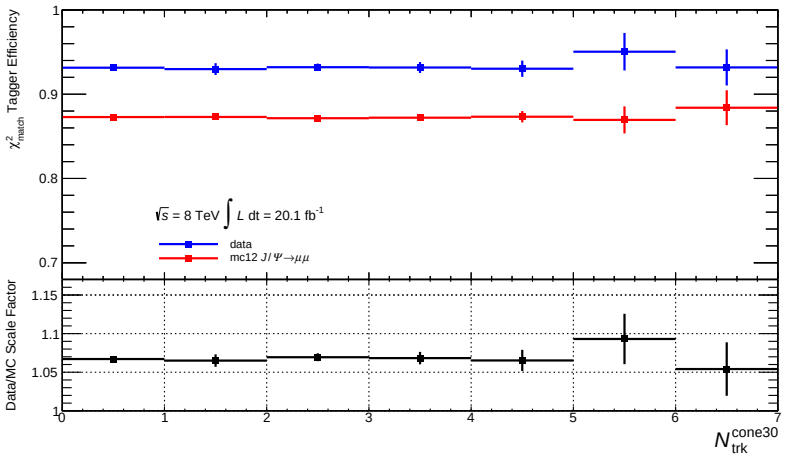

(b) N_{trk} in cone $\Delta R = 0.3$

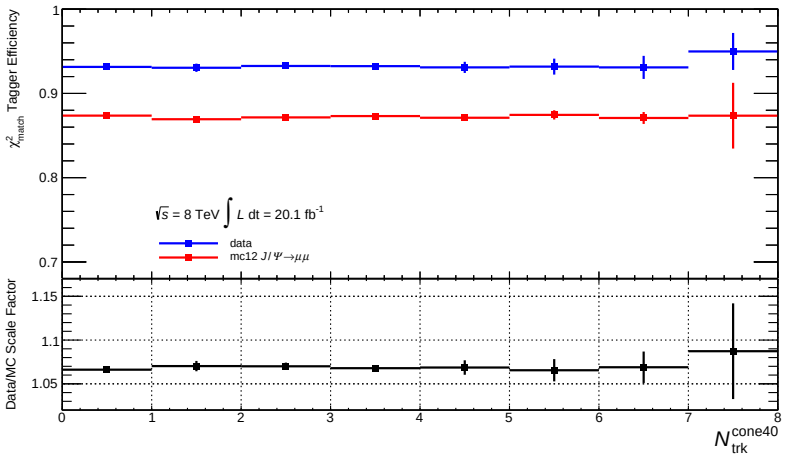

(c) N_{trk} in cone $\Delta R = 0.4$

Figure 6.16: χ^2_{DoF} efficiencies and scale factor with to N_{tracks} for a muon probe that passes the SMT requirements.

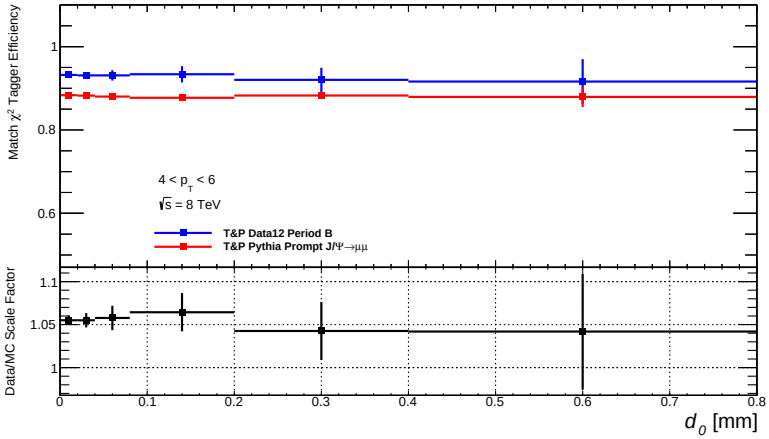

(a) $4\,\text{GeV} < p_\text{T} < 6\,\text{GeV}$

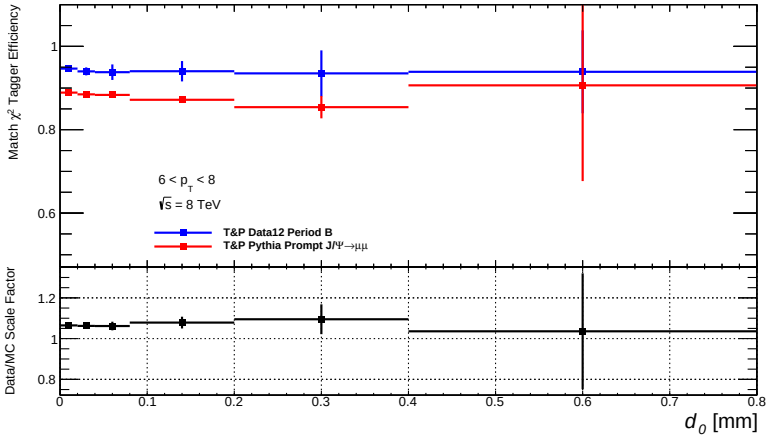

(b) $6\,\text{GeV} < p_\text{T} < 8\,\text{GeV}$

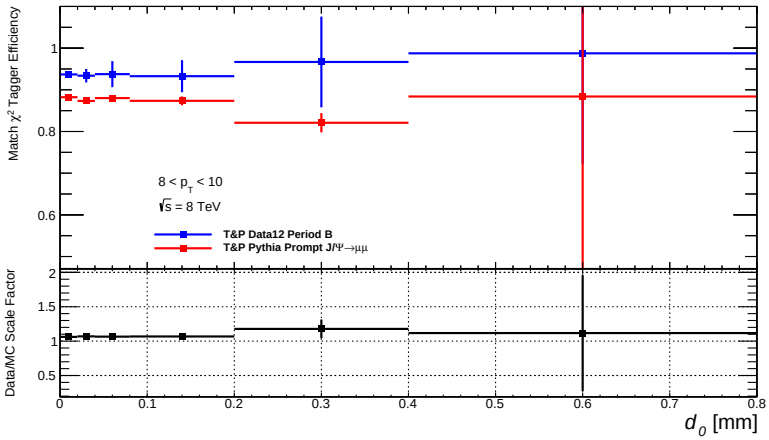

(c) $8\,\text{GeV} < p_\text{T} < 10\,\text{GeV}$

Figure 6.17: Distribution of the χ^2_match efficiencies and scale factor with respect to impact parameter d_0 for muon probes with p_T in the ranges (a) 4–6 GeV, (b) 6–8 GeV and (c) 8–10 GeV. The measurement was carried out only on Period B of 2012 ATLAS collision data.

6.5 Scale factor discrepancy

A discrepancy between the 2011 and 2012 scale factors is observed. The SFs in the 2011 analysis do not deviate substantially from unity, while the 2012 SFs deviate as much as $15\,\%$. The efficiency measured in the 2012 collision data appears to be consistent with the 2011 result, however in simulation the efficiency is measured to be lower. The difference in SF appears to come from a mismodelling of the χ^2_{DoF} variable.

A number of factors can contribute to such a mismodelling including inaccurate description of the alignment of detector components, and the description of the material used in the detector. Both of these can result in mismodelling of the kinematic variables that make up the χ^2_{DoF} variable.

In order to find the source of the discrepancy the components of the χ^2_{DoF} variable were examined. The *pull* of a kinematic variable is defined here as

$$X_{\text{pull}} = \frac{X^{\text{ID}} - X^{\text{MS}}}{\sqrt{\sigma^2_{X^{\text{ID}}} + \sigma^2_{X^{\text{MS}}}}} \tag{6.11}$$

where X is any of the five kinematic components of χ^2_{match}, and σ is the uncertainty on that variable. The pulls are shown in terms of the azimuthal angle, the polar angle, the longitudinal and transverse impact parameters and the charge over momentum (q/p) of the muon probe in in Figure 6.18. The transverse momentum is related to the q/p by $p_{\text{T}} = |1/(q/p)|\sin(\theta)$ and the pseudorapidity is defined in terms of the angle θ in Section 4. All distributions appear to suffer from some mismodelling in MC, with the θ distributions being the worst. By construction the two variables are strongly correlated [85], so its not unexpected to observe a discrepancy simultaneously in both of these arguments. Such a discrepancy could be caused by a mismodelling of the alignment of the detector components.

A study to test the effects of different alignment profiles was carried out. Several samples with different alignment profiles were compared to a small sample of 8 TeV collision data from a single run. These include the nominal prompt J/ψ sample used in this calibration, the J/ψ sample used for the 2011 calibration, a $Z \to \mu\mu$ sample where the detector is perfectly aligned, a 2011 $Z \to \mu\mu$ sample with an updated detector geometry description, and a $Z \to \mu\mu$ sample with the nominal smeared alignment. The smeared alignment is produced by distorting the

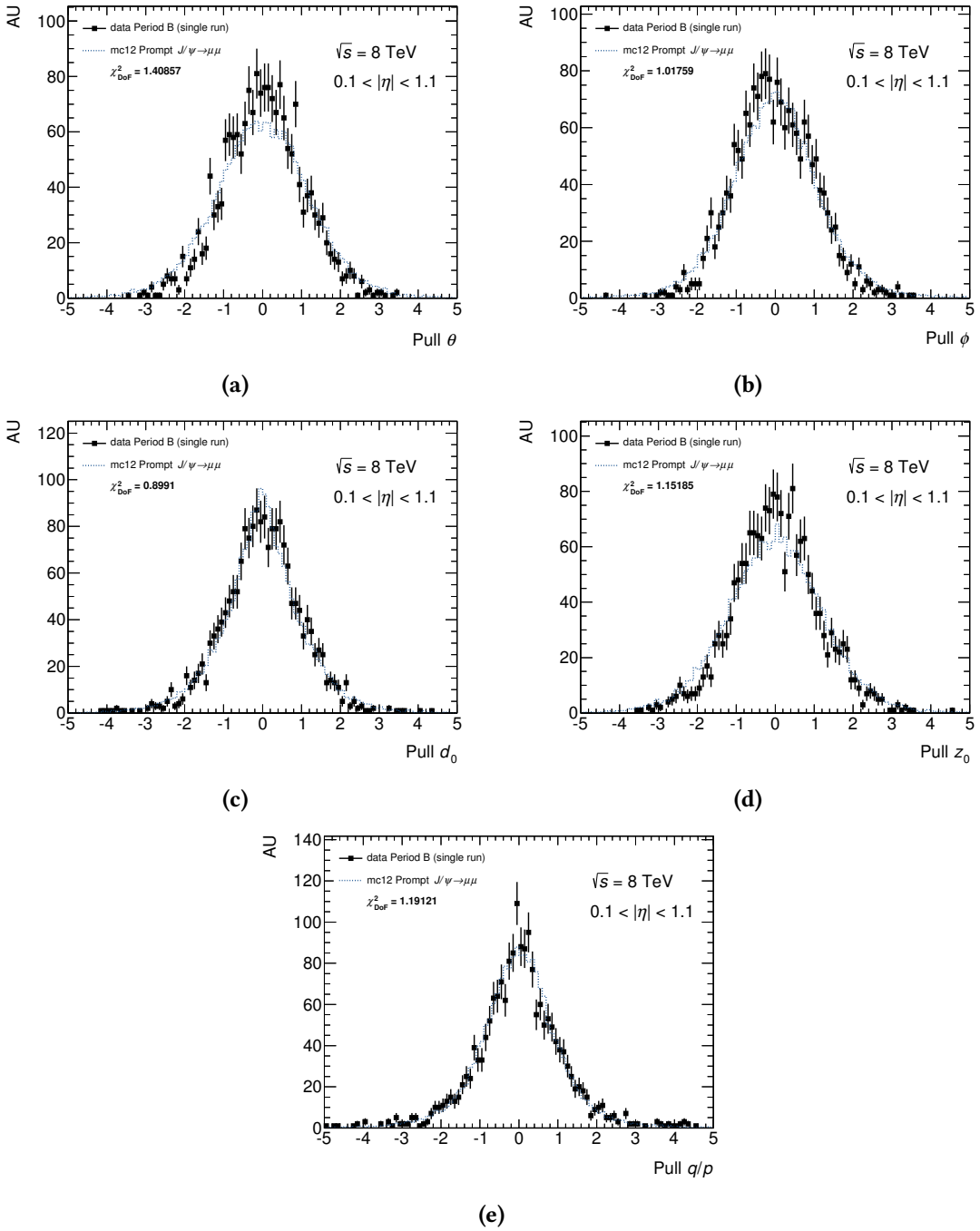

Figure 6.18: Distribution of the pull (see 6.11) of components of χ^2_{DoF} as measured in the ID for muon probes in the barrel region for collision data (squares) and prompt J/ψ simulation (dotted). Shown are (a) θ, (b) ϕ, (c) d_0, (d) z_0 and (e) q/p. Also shown is the goodness-of-fit χ^2_{DoF} between the collision data and the simulation. These distributions are based on smaller samples and are normalized to unit area.

ideal alignment sample within the current measured alignment uncertainties. This procedure is not designed to perfectly represent the details in the misalignment of the ATLAS detector, but rather simulates a detector which is as well aligned as the real detector. These two profiles are compared in small samples of $Z \to \mu\mu$ events.

A sample of well reconstructed muons is selected by matching STACO CB muons to truth muons[1] from Z or J/ψ. The χ^2_{DoF} distribution of these muons is then compared for muons with p_{T} between 4 and 25 GeV.

As expected, the alignment profile does have an effect on the χ^2_{DoF} distribution, particularly in the lower end (Figure 6.19). However, this effect is not sufficiently large to account, on its own, for the discrepancy between simulation and data in all bins. A pseudo-efficiency of the χ^2_{match} selection is obtained by taking the area under the curve below 3.2 and dividing it to the total area. The results are summarized in Table 6.7. The overall difference between the 2011 and 2012 J/ψ samples is approximately $5\,\%$, not sufficient to cover the discrepancy between data and MC.

Sample	Pseudo-efficiency [%]
Data $\sqrt{s} = 8$ TeV	94.35 ± 0.02
$\boldsymbol{J/\psi \to \mu\mu}$	
Nominal 2011	95.22 ± 0.02
Nominal 2012	90.59 ± 0.02
$\boldsymbol{Z \to \mu\mu}$	
Nominal 2012	92.44 ± 0.03
Ideal alignment 2012	91.37 ± 0.03
New geometry 2011	91.43 ± 0.03

Table 6.7: Summary of χ^2_{match} tagger efficiencies as measured in all tested samples.

6.5.1 Future developments

As can be seen from Figure 6.18e, the momentum appears to be well modelled in both data and simulation. As a result, an alternative variable known as the momentum imbalance is currently

[1] These are the muons present in the truth information.

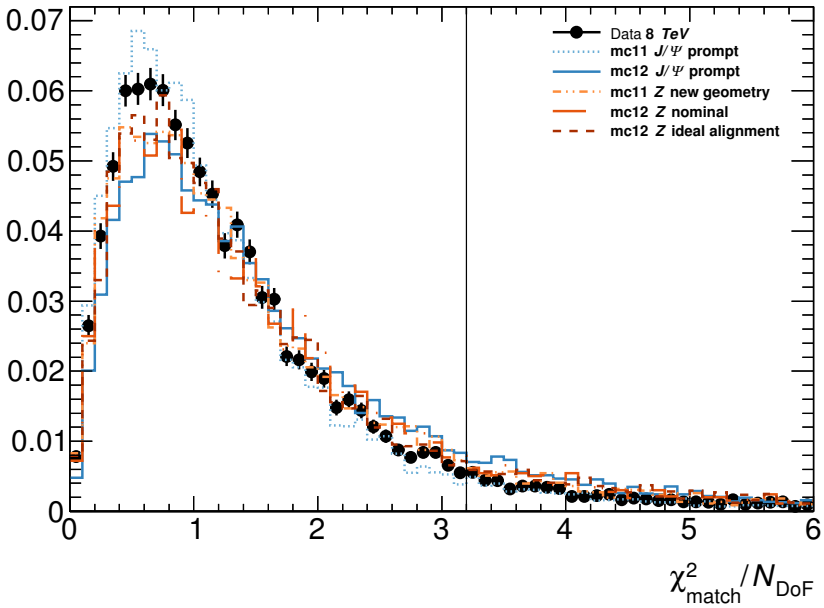

Figure 6.19: Distribution of χ^2_{DoF} of STACO CB muons from collision data (circle), a nominal 2012 $Z \to \mu\mu$ sample (solid), a 2012 $Z \to \mu\mu$ sample with ideal detector alignment (dashed), a 2011 $Z \to \mu\mu$ sample with updated detector description (dashed-double dot), $J/\psi \to \mu\mu$ with nominal alignment at $\sqrt{s} = 8\,\mathrm{TeV}$ (solid) and $J/\psi \to \mu\mu$ with smeared alignment at $\sqrt{s} = 7\,\mathrm{TeV}$ as used in the 2011 analysis (dotted). Distributions are normalized to unit area.

being studied. The momentum imbalance is defined as

$$\text{Mom. Imb.} = \frac{p^{\text{ID}} - p^{\text{ME}}}{p^{\text{ID}}} \tag{6.12}$$

where p^{ID} is the momentum of the muon track as measured in the ID and p^{ME} is measured in the MS extrapolated (ME) back to the primary vertex. This extrapolation takes into account the loss of momentum that occurs when the muon traverses through the detector material.

The momentum imbalance distribution for the aforementioned samples is shown in Figure 6.20. Measurements of the efficiency using momentum imbalance have been carried out, and the collision data results appear to be well-modelled in simulation. The selection using momentum imbalance requires Mom. Imb. < 0.1 as background sources tend to peak above this threshold. From full studies currently being carried out, the momentum imbalance at this operating point exhibits similar performance to the χ^2_{match} version of the tagger.

The pseudo-efficiency for this selection as measured in the aforementioned samples are shown in Table 6.8. These appear to be less affected by the transition from 2011 reconstruction and 2012 reconstruction techniques. In addition, changes in the detector alignment and geometry description affect the pseudo-efficiency substantially less than the χ^2_{DoF} selection.

Sample	Pseudo-efficiency [%]
$\boldsymbol{J/\psi \to \mu\mu}$	
Nominal 2011	92.81 ± 0.02
Nominal 2012	93.57 ± 0.02
$\boldsymbol{Z \to \mu\mu}$	
New geometry 2011	94.20 ± 0.03
Nominal 2012	94.19 ± 0.03
Ideal alignment 2012	94.46 ± 0.02

Table 6.8: Summary of momentum imbalance efficiencies as measured in all tested samples.

Following a comparison of the reconstruction efficiencies with those obtained by members of the MCP group, the pairing selection has been loosened to allow for multiple probes per tag. It is possible for the correct probe to be further away from the tag in z_0 than other spurious tracks. By forcing the selection of the closest ID track in z_0, the sample of probes is contaminated with non-muons resulting in a lower than expected reconstruction efficiency.

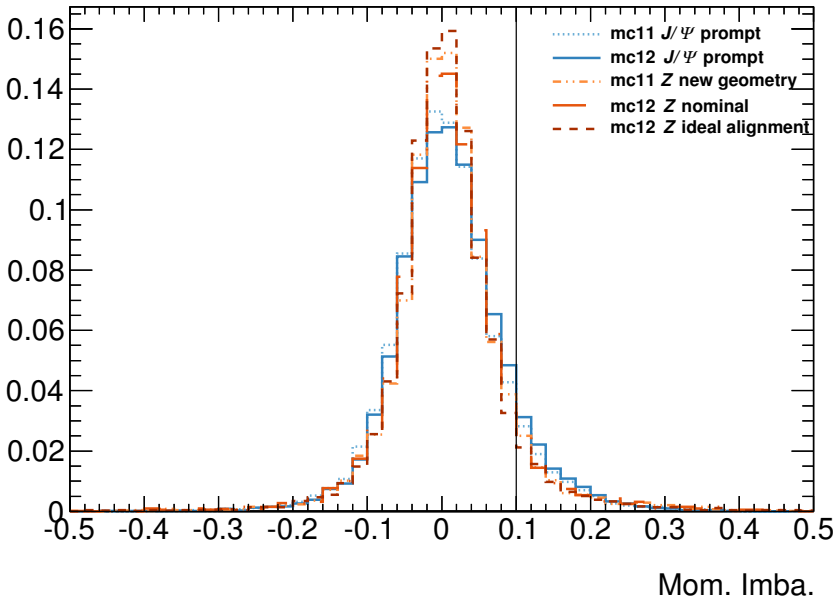

Figure 6.20: Distribution of momentum imbalance of STACO CB muons from a nominal 2012 $Z \to \mu\mu$ sample (solid), a 2012 $Z \to \mu\mu$ sample with ideal detector alignment (dashed), a 2011 $Z \to \mu\mu$ sample with updated detector description (dashed-double dot), $J/\psi \to \mu\mu$ with nominal alignment at $\sqrt{s} = 8$ TeV (solid) and $J/\psi \to \mu\mu$ with smeared at $\sqrt{s} = 7$ TeV as used in the 2011 analysis (dotted). Distributions are normalized to unit area.

This increases the data available for invariant mass fitting and more importantly, has increased the reconstruction efficiency across the η-p_{T} phase space.

Overall, the mismodelling of χ^2_{match} in simulation cannot be fully explained in all tested bins by the description of the alignment alone. Additional testing could be performed on samples with different material description. If the χ^2_{match} distribution is substantially affected, this along with the alignment description could explain the difference between collision data and simulation.

Chapter 7

Measurement of the $t\bar{t}$ cross section in the ℓ+jets channel using SMT

This section describes a $t\bar{t}$ cross section measurement carried out by the joint RHUL and QMUL group.

Presented here is a measurement of the top quark pair production cross section at $\sqrt{s} = 7$ TeV in the lepton plus jets channel, with at least one of the b-quarks in the event decaying semileptonically producing a soft muon. The presence of such a jet is determined by the use of the χ^2_{match}-based SMT tagger described in Section 5.2.4.

7.1 Collision data and simulated samples

This measurement is based on collision data recorded by ATLAS in 2011 at the LHC running with $\sqrt{s} = 7$ TeV. After applying quality cuts based on the beam and detector conditions, the dataset contains an integrated luminosity of (4.66 ± 0.08) fb^{-1}. Several simulated samples are used in this analysis, including the signal process and all backgrounds excluding the multijet background source. The $t\bar{t}$ signal sample was simulated with MC@NLO v4.01 [86, 87] interfaced to HERWIG [88] for parton showering and hadronization, and JIMMY [89] for underlying event simulation. The W/Z+jets samples were generated using ALPGEN [90] interfaced into HERWIG+JIMMY. The single top samples were generated using MC@NLO interfaced to HERWIG+JIMMY for the s and Wt channels, and AcerMC [91] interfaced to PYTHIA [92] for the t channel. Finally, the diboson samples ($WW/WZ/ZZ$) were generated using HERWIG alone.

Source	Branching Ratio [%] (Ratio to PDG)		
	PDG	HERWIG	PYTHIA
$b \to \mu$	10.95 ± 0.29	9.57 ± 0.03 (1.14 ± 0.03)	10.01 ± 0.03 (1.09 ± 0.03)
$b \to \tau \to \mu$	0.42 ± 0.04	0.70 ± 0.02 (0.60 ± 0.06)	0.67 ± 0.01 (0.62 ± 0.06)
$b \to c \to \mu^+$	8.02 ± 0.19	8.24 ± 0.03 (0.97 ± 0.02)	8.89 ± 0.03 (0.90 ± 0.02)
$b \to \bar{c} \to \mu^-$	1.60 ± 0.50	2.51 ± 0.02 (0.64 ± 0.20)	2.66 ± 0.02 (0.60 ± 0.19)

Table 7.1: List of the $b \to \mu$ branching ratios used in the HERWIG and PYTHIA generators compared to the reference PDG values [19].

This analysis is based on the tagging of muons from semileptonic decays of b-quarks. In order to obtain accurate event yields it is important that the simulation correctly models the inclusive production rate of soft muons, and the individual BR for all production chains (Table 5.1). To this end, each event with a soft muon is re-weighted such that the BRs conform with the latest measured values as quoted in Ref. [19]. The reference BR and the values used by HERWIG and PYTHIA are shown in Table 7.1.

7.2 Object identification and event selection

The selection criteria used in this analysis are based on the nominal $\sqrt{s} = 7\,\text{TeV}$ selections recommended by the ATLAS top group. Some alterations have been implemented to adapt to the usage of the χ^2_{match} tagger instead of the standard MV1 method for b-jet tagging. Collision and simulation events are required to have fired an inclusive single electron or muon trigger with offline-reconstructed candidates with $p_{\text{T}} > 25\,\text{GeV}$ for electrons and $p_{\text{T}} > 20\,\text{GeV}$ for muons. Electrons are required to have $|\eta| < 2.47$ and not lie within the transition between the barrel and end-cap calorimeters ($1.37 < |\eta| < 1.52$). They must satisfy the *tight* identification criteria as described in Appendix A. Electrons are required to be isolated using cuts on calorimeter isolation ($E_{\text{T}}^{\text{cone20}}$) and momentum isolation ($p_{\text{T}}^{\text{cone30}}$) as defined in Section 6.4. The cut values for both are defined so as to maintain an efficiency of $90\,\%$. The isolation requirements are designed to reduce the amount of multijet background where reconstructed electrons are not produced in isolation.

Muon candidates are reconstructed using the MUID combined algorithm (see Section 5.2.2),

and must lie within the coverage of ID ($|\eta| < 2.5$). The combined track is obtained by fitting hits in the ID and MS. The muon is required to be isolated in both tracking and calorimeter isolation with $E_{\mathrm{T}}^{\mathrm{cone20}} < 4\,\mathrm{GeV}$ and $p_{\mathrm{T}}^{\mathrm{cone30}} < 2.5\,\mathrm{GeV}$, and to be well separated from the jet by at least $\Delta R > 0.4$. Events must contain exactly one selected muon or one selected electron.

Jets are reconstructed using the anti-k_t algorithm with a distance parameter $R = 0.4$. Topo-clusters at the EM scale are used as inputs to the algorithm and JES corrections are applied to the resulting jets. They are also required to have a $p_{\mathrm{T}} > 25\,\mathrm{GeV}$ and $|\eta| < 2.5$. The *jet vertex fraction* (JVF) defined as:

$$\mathrm{JVF} = \frac{\sum p_{\mathrm{T}} \text{ of jet tracks from PV}}{\sum p_{\mathrm{T}} \text{ of all jet tracks}} \tag{7.1}$$

has to be larger than 0.75. The JVF cut is implemented to remove jets from minimum bias interactions. Finally, jets within $\Delta R < 0.2$ of an electron are rejected.

The transverse mass of the W boson $m_{\mathrm{T},W}$ is reconstructed from the signal lepton and the missing transverse energy:

$$m_{\mathrm{T},W} = \sqrt{2p_{\mathrm{T}}^{\ell}p_{\mathrm{T}}^{\nu}[1 - \cos\phi^{\ell} - \phi^{\nu}]} \tag{7.2}$$

where $E_{\mathrm{T}}^{\mathrm{miss}}$ is associated with the neutrino to calculate p_{T}^{ν} and ϕ^{ν}.

In the e+jets analysis, a large amount of missing transverse energy is required ($> 30\,\mathrm{GeV}$) to account for the escaping neutrino. A cut is also applied on the measured $m_{\mathrm{T},W}$, which must be larger than $30\,\mathrm{GeV}$. In the μ+jets channel the $E_{\mathrm{T}}^{\mathrm{miss}}$ cut is looser ($E_{\mathrm{T}}^{\mathrm{miss}} > 20\,\mathrm{GeV}$) and a triangular cut $E_{\mathrm{T}}^{\mathrm{miss}} + m_{\mathrm{T},W} > 60\,\mathrm{GeV}$ is applied.

For both channels, a minimum of three selected jets is required. Given the final-state signature, it is reasonable to request four or more jets in the event. It was found that the three jets inclusive selection yielded a lower statistical uncertainty, and more importantly a smaller event generator systematic uncertainty. These uncertainties are described in more detail in Section 7.4.

All events which pass these selections are labelled as "pretag" events. Those events which contain at least one jet tagged by the SMT algorithm are labelled as "tagged" events. In the μ+jets channel, requirements are placed on the invariant mass of the soft muon and the signal muon $m_{\mu\mu}$ to remove contributions from dimuon Υ ($8\,\mathrm{GeV} \leq m_{\mu\mu} \leq 11\,\mathrm{GeV}$) and Z

($80\,\text{GeV} \leq m_{\mu\mu} \leq 100\,\text{GeV}$) decays. Finally, the signal muon must be a different object than the soft muon ($\Delta R > 0.01$).

The efficiency of the full selection as measured on the $t\bar{t}$ signal sample is $1.42\,\%$ in the e+jets channel and $2.15\,\%$ in the μ+jets channel. These efficiencies include both lepton plus jets and dilepton events with at least three jets and at least one jet tagged by the SMT algorithm. Acceptance to fully hadronic events is negligible.

7.3 Background estimation

Lepton plus jets $t\bar{t}$ events have a varied final state signature that includes a lepton, multiple jets including b-jets and missing energy. As a result $t\bar{t}$ analyses must take into account several sources of background: diboson, W+jets, Z+jets, single-top and multijet.

W+jets events (e.g. Figure 7.1a) enter the signal region due to the presence of a real lepton, missing transverse energy, and one or two real b-jets or mistagged LF jets. Gluon emissions can also occur resulting in additional jets. The W+jets background is estimated using data-driven methods.

Z+jets events (e.g. Figure 7.1b) can pass the selection if one of the two leptons is not identified. This can happen if, for example, the lepton enters the crack region. This results in an overall imbalance of momentum interpreted as missing energy. The Z boson can be created in association with a gluon which results in real b-jets or mistagged LF jets. This source of background, along with single-top and diboson, is estimated from MC simulation.

Diboson production (e.g. Figure 7.1c) such as WW, ZZ or WZ enters the signal region due to the presence of real leptons, missing energy (from real or missed leptons), and HF or mistagged LF jets.

Multijet events which contain LF and/or b-quarks enter the signal region when they contain a reconstructed lepton that passes the isolation requirement. These can include both real electrons and objects that fake electrons. Real electron sources include photon conversions in the detector material, and semileptonic decay of b- and c-quarks. Fake electrons can be reconstructed from tracks overlapping with photons, and jets with few charged tracks or small amounts of energy deposited in the hadronic calorimeter.

There are several sources of real muons including those from the decay-in-flight of pions or

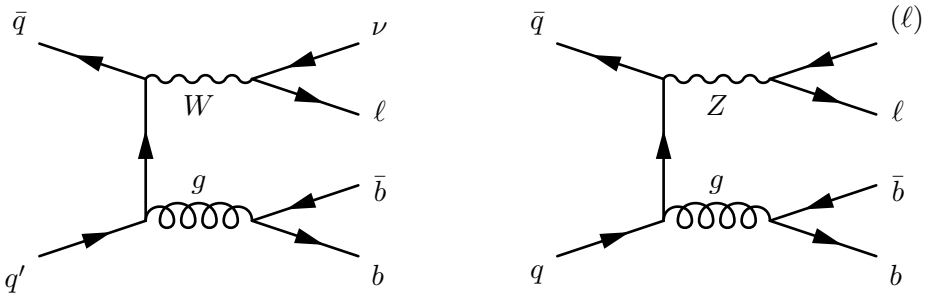

(a) $W\bar{b}b$+jets production.

(b) $Z\bar{b}b$+jets production.

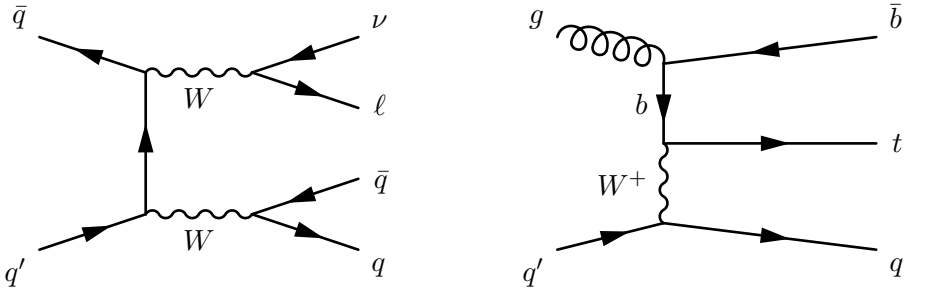

(c) WW production.

(d) Single-top production.

Figure 7.1: Some of the Feynman diagrams of background processes from W/Z+jets, diboson and single-top.

kaons within the tracking region. There are also several objects that fake the muon signature such as hadrons that do not shower in the detector material, and *punch-through* hadrons from hadronic showers [1]. The semileptonic decay of b- and c-quarks can also produce muons which constitute a background to the signal W-muon. However, in this analysis these soft muons are exploited by the SMT tagger.

A significant amount of fake $E_{\mathrm{T}}^{\mathrm{miss}}$ must also be reconstructed for the multijet events to pass the selection. There are numerous sources of fake $E_{\mathrm{T}}^{\mathrm{miss}}$ such as uninstrumented sections of the detector, noisy or dead calorimeter cells, misreconstruction of physics objects, fake muons from punch-through and pile-up. Although the probability of each of these processes is small, the large production cross section for multijet make it an important background.

Using simulation to model these effects is not possible as they depend on the conditions in the detector, some of which are random or short-lived. The data sample required for such a study would also have to be very large, making this approach impractical. As a result the multijet background is estimated using data-driven methods.

[1] Hadrons which are not contained within the calorimetry and enter the muon system

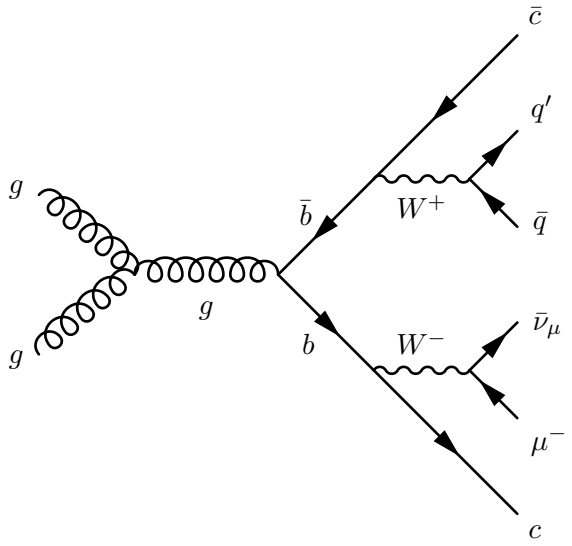

(a) Multijet with real lepton

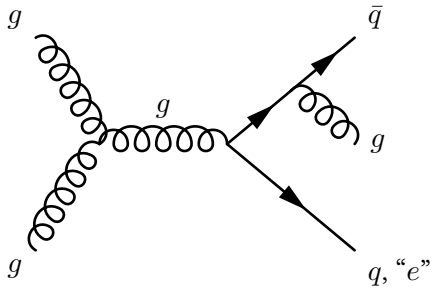

(b) Multijet with fake lepton

Figure 7.2: Feynman diagrams of some of the multijet background sources. Shown are (a) $b\bar{b}$ which produce a real lepton and multiple jets, and (b) where one of the quark jets is misidentified as an electron.

7.3.1 Multijet in the electron channel

The estimation of the multijet background in the electron channel is done using two different methodologies. The *matrix method* [93], which is used to obtain the central value, and the so-called *ABCD method* as a cross-check.

The pretag estimate is obtained using the matrix method, while the tagged estimate is obtained by scaling the pretag values by an SMT multijet event tagging-rate.

The matrix method is implemented as follows: in addition to the standard electron selection, a looser selection is defined where the isolation requirement is removed. Events are categorized by whether they pass the standard selection or only loose selection[2]. The number of events in each category is the sum of events with "real" electrons and "fake" electrons[3] as follows:

$$N^{\text{loose}} = N^{\text{loose}}_{\text{real}} + N^{\text{loose}}_{\text{fake}} \tag{7.3}$$

$$N^{\text{std}} = rN^{\text{loose}}_{\text{real}} + fN^{\text{loose}}_{\text{fake}} \tag{7.4}$$

where r and f are the portion of loose events that pass the standard selection, given that the event contains a "real" or "fake" electron.

Given a measured N^{std} and N^{loose} in data, and if f and r are known the number of events with a fake electron that passes the standard selection can be calculated:

$$N^{\text{std}}_{\text{fake}} = fN^{\text{loose}}_{\text{fake}} = f\frac{N^{\text{std}} - rN^{\text{loose}}}{(f-r)} \tag{7.5}$$

The relative efficiency r is measured from an inclusive sample of $Z \to ee$ events and f is measured from a sample of events with exactly one loose electron, at least one jet with a $p_{\text{T}} > 25\,\text{GeV}$, and $E^{\text{miss}}_{\text{T}} < 20\,\text{GeV}$. This sample is enriched with events that have low missing energy and one electron likely coming from a jet faking a lepton. An uncertainty of $50\,\%$ is assigned to the pretag estimate to cover the respective uncertainties on f and r. The values of r and f are binned as a function of lepton pseudorapidity.

To derive the tagged estimate, the pretag estimates are scaled by the probability of SMT tagging a multijet event. The tagging probability of multijet events $R^{\text{multijet}}_{\text{SMT}}$ is derived from

[2] All muons that pass the standard selection by construction also pass the loose selection

[3] Here, fake means background muons that are not the signal muon.

control regions defined by the isolation of the electron and the $E_{\mathrm{T}}^{\mathrm{miss}}$ cut defined in the event selection, as shown in Figure 7.3.

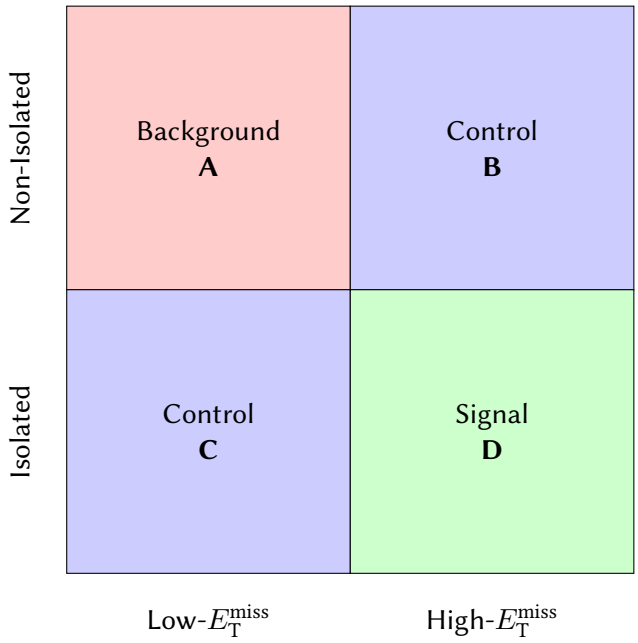

Figure 7.3: Diagram of the $E_{\mathrm{T}}^{\mathrm{miss}}$-isolation phase space. Shown are the four regions as defined by the event selection.

These four regions are labelled A through D: a background-dominated region (A), containing events with low-$E_{\mathrm{T}}^{\mathrm{miss}}$ and no isolated electrons; a control region (B) with an isolated electron; a control region (C) with low-$E_{\mathrm{T}}^{\mathrm{miss}}$; and the signal region (D), with events that pass the event selection. Events in each region represent a different multijet process that allows these to pass the event selection.

The tagging-rate is simply defined as

$$R_{\mathrm{SMT}}^{\mathrm{multijet}} = \frac{N_{\mathrm{tagged}}^{\mathrm{multijet}}}{N_{\mathrm{pretag}}^{\mathrm{multijet}}} \tag{7.6}$$

where N is the number of events in the region. Contaminations from non-multijet events such as W+jets, Z+jets, $t\bar{t}$, single-top, and diboson events are subtracted using MC simulation. Thus the yield in each region is defined as

$$N^{\mathrm{multijet}} = N^{\mathrm{data}} - N^{W\text{+jets}} - N^{Z\text{+jets}} - N^{t\bar{t}} - N^{\mathrm{diboson}} - N^{\text{single-top}} \tag{7.7}$$

The largest sources of contamination are $t\bar{t}$, W+jets, and Z+jets, as shown in Table 7.2 for pretag level and in Table 7.3 for tag level. Single-top and diboson contribute less than 1 % in most bins and are therefore not shown here. As expected, Region A contains the least amount of contamination from other processes and is dominated by multijet events. Regions B and C are dominated by W+jets in all jet-bins because of the presence a real lepton and $E_{\mathrm{T}}^{\mathrm{miss}}$ from a real neutrino. The Z+jets contamination is most significant in region C due to the requirement of an isolated electron but low-$E_{\mathrm{T}}^{\mathrm{miss}}$.

Jet-bin	Contamination by [%]		
	$t\bar{t}$	W+jets	Z+jets
Region A			
1	0.01 ± 0.00	6.99 ± 1.74	2.57 ± 0.01
2	0.13 ± 0.02	6.44 ± 1.61	3.87 ± 0.04
3	1.14 ± 0.18	5.72 ± 1.43	4.77 ± 0.09
$\geq$3	2.24 ± 0.34	5.64 ± 1.41	4.90 ± 0.08
Region B			
1	0.12 ± 0.02	39.1 ± 9.8	1.64 ± 0.02
2	1.47 ± 0.22	30.6 ± 7.6	2.61 ± 0.05
3	8.42 ± 1.27	22.7 ± 5.7	3.21 ± 0.09
$\geq$3	14.0 ± 2.0	20.2 ± 5.0	3.14 ± 0.08
Region C			
1	0.02 ± 0.00	43.3 ± 11.0	20.0 ± 0.4
2	0.49 ± 0.07	36.4 ± 9.0	26.4 ± 1.1
3	4.63 ± 0.70	29.6 ± 7.4	29.9 ± 0.3
$\geq$3	8.77 ± 1.32	28.0 ± 7.0	29.2 ± 0.2

Table 7.2: The portion of contamination in data in all control regions at pretag level. The uncertainties shown include statistical and systematic contributions.

The distributions of various kinematic variables are shown in Figure 7.4 after contamination is removed in region B. The $E_{\mathrm{T}}^{\mathrm{miss}}$ distribution exhibits a long tail due to the aforementioned sources of fake reconstructed missing energy. The momentum distributions at both pretag and tag level point to the presence of hard objects reconstructed as leptons in the multijet background likely coming from misidentified jets. The χ^2_{DoF} distribution of the SMT muons

Jet-bin	Contamination by [%]		
	$t\bar{t}$	W+jets	Z+jets
Region A			
1	0.05 ± 0.02	4.46 ± 1.13	0.43 ± 0.05
2	0.82 ± 0.12	4.89 ± 1.25	1.33 ± 0.15
3	5.64 ± 0.54	4.97 ± 1.34	1.54 ± 0.27
$\geq$3	10.4 ± 1.7	4.50 ± 1.19	1.75 ± 0.24
Region B			
1	1.09 ± 0.23	26.6 ± 6.7	0.43 ± 0.11
2	8.71 ± 1.40	29.9 ± 7.5	1.02 ± 0.18
3	28.3 ± 4.5	12.2 ± 3.2	1.08 ± 0.24
$\geq$3	38.9 ± 6.0	9.84 ± 2.51	0.95 ± 0.16
Region C			
1	0.36 ± 0.09	53.6 ± 13.4	4.78 ± 0.26
2	4.86 ± 0.80	41.5 ± 10.4	11.5 ± 0.6
3	26.5 ± 4.2	30.6 ± 7.8	11.7 ± 0.9
$\geq$3	40.5 ± 6.2	24.2 ± 6.1	10.1 ± 0.6

Table 7.3: The portion of contamination in data in all control regions at tagged level. The uncertainties shown include statistical and systematic contributions.

peaks at low χ^2_{DoF} values pointing to a good quality of fit between the ID and MS tracks of the muon. As expected the SMT muons are soft just as those in $t\bar{t}$ events. One possible source of these soft muons is semileptonic decays of HF quarks.

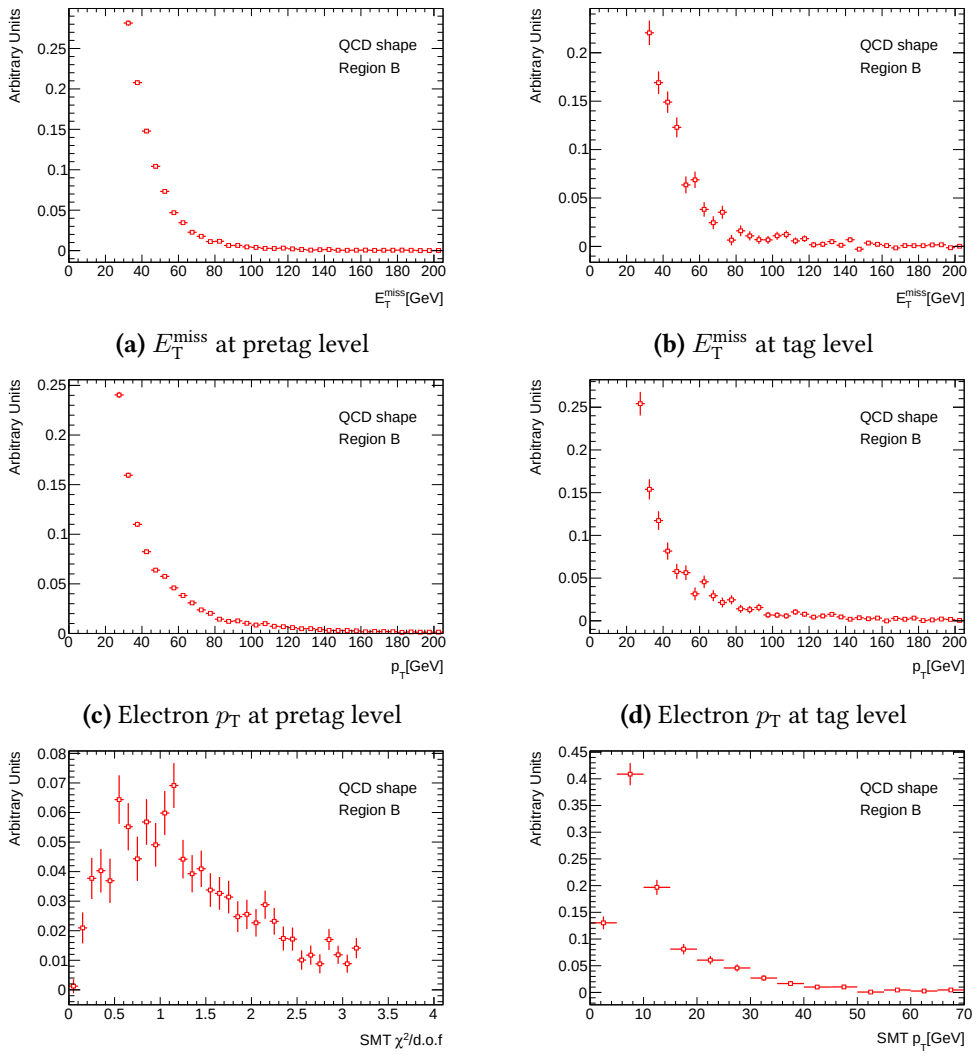

(a) $E_{\mathrm{T}}^{\mathrm{miss}}$ at pretag level

(b) $E_{\mathrm{T}}^{\mathrm{miss}}$ at tag level

(c) Electron p_{T} at pretag level

(d) Electron p_{T} at tag level

(e) SMT muon χ^2_{DoF} at tag level

(f) SMT muon p_{T} at tag level

Figure 7.4: Kinematic distributions measured in region B (high-$E_{\mathrm{T}}^{\mathrm{miss}}$ and non-isolated) at pretag and tagged level. These distributions are obtained by subtracting non-multijet contributions using simulation.

The normalization of the $t\bar{t}$ contribution is initially based on the theoretical cross section. An estimate for the multijet contribution is determined using this cross section and a new measured $t\bar{t}$ cross section is obtained. This cross section is used to rescale the $t\bar{t}$ contribution and a new cross section is obtained. This process is repeated until the measured cross section

stabilizes. Only two iterations are needed.

The uncertainty on the tagging-rate contains statistical and systematic contributions. The systematic uncertainty includes the uncertainty on the cross section of the $t\bar{t}$ and W+jets samples, $15\,\%$ and $25\,\%$ respectively; uncertainty from the calibration of the SMT tagger; and uncertainties associated with the BR re-weighting. For more detail on the tagger-specific uncertainty, see Section 7.4. The dominant source of uncertainty depends on the region and jet-bin. In regions where contamination is high, the uncertainty from W+jets and $t\bar{t}$ are more significant.

The final tagging-rate is the unweighted average of all three regions. This definition was chosen as no single type of multijet process is favoured over the others. The uncertainty is half the largest difference in rates between the regions. This covers the entire range of possible tagging-rate values. The tagging-rates per region for each jet-bin, including uncertainty, are shown in Table 7.4.

Jet-bin	SMT tagging-rate R^{SMT} [%]			
	Region A	Region B	Region C	Average
1	1.17 ± 0.01	1.10 ± 0.10	0.609 ± 0.056	0.962 ± 0.446
2	2.25 ± 0.03	2.49 ± 0.10	1.55 ± 0.17	2.09 ± 0.47
3	3.44 ± 0.09	4.31 ± 0.21	2.27 ± 0.85	3.34 ± 1.02
$\geq$3	3.84 ± 0.09	5.14 ± 0.41	2.52 ± 1.30	3.83 ± 1.31

Table 7.4: Results of the SMT multijet tagging-rate measurement in region A (inverted-$E_{\text{T}}^{\text{miss}}$, non-isolated), B (High-$E_{\text{T}}^{\text{miss}}$, non-isolated) and C (low-$E_{\text{T}}^{\text{miss}}$, isolated).

The multijet background estimates in the e+jets channel are shown in Table 7.5. The uncertainties on the final pretag and tagged estimates are dominated by the $50\,\%$ uncertainty on the efficiencies associated with the matrix method pretag estimate.

The ABCD method

The ABCD method relies on a pair of uncorrelated variables to extrapolate the amount of multijet events from a set of control regions into the signal region. First, a two-dimensional phase-space is constructed, in this case the same construct shown in Figure 7.3 is used. If these

Jet-bin	Multijet event yield	
	Pretag	Tagged
1	$145\,000 \pm 72\,000$	1390 ± 700
2	$39\,600 \pm 19\,800$	830 ± 416
3	$11\,300 \pm 5700$	378 ± 190
$\geq$3	$16\,200 \pm 8100$	620 ± 311

Table 7.5: Results of the matrix method estimation of the multijet background in the e+jets channel. The uncertainties are combined statistical and systematics.

two variables are uncorrelated then the following relation holds

$$\frac{N_{\mathrm{D}}^{\mathrm{multijet}}}{N_{\mathrm{C}}^{\mathrm{multijet}}} = \frac{N_{\mathrm{B}}^{\mathrm{multijet}}}{N_{\mathrm{A}}^{\mathrm{multijet}}} \tag{7.8}$$

where $N_{\mathrm{X}}^{\mathrm{Multijet}}$ is the number of multijet events in region X. As with the matrix method, the value of N^{Multijet} is obtained by subtracting the contribution of other processes from the data value using simulation.

This allows an estimation of the number of multijet events that pass the event selection by extrapolating from the background region into the signal region. The uncertainty on the final estimate includes statistical contributions from the yield in each region and the systematic uncertainty on the W+jets and $t\bar{t}$ samples as described. The multijet estimates in all regions at pretag and tagged level are presented in Table 7.6. The uncertainty on the estimate in some jet-bins is smaller than the matrix method estimate. However, in the signal jet-bin ($\geq$3) the uncertainty at tag level is very large. The matrix method estimate is therefore used as the central value and the ABCD estimate is used as a cross-check. Comparing the results from the matrix method and the ABCD method, it appears that both produce compatible results within their uncertainties.

7.3.2 Multijet background in the muon channel

The procedure in the muon channel is similar to that used for the electron channel. A pretag estimate of the multijet fraction in the signal region is obtained using the matrix method. The "real" muon selection efficiency r is measured from an inclusive sample of $Z \to \mu\mu$ events.

Jet-Bin	Multijet event yield	
	Pretag	Tag
1	$99\,000 \pm 48\,000$	565 ± 264
2	$33\,500 \pm 13\,000$	572 ± 272
3	9500 ± 3320	270 ± 220
$\geq$3	$13\,000 \pm 5000$	438 ± 449

Table 7.6: Results of the ABCD method estimation of the multijet background in the e+jets channel. The uncertainty contains statistical and systematic components.

Control region	SMT tagging-rate [%]
Inverted isolation	5.7 ± 0.1
Inverted triangular cut	4.0 ± 0.5
Unweighted average	4.9 ± 0.8

Table 7.7: Summary of tagging-rates as measured in data in the two multijet-dominated regions. The uncertainty quoted includes statistical and systematic contributions. The uncertainty on the unweighted average is set as half of the difference between control regions [1].

The "fake" muon selection efficiency f is obtained from data using two different samples:

- A background-dominated control region where the $E_{\mathrm{T}}^{\mathrm{miss}} + m_{\mathrm{T},W}$ cut is inverted and an additional cut of $m_{\mathrm{T},W} < 20\,\mathrm{GeV}$ is applied.
- A fit to the transverse impact parameter significance distribution where both $E_{\mathrm{T}}^{\mathrm{miss}} + m_{\mathrm{T},W}$ and $E_{\mathrm{T}}^{\mathrm{miss}}$ cuts are inverted.

The central value of the pretag estimate is obtained from an average of these two regions and was found to be $27\,000 \pm 5400$. An uncertainty of 20 % is assigned to the final estimate to account for the uncertainty associated with each region and the difference between them.

The SMT event tagging-rate is obtained from two control regions defined by inverting the $E_{\mathrm{T}}^{\mathrm{miss}}$ and $E_{\mathrm{T}}^{\mathrm{miss}} + m_{\mathrm{T},W}$ cuts, and by inverting the muon isolation requirement. As with the electron analysis, contamination from other non-multijet processes is subtracted using MC simulation. The associated sources of uncertainty are the same as those considered in the electron channel.

The final multijet estimate at tagged level is obtained by multiplying the average pretag estimate by the unweighted tagging-rate. The uncertainty on the unweighted tagging-rate is set to half the difference between the two control regions, as this is larger than the individual uncertainties combined. The final uncertainty is obtained by combining the uncertainties on the pretag estimate and the tagging-rate. The final tagged estimate was found to be 1310 ± 350.

7.3.3 *W*+jets background

The W+jets background is the most dominant background since these events contain a real lepton and $E_{\mathrm{T}}^{\mathrm{miss}}$ from the escaping neutrino. Events can be classified into W+HF, which is the largest contribution; and W+LF where a LF jet is mistagged. Due to the significant uncertainty on the overall normalization of W+jets and the presence of a mistagged LF jet, a data-driven method known as W charge asymmetry [94] is used to estimate this background.

The W charge asymmetry method relies on the charge asymmetry in the production of W-bosons. As the LHC is a proton-proton collider, up-type valence quarks are more prevalent, resulting in an increased rate of W^+ production via $u\bar{d} \to W^+$ or $c\bar{s} \to W^+$ compared to W^- production involving down-type quarks. The ratio of these production cross sections r is theoretically well understood [95]. It is thus possible to use this ratio as measured in MC simulation to determine an overall normalization in data from the following formula:

$$N_{W^+} + N_{W^-} = \frac{N_{W^+}^{\mathrm{MC}} + N_{W^-}^{\mathrm{MC}}}{N_{W^+}^{\mathrm{MC}} - N_{W^-}^{\mathrm{MC}}}(D^+ - D^-) \tag{7.9}$$

$$= \frac{r_{\mathrm{MC}} + 1}{r_{\mathrm{MC}} - 1}(D^+ - D^-) \tag{7.10}$$

where r_{MC} is the ratio as measured in MC and $D^{\pm}$ are the number of events in data with a positively- or negatively-charged lepton. Contributions from other charge asymmetric processes, namely single-top and diboson are removed using MC simulation. This results in an overall normalization for the W+jets background at the pretag level. The flavour of the quarks produced in association with the W-boson is particularly important when performing b-tagging. Events are categorized by the flavour of these accompanying quarks into Wc+jets, $Wb\bar{b}$+jets, $Wc\bar{c}$+jets and W+LF. The tagged level estimate is obtained by multiplying the pretag estimate via a tagging-rate, obtained separately for $b\bar{b}$, $c\bar{c}$, c and LF separately. The overall

Channel	W+jets event yield	
	Pretag	Tagged
e+jets	$59\,300 \pm 5400$	1640 ± 330
μ+jets	$117\,200 \pm 9300$	2900 ± 500

Table 7.8: Results of the W+jets background estimation at pretag and tagged level for the three-jets inclusive selection [1].

tagged estimate is then obtained using the following formula:

$$W_{\text{tag}} = R_{\text{tag}}^{\text{LF}} W_{\text{pretag}}^{\text{LF}} + \sum_{\text{HF}}^{\text{HF}=c,cc,bb} R_{\text{tag}}^{\text{HF}} W_{\text{pretag}}^{\text{HF}} \tag{7.11}$$

where $R_{\text{tag}}^{\text{LF}}$ is defined as the probability to mistag a LF event and $R_{\text{tag}}^{\text{HF}}$ is the probability to correctly tag a HF event. The tagging-rates are obtained from simulation with the SMT scale factors and BR reweighing applied to each tagged jet. The results of the estimation are summarized in Table 7.8.

7.3.4 Background shapes

Kinematic distributions are shown at the tagged level in Figures 7.5 for events with at least three jets in both electron and muon channels. The multijet distributions are taken from data normalized to the obtained estimates. In the electron channel, the multijet shapes are obtained from region B, as defined in Figure 7.3, with the contamination from non-multijet processes removed. The multijet shapes in the muon channel are obtained from the loose selection in data, after the application of per-event weights obtained from the matrix method. SMT muon distributions for both background and signal are shown in Figure 7.6. It is noted that the χ^2_{DoF} distribution is shifted in both channels in data compared to the simulation. Any such discrepancies are accounted for by the χ^2_{DoF} scale factor. Good agreement between data and estimations, both simulation-based and data-driven, is observed in all distributions.

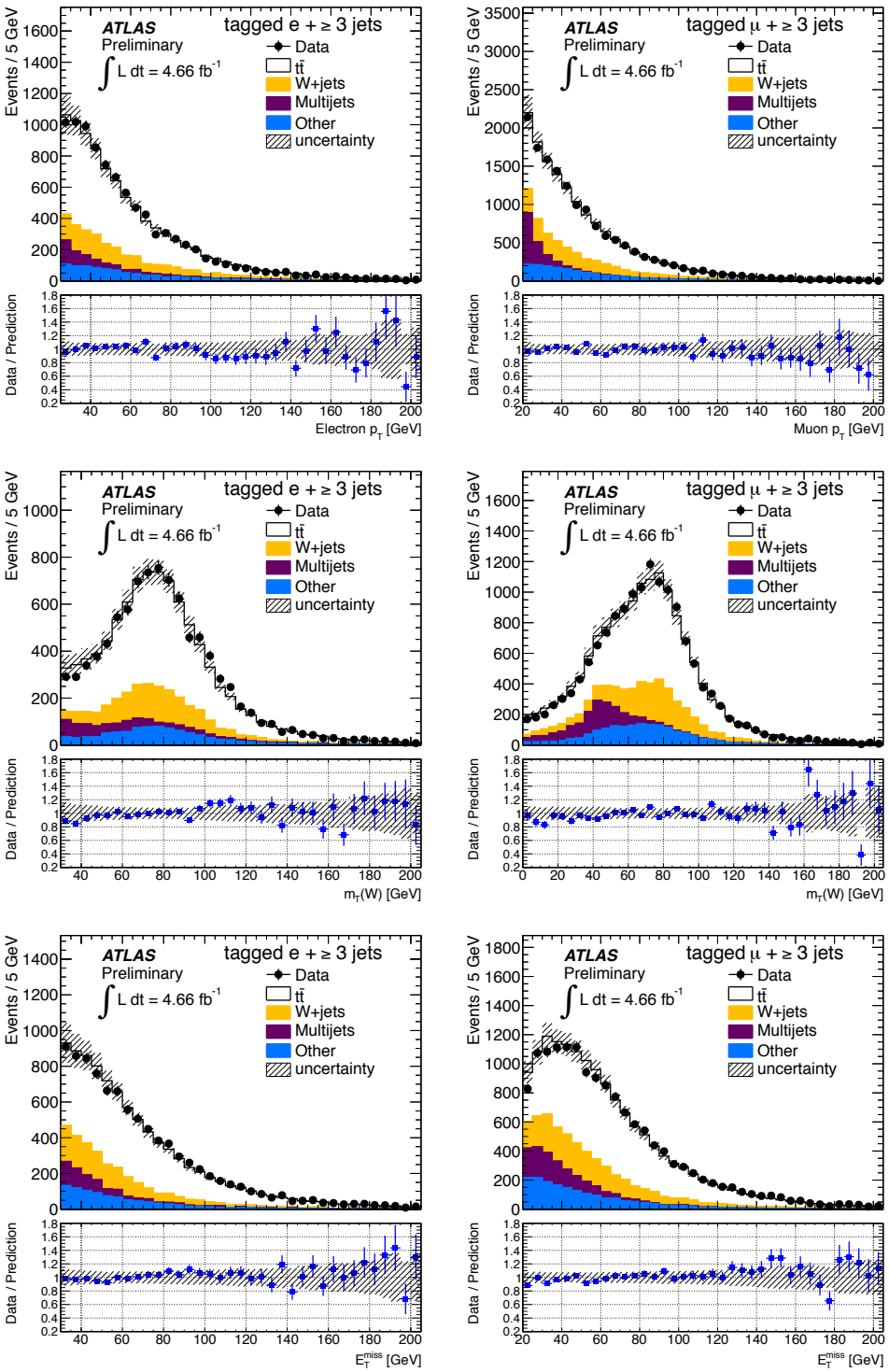

Figure 7.5: Distributions for tagged events in the e+jets (left) and μ+jets (right) channels of (from top to bottom): lepton p_{T}, transverse W mass, and missing transverse energy [1].

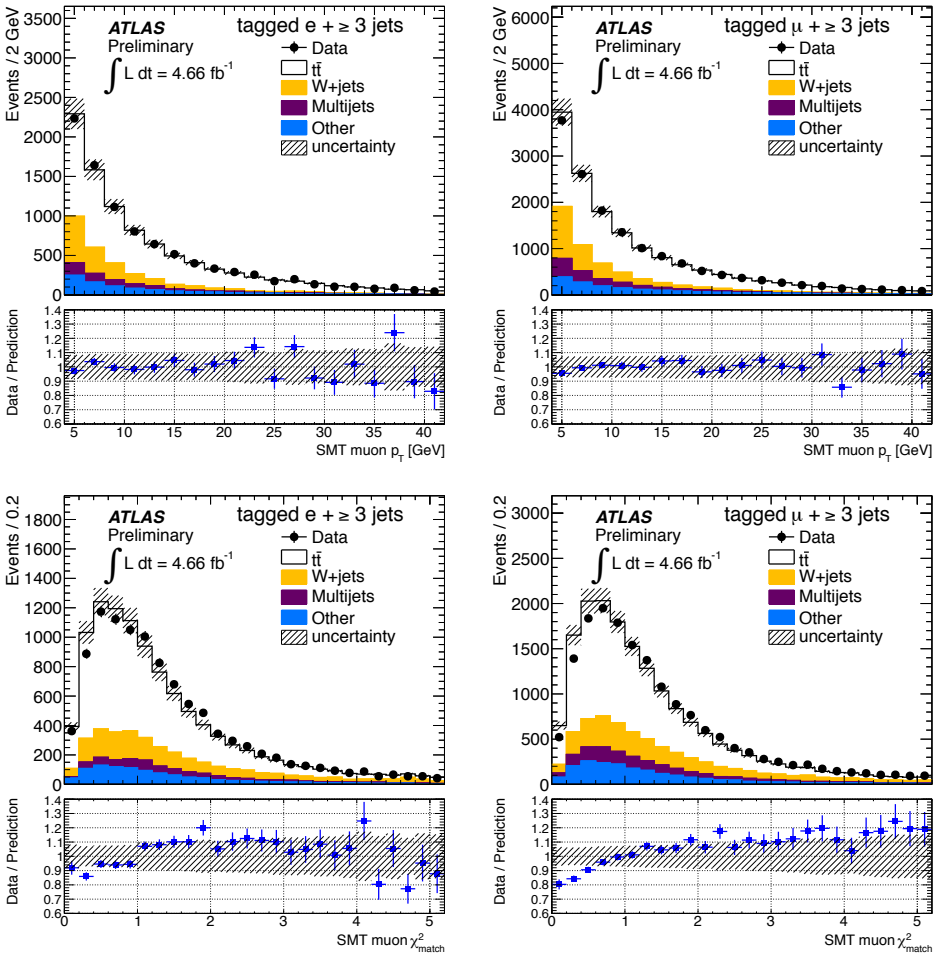

Figure 7.6: Distributions of SMT variables in the e+jets (left) and μ+jets (right) of (from top to bottom): SMT muon p_{T} and SMT muon χ^2_{DoF} [1].

7.4 Systematic uncertainties

The uncertainties associated with the cross section include various sources such as signal simulation, object reconstruction, background estimation, integrated luminosity determination and tagger uncertainties (Table 7.9). The SMT tagger uncertainty is made of the STACO CB reconstruction uncertainty and the uncertainty on the χ^2_{match} efficiency measurement.

The signal modelling uncertainties are evaluated by repeating the cross section measurement while substituting the main $t\bar{t}$ sample with alternate ones. The NLO generator uncertainty covers any differences in the modelling of kinematic distributions at parton level as a result of the hard interaction in different generators. This is evaluated by comparing the signal acceptance in ALPGEN and POWHEG [96, 97] samples to the nominal sample. Initial and final state radiation (ISR/FSR) uncertainty covers the differences in modelling of soft radiation from initial and final state particles. This uncertainty is evaluated in studies on samples generated with AcerMC and PYTHIA, and by varying parameters which affect ISR/FSR simulation in the range consistent with experimental data [98, 99]. The PDF uncertainty is evaluated using three PDF sets: the nominal CT10 [100], MSTW [101], and NNPDF [102]. Several uncertainties are related to each PDF set. Each variation is evaluated by an event-by-event re-weighting of the signal $t\bar{t}$ MC. The total uncertainty assigned to $\sigma_{t\bar{t}}$ is then half the spread of the envelope of all PDF uncertainties [1].

The largest uncertainties come from the background estimation methods, JES corrections, and SMT tagger uncertainties. In the multijet background estimate, the uncertainty associated with the matrix method pretag estimates is the largest contribution at $50\,\%$ of the estimate. The tagger uncertainties, including the $b \rightarrow \mu X$ BR re-weighting uncertainty, contribute approximately $+3.2\,\%/-3.4\,\%$ to the total uncertainty. In comparison, the total b-tagging uncertainty as measured by another ℓ+jets analysis using JetProb is $+4.1\,\%/-3.8\,\%$ [103]. This is larger than the total SMT tagger uncertainty despite including the BR re-weighting uncertainty. Overall, the analysis is dominated by the systematic uncertainty and reduced acceptance due to the BR of $b \rightarrow \mu$ is not significant in this case.

Source	Relative cross section uncertainty [%]		
	e+jets	μ+jets	Combined
Statistical Uncertainty	± 1.5	± 1.3	± 1.0
Object Selection			
Lepton Energy Resolution	$+0.4/-0.3$	$+0.2/-0.01$	$+0.2/-0.1$
Lepton Reco., ID, Trigger	$+2.4/-2.5$	$+1.5/-1.5$	$+1.5/-1.8$
Jet Energy Scale	$+3.8/-4.3$	$+3.2/-3.6$	$+3.5/-3.8$
Jet Energy Resolution	± 0.2	± 0.5	± 0.2
Jet Reconstruction Efficiency	± 0.06	± 0.06	± 0.06
Jet Vertex Fraction	$+1.2/-1.4$	$+1.2/-1.4$	$+1.2/-1.4$
$E_{\mathrm{T}}^{\mathrm{miss}}$ Uncertainty	± 0.06	± 0.08	± 0.07
SMT Calibration			
STACO Reconstruction Eff.	± 1.3	± 1.3	± 1.3
Muon χ^2_{match} Eff.	± 0.6	± 0.6	± 0.6
Background Estimates			
Multijet Normalisation	± 5.2	± 3.9	± 4.4
W+jets Normalisation	± 5.2	± 5.7	± 5.5
Other Bkg Normalisation	± 0.2	± 0.2	± 0.1
Other Bkg Systematics	$+1.6/-1.5$	$+2.5/-2.0$	$+2.2/-1.8$
Signal Simulation			
$b \to \mu X$ Branching Ratio	$+2.9/-3.0$	$+2.9/-3.1$	$+2.9/-3.1$
ISR/FSR	± 2.4	± 0.9	± 1.5
PDF	± 3.2	± 3.0	± 3.1
NLO Generator	± 3.2	± 3.2	± 3.2
Parton Shower	± 2.2	± 2.2	± 2.2
Total Systematics	$+11.1/-11.3$	$+10.2/-10.3$	$+10.5/-10.6$
Integrated Luminosity	± 1.8	± 1.8	± 1.8

Table 7.9: List of cross section uncertainty sources for the three-jets inclusive selection [1].

Sample	Event yields in			
	e+jets		μ+jets	
	Pretag	Tagged	Pretag	Tagged
Data	124 424	9165	227 318	14 940
MC				
$t\bar{t}$	$31\,900 \pm 1300$	5980 ± 350	$52\,100 \pm 1600$	9100 ± 500
Z+jets	$9900\,^{+2500}_{-1400}$	$270\,^{+40}_{-30}$	$11500\,^{+2400}_{-1600}$	$780\,^{+140}_{-100}$
Diboson	$1190\,^{+220}_{-180}$	40 ± 10	$2030\,^{+350}_{-300}$	60 ± 10
Single top	4300 ± 400	630 ± 60	7200 ± 600	980 ± 80
Data-Driven				
Multijet	$16\,200 \pm 8100$	620 ± 310	$27\,000 \pm 5400$	1310 ± 350
W+jets	$59\,300 \pm 5400$	1640 ± 330	$117\,200 \pm 9300$	2900 ± 500
Measured $t\bar{t}$		6000 ± 500		8900 ± 600

Table 7.10: Summary of event yields for signal and background events, as well as the yield measured in data [1].

7.5 Results and conclusion

The event yields in data, signal $t\bar{t}$ MC and background contributions that pass the event selection for both pretag and tagged in the muon and electron channels are shown in Table 7.10.

The final cross section is determined by a cut-and-count method and is calculated as

$$\sigma_{t\bar{t}} = \frac{N_{\text{data}} - N_{\text{bkg}}}{\int L\,\mathrm{d}t \times \epsilon \times \text{BR(noFullHad)}} \tag{7.12}$$

where N_{data} is the total number of events in collision data that pass the event selection, N_{bkg} is the estimated number of background events that pass the event selection, ϵ is the estimated selection efficiency (Table 7.11), and BR(noFullHad) is the semileptonic and dilepton total branching ratio. This BR was calculated using a $W \to \ell\nu$ branching ratio of 0.108 per flavour, and has a value of 0.543. The combined cross section is obtained by combining e+jets and μ+jets event yields.

The final measured cross sections at $\sqrt{s} = 7$ TeV are shown below. The combined mea-

Channel	Event selection efficiency [%]
e+jets	1.42 ± 0.02
μ+jets	2.15 ± 0.02
Combined	3.57 ± 0.03

Table 7.11: The event selection efficiencies for the muon, electron and combined channels as measured on the signal $t\bar{t}$ sample [1].

surement is obtained by the sum of the event yields in both channels:

$$\sigma_{t\bar{t}}^{e\text{+jets}} = 167 \pm 3\,(\text{stat.}) \pm 20\,(\text{syst.}) \pm 3\,(\text{lumi.})\,\text{pb} \tag{7.13}$$

$$\sigma_{t\bar{t}}^{\mu\text{+jets}} = 164 \pm 2\,(\text{stat.}) \pm 17\,(\text{syst.}) \pm 3\,(\text{lumi.})\,\text{pb} \tag{7.14}$$

$$\sigma_{t\bar{t}} = 165 \pm 2\,(\text{stat.}) \pm 17\,(\text{syst.}) \pm 3\,(\text{lumi.})\,\text{pb} \tag{7.15}$$

The two channels appear to be in agreement with each other. No excess of events is observed and the combined cross section is in good agreement with the latest theoretical SM cross section at $\sigma_{t\bar{t}} = 158\ ^{+\,13.5}_{-\,12.2}$ pb. The result is also in agreement within uncertainty with other ATLAS measurements made with different methods. These results, including the one obtained in this analysis, are summarized in Figure 3.7.

Chapter 8

Muon identification in a boosted $t\bar{t}$ environment

The search for BSM theories is an important part of particle physics research. Many of these theories posit the existence of very heavy particles that can only be produced by very energetic collisions. The LHC provides a unique opportunity to produce such collisions and search for very heavy particles.

Several BSM theories predict the existence of high mass particles that can decay into top quark pairs. An example of such a theory is the topcolor assisted technicolor model (TC2) [13, 14, 15] which predicts the existence of a leptophobic Z' boson. The Z' could potentially have a mass on the order of several TeV. Due to its large mass, the decay products of the Z' would emerge with a large momentum. These particles are said to be boosted particles.

One of the possible decay modes of the Z' is into a top quark pair. These would emerge with a very large momentum and decay into a W boson and a b quark in a collimated cone. In the detector, these events would appear as two back-to-back particle jets. The hadronic decay of the W would produce three jets which merge into a singular *fat jet*. If the W decays leptonically, the lepton is expected to lie very close to or within the b-jet. This makes reconstruction of such objects more difficult and requires specialized techniques, particularly when dealing with multiple merged jets. In contrast, low boost events where all products are well separated are said to be resolved.

Presented here are the results of a study conducted to determine the viability of using

the χ^2_{match} tagger to tag W muons from boosted top quark decays. This is in contrast to the cross section analysis detailed in a previous chapter where the muon tagged came from the semileptonic decay of b-quarks.

The boost of the top quarks is expected to be related to the mass of the Z' produced, so a higher mass Z' would decay into more collimated jets. The environment that results is thus very similar to that of a semileptonic b-decay: a muon buried inside a b-jet.

Searches for heavy bosons have been carried out and so far no evidence for such a resonance has been observed, and limits have been placed on the production rate of these resonance for various benchmark models. A leptophobic topcolor Z' of mass less than $1.74\,\text{TeV}$ has been excluded using $4.7\,\text{fb}^{-1}$ of ATLAS collision data at $\sqrt{s} = 7\,\text{TeV}$ [49] using both resolved and boosted reconstruction approaches. A more recent analysis using $14.3\,\text{fb}^{-1}$ of $\sqrt{s} = 8\,\text{TeV}$ data excluded a Z' with a mass less than $1.8\,\text{TeV}$ at $95\,\%$ confidence level [104] with the same combined reconstruction approach. The analysis detailed here is based on the 7 TeV analysis. Similar analyses performed with data collected by CMS using both a resolved and boosted reconstruction have excluded Z' candidates for similar benchmark models [105, 106, 107].

As the boost increases, the nominal isolation requirements used in the resolved $t\bar{t}$ analysis, namely cuts on $E_{\text{T}}^{\text{cone}\Delta R}$ and/or $p_{\text{T}}^{\text{cone}\Delta R}$ with a predefined cone size, begin to remove too many leptons. This results in very low lepton selection efficiency and poor acceptance in the higher mass range. As a result, much effort has gone into adapting the isolation requirements to boosted events.

The χ^2_{match} tagger could serve as a replacement for the traditional isolation requirements, or as a complement to other methodologies. A novel approach known as mini-isolation (MI) was developed by the ATLAS $t\bar{t}$ resonance group.

The results of a preliminary study of the efficiency of both of these methodologies are presented. In addition, the χ^2_{match} tagger performance as a b-tagger in boosted $t\bar{t}$ events is compared to the nominal approach that relies on the standard MV1 tagger. This study focuses on top pair production in the lepton plus jets channel.

8.1 Data samples

The simulated data used in this analysis is generated using $\sqrt{s} = 7\,\text{TeV}$ with 2011 data conditions. Signal Z' samples were generated at various mass points: 1.0, 1.3, 1.6, 2.0, 2.5 and 3.0 TeV. All simulated samples were generated using PYTHIA [92] with CTEQ6LI [108] PDF sets with a Z' width of 3 % of the boson mass. The irreducible $t\bar{t}$ background events are generated with MC@NLO v4.01 [86, 87] interfaced to HERWIG [88] for parton showering and hadronization, and JIMMY [89] for underlying event simulation.

The analysis is based on the truth information created by the event generator. This includes the kinematic information of particles in the event, as well as the child-parent connection between particles. For example, the Z' has two daughter particles associated with it: the top and antitop, which are in turn connected to the W bosons and b-quarks. By navigating up or down these chains it is possible to ascertain the origin of a given particle.

8.2 Boosted event topology

In order to perform an effective feasibility study it is important to understand how a boosted event looks in the detector. It is expected that events with more strongly boosted tops would exhibit a stronger collimation between the W muon and the b-quark. This results in a situation very similar to that exploited for b-tagging in Section 7; a muon from the semileptonic decay of a b-quark emerges from within the b-jet as shown in Figure 8.1. It is possible then to use the χ^2_{match} tagger[1] to tag W muons in boosted events. As the tagger is designed to work in energetically "busy" sectors of the detector, it is ideally suited to probe highly boosted events where the decay products are collimated.

As can be seen from Figure 8.2, the increase in boost does result in the W muon and b-quark emerging closer to each other. Note that the fraction of events below the χ^2_{match} tagger requirement of $\Delta R^{\text{jet}}_{\mu} < 0.5$ increases with top quark p_{T}. Additionally, as can be seen in Figure 8.3 the top p_{T} distribution peaks at just below half of the mass of the Z' boson, thus the large portion of the candidate muons in the sample will pass the aforementioned separation requirement. The decay products of the boosted top quark appear to emerge primarily back to

[1] Since signal muons in this analysis have large p_{T}, the tagger is now referred to as the χ^2_{match} tagger not soft muon tagger to reflect this difference

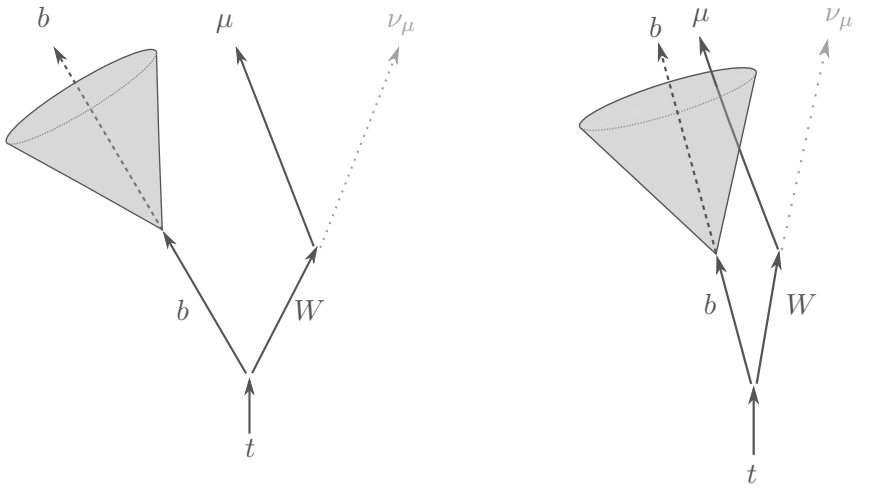

(a) Resolved top quark topology **(b)** Boosted top quark topology

Figure 8.1: Diagrams of possible configurations of final-state objects in (a) a resolved and (b) a boosted event.

back as seen in Figure 8.4, while the b-quarks from non-resonant $t\bar{t}$ emerge closer more often.

8.3 Signal muon selection

Since the signal muon in boosted $t\bar{t}$ events emerge near or within jets, the standard isolation requirements used in SM $t\bar{t}$ analyses erroneously remove W muons. The portion of muons removed increases with collimation and thus Z' mass. Using the nominal isolation requirement then limits the reach to higher Z' masses that have yet to be probed.

The ATLAS boosted $t\bar{t}$ resonance analysis proposed an alternative variable to replace the nominal isolation requirement called *mini-isolation* (MI). The absolute MI is defined as the sum of the measured transverse momenta of all tracks in a cone of size $\Delta R = k_{\mathrm{T}}/p_{\mathrm{T}}^{\ell}$ around the lepton, where k_{T} is an adjustable scale[2] and p_{T}^{ℓ} is the momentum of the lepton. This study uses the *relative* MI where the absolute value is scaled by the momentum of the lepton:

$$\text{Rel. MI} = \frac{MI}{p_{\mathrm{T}}^{\ell}} \tag{8.1}$$

where p_{T}^{ℓ} is the transverse momentum of the lepton.

MI adapts to the strong collimation of the top products with increasing boost by shrinking

[2]For convenience, mini-isolation with a k_{T} value of 10 GeV is referred to as MI10.

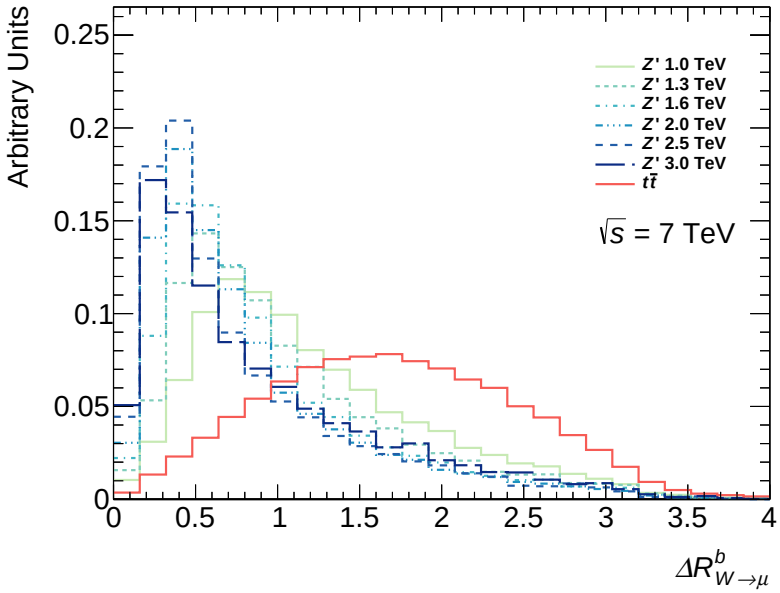

Figure 8.2: The angular separation (ΔR) between the truth W muon and the corresponding b-quark for all examined Z' mass points and non-resonant $t\bar{t}$. Uncertainties are omitted for clarity.

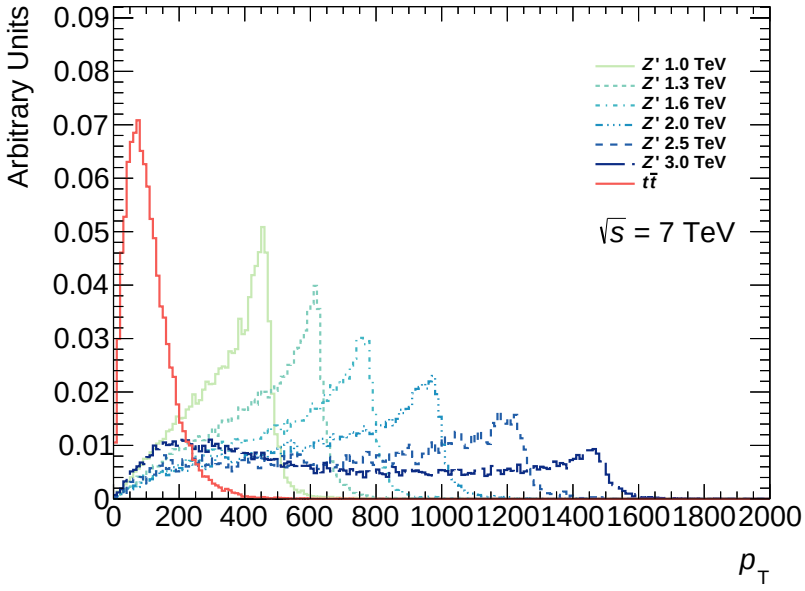

Figure 8.3: The transverse momentum of the top/anti-top quarks in the event for all examined Z' mass points and non-resonant $t\bar{t}$. Uncertainties are omitted for clarity.

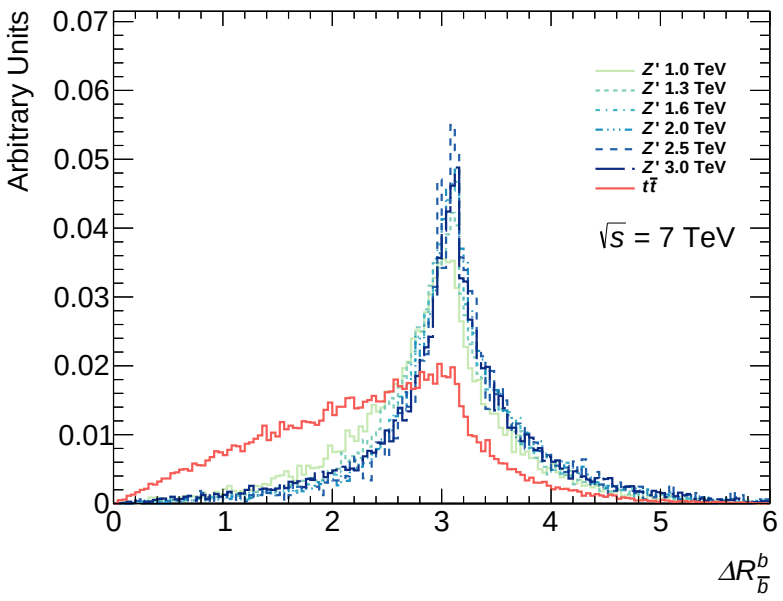

Figure 8.4: The angular separation (ΔR) between the b and $\bar{b}$ in the event for all examined Z' mass points and non-resonant $t\bar{t}$. Uncertainties are omitted for clarity.

the size of the cone for higher boost top quarks.

The goal of this study is to improve the acceptance at higher Z' masses by removing the nominal isolation requirement, and instead use the χ^2_{match} tagger to identify the signal muons.

The performance of the χ^2_{match} tagger is measured against the conventional isolation criteria, and MI with $k_{\text{T}} = 10\,\text{GeV}$. The resolved isolation criteria requires the muon to have an $E_{\text{T}}^{\text{cone20}} < 2.5\,\text{GeV}$ and $E_{\text{T}}^{\text{cone30}} < 4.0\,\text{GeV}$. For mini-isolation, the lepton is deemed isolated if the $\sum p_{\text{T}}$ is less than 5 % of the lepton p_{T}. The χ^2_{match} tagger operates with the same selection used in Chapter 6 with the standard operating-point of $\chi^2_{\text{DoF}} < 3.2$.

Two separate selections are applied: one for χ^2_{match} tagger and one for the resolved isolation and mini-isolation. As mini-isolation and the resolved isolation both use MUID, they share the same set of reconstruction criteria, while the χ^2_{match} tagger selection is moderately different. All chains require a high-p_{T} muon ($p_{\text{T}} > 20\,\text{GeV}$) within the pseudorapidity coverage of the ID ($|\eta| < 2.5$) that passes the MCP tracking cuts detailed in Appendix E. Mini-isolation and resolved isolation make use of muons reconstructed by the MUID algorithm that pass the so-called *Tight* identification criteria. An additional requirement on the impact parameter ($|z_0| < 3.0\,\text{mm}$) is used to reduce non-prompt muons. The χ^2_{match} tagger uses the STACO combined algorithm for muon reconstruction with no additional requirements. The cutflows

for all three selections are shown in Figure 8.7.

The distribution of pseudorapidity for χ^2_{match} tagged muons, as expected, is similar for all $m_{Z'}$ samples as shown in Figure 8.5b. Interestingly, in Figure 8.5a, the average transverse momentum of the χ^2_{match} muon increases with $m_{Z'}$ up to $1.6\,\text{TeV}$ then stabilizes for higher masses. This suggests that the b-quark takes a larger portion of the top quark momentum above a certain threshold. As expected the angular separation between the χ^2_{match} tagged muon and the jet in the event decreases with increased $m_{Z'}$ as shown in Figure 8.5c. Finally, the χ^2_{DoF} distribution is not affected by changes in $m_{Z'}$ as shown in Figure 8.5d. Thus the efficiency of the χ^2_{match} tagger should be stable through-out the mass range. Similar comments can be made about MI10 muons with regards to their transverse momentum (Figure 8.6a), pseudorapidity (Figure 8.6b) and angular separation from the nearest jet (Figure 8.6c). The size of the cone used in MI is inversely proportional to the lepton p_{T}. As expected, the cone size distributions are much wider with longer tails at low $m_{Z'}$ and more narrow at high $m_{Z'}$ as shown in Figure 8.6d.

8.4 Efficiency definition

The efficiency measurement was designed to provide an accurate representation of the performance of the χ^2_{match} tagger and a fair comparison with mini-isolation. Additional sources of inefficiency such as muon reconstruction are separated out into an additional efficiency which is also quoted. See Figure 8.7 for a summary of the efficiency measurement.

Firstly, events where a W boson decays into a muon are selected using truth information. These events are then used to measure the efficiency. Note that at each stage the denominator is the numerator of the previous efficiency. Thus the complete efficiency is given by the product of all the efficiency components. This allows for an estimation of the number of W muons that would be selected.

First, the truth W muons are matched to STACO/MUID muons if the angular separation (ΔR) between them is less than 0.0015. The matching efficiency is defined as:

$$\epsilon_{\text{match}} = \frac{\text{STACO/MUID muons matched to truth } W \text{ muon}}{\text{Truth } W \text{ muons}} \tag{8.2}$$

The selections then diverge and the two sets of reconstruction cuts described earlier are applied independently with an efficiency defined as:

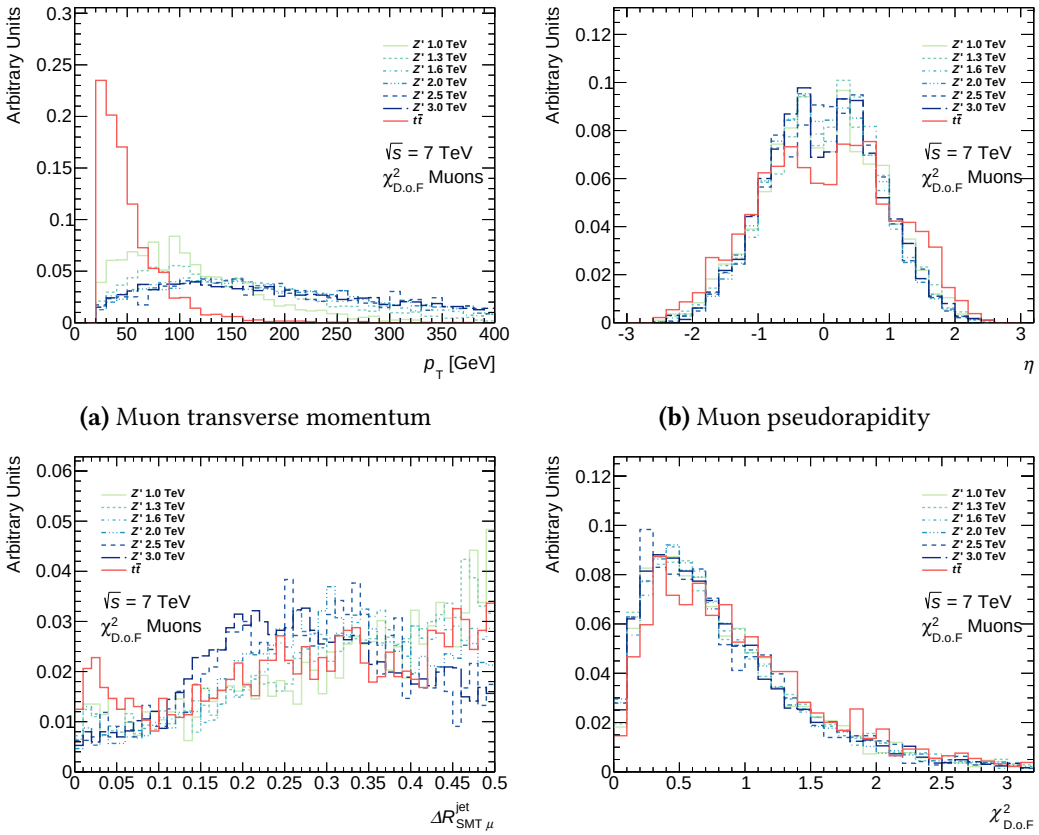

(a) Muon transverse momentum

(b) Muon pseudorapidity

(c) Angular separation from nearest jet

(d) STACO combined χ^2_{DoF}

Figure 8.5: Distributions for all tested Z' mass points of (a) the transverse momentum and (b) pseudorapidity of muons which pass the χ^2_{match} tagger selection, the (c) angular separation between those muons and the nearest jet in the event, and (d) the χ^2_{match} used in the selection. All distributions normalized to unit area.

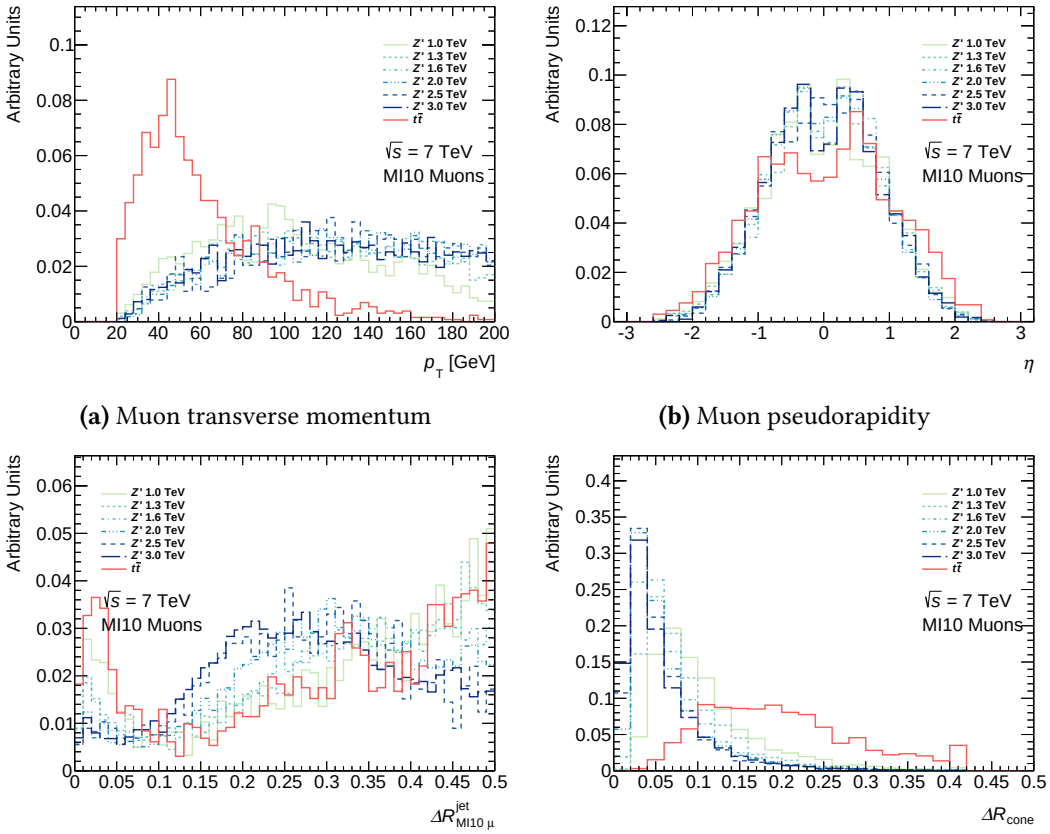

(a) Muon transverse momentum

(b) Muon pseudorapidity

(c) Angular separation from nearest jet

(d) Size of isolation cone

Figure 8.6: Distributions for all tested Z' mass points of (a) the transverse momentum and (b) pseudorapidity of muons which pass the MI10 selection, the (c) angular separation between those muons and the nearest jet in the event, and (d) the cone size used in the selection. All distributions normalized to unit area.

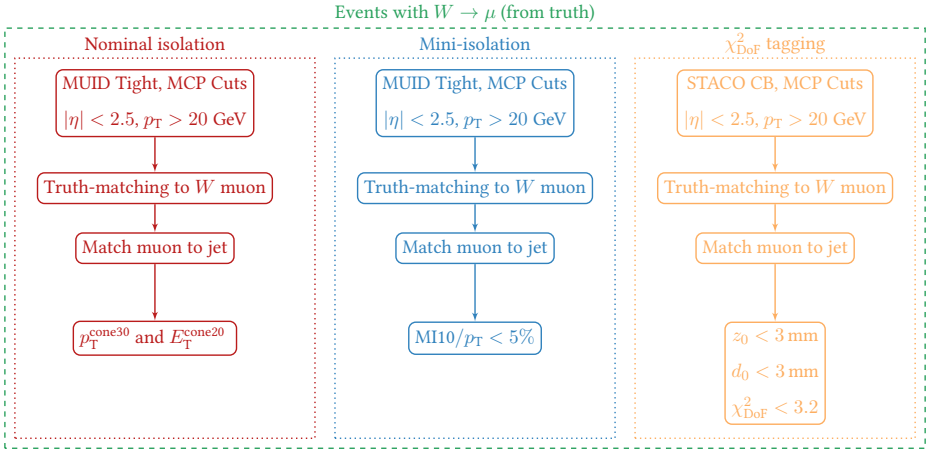

Figure 8.7: Structure of the efficiency measurement including both cut-flows.

$$\epsilon_{\text{reco}} = \frac{\text{STACO/MUID muons that pass reconstruction cuts}}{\text{STACO/MUID muons matched to truth } W \text{ muon}} \tag{8.3}$$

Next the muons are required to be within $\Delta R < 0.5$ from a jet. The impetus behind the analysis is to probe highly boosted events exploiting the capabilities of χ^2_{match} tagging. This selection ensures that the muons available for χ^2_{match} tagging are indeed close to a jet. This selection also has an efficiency associated with it defined as:

$$\epsilon_{\text{non-iso}} = \frac{\text{Muons with } \Delta R^{\text{jet}}_{\mu} < 0.5}{\text{STACO/MUID muons that pass reconstruction cuts}} \tag{8.4}$$

The final step is the application of either the mini-isolation selection or the χ^2_{match} tagger selection discussed above. These selections are associated with the final and most interesting sets of efficiencies, defined as:

$$\epsilon_{\chi^2_{\text{match}}/\text{MI10/Res.}} = \frac{\text{Muons which pass } \chi^2_{\text{match}}/\text{MI10/Res. selection}}{\text{Muons with } \Delta R^{\text{jet}}_{\mu} < 0.5} \tag{8.5}$$

In the nominal analysis described in [49] muons which are within $\Delta R = 0.1$ of the jet would be removed. The goal of the analysis is to exploit the χ^2_{match} tagger to accept additional events where the signal muon emerges very close to the jet axis, thus overlap removal [3] is not traditionally part of the χ^2_{match} tagging selection. Two sets of efficiencies are provided here: one without overlap (defined in Eq 8.5) and one with overlap removal, defined below

$$\epsilon_{\chi^2_{\text{match}}/\text{MI10/Res.+overlap}} = \frac{\text{Muons which pass the } \chi^2_{\text{match}}/\text{MI10/Res. selection with } \Delta R^{\text{jet}}_{\mu} > 0.1}{\text{Muons with } \Delta R^{\text{jet}}_{\mu} < 0.5} \tag{8.6}$$

8.5 Results

The results of the reconstruction portion of the analysis chains are summarized in Table 8.1 for the χ^2_{match} chain and in Table 8.2 for the mini-isolation chain. The matching efficiency (ϵ_{match}) is stable with respect to Z' mass for both MUID and STACO, meaning that both algorithms

[3] True objects may be reconstructed as two different objects, such as an electron and jet. Overlap removal is the act of selecting the true object from two overlapping reconstructed objects.

are able to reconstruct the signal muon irrespective of boost. Within the uncertainty neither algorithm appears to be better than other at reconstruction of these muons. The efficiencies of both reconstruction selections (ϵ_{reco}) are compatible within uncertainties and appear to be slightly lower at low Z' mass, likely due to the p_{T} requirement on the muon. Finally, the collimation effect due to increased boost is clearly visible in the non-isolation efficiency. A marked increase with Z' mass is noted as the products of the top quarks get pushed closer together. Note that the results obtained at $m_{Z'} = 2.5\,\text{TeV}$ suffer from lack of data compared to the other mass points. Once again, this effect those not appear to affect one reconstruction algorithm more than the other and the efficiencies are compatible within uncertainty.

$m_{Z'}$ [GeV]	$N_{\text{muons}}^{\text{from } W}$	Efficiency [%]		
		$\epsilon_{\text{match}}^{\text{STACO}}$	$\epsilon_{\text{reco}}^{\text{STACO}}$	$\epsilon_{\text{non-iso.}}^{\text{STACO}}$
1000	13 700	91.3 ± 0.2	85.5 ± 0.3	20.4 ± 0.4
1300	15 500	92.0 ± 0.2	86.4 ± 0.3	31.8 ± 0.4
1600	13 400	91.9 ± 0.2	87.5 ± 0.3	42.4 ± 0.5
2000	15 300	92.1 ± 0.2	87.9 ± 0.3	51.3 ± 0.5
2500	3310	91.9 ± 0.5	88.1 ± 0.6	57.7 ± 1.0
3000	15 300	91.8 ± 0.2	87.5 ± 0.3	51.4 ± 0.5

Table 8.1: Results of constructing the muon sample used to estimate the efficiency of the χ^2_{match} tagger. Uncertainty is statistical only.

$m_{Z'}$ [GeV]	$N_{\text{muons}}^{\text{from } W}$	Efficiency [%]		
		$\epsilon_{\text{match}}^{\text{MUID}}$	$\epsilon_{\text{reco}}^{\text{MUID}}$	$\epsilon_{\text{non-iso}}^{\text{MUID}}$
1000	13 700	91.7 ± 0.2	86.6 ± 0.3	20.3 ± 0.4
1300	15 500	92.2 ± 0.2	87.6 ± 0.3	31.9 ± 0.4
1600	13 400	92.2 ± 0.2	88.7 ± 0.3	42.2 ± 0.5
2000	15 300	92.5 ± 0.2	88.8 ± 0.3	51.2 ± 0.4
2500	3310	92.2 ± 0.5	89.1 ± 0.7	57.9 ± 0.9
3000	15 300	92.1 ± 0.2	88.5 ± 0.3	51.2 ± 0.4

Table 8.2: Results of constructing the muon sample used to estimate the efficiency of mini-isolation and resolved isolation. The uncertainty is statistical only.

The efficiency of the resolved isolation is low and decreases with increasing boost to 18 % at

$m_{Z'} = 3.0\,\text{TeV}$ as shown in Table 8.3, highlighting the need for a better isolation requirement.

$m_{Z'}$ [GeV]	Efficiency [%]	
	$\epsilon_{\text{Res.}}$	$\epsilon_{\text{Res.+overlap}}$
1000	43.7 ± 1.1	35.5 ± 1.0
1300	38.5 ± 0.8	33.2 ± 0.7
1600	33.4 ± 0.7	29.4 ± 0.7
2000	26.7 ± 0.6	24.1 ± 0.5
2500	21.6 ± 1.0	19.5 ± 1.0
3000	20.8 ± 0.5	18.6 ± 0.5

Table 8.3: Efficiency of selecting a muon by using the resolved isolation. Uncertainty is statistical only.

The performance of MI and the χ^2_{match} tagger was studied as a function of the angular separation between the muon and the jet (Figure 8.8), and the p_{T} of the muon (Figure 8.9). The χ^2_{match} tagger efficiency shows some minor dependence on the angular separation to the jet and as expected exhibits a dependence on the p_{T} of the muon. Mini-isolation has a strong dependence on the p_{T} of the muon particularly in the low range. The efficiency at high p_{T} plateaus at approximately $100\,\%$, due to the mini-isolation cone containing only the muon itself. The decrease in efficiency at lower momentum is due to the increase in the cone size and the inclusion of more tracks from the nearby jet in the cone. Note that the cone size is larger than the one used for the nominal analysis for muons with $p_{\text{T}} < 50\,\text{GeV}$. The mini-isolation efficiency distribution exhibits a strong dependence on $\Delta R_{\mu}^{\text{jet}}$ which varies as a function of top boost in the event.

This effect was stronger before the introduction of truth matching to the analysis. A possible explanation for the dip was due to the background rejection capability of mini-isolation. Muons which are very close to jets most likely come from semileptonic decay of b-quarks. These should be rejected as they do not come from the W boson. Despite this correction the effect persists. It is possible that the reconstructed muon is being mismatched to the W muon. The matching criteria was tightened to $\Delta R < 0.001$ in an attempt to reduce the likelihood of muon mismatching. This had a negligible effect on the shape of the MI distribution. As expected changing the value of k_{T} does change the shape of the distribution, but does not remove

the dip.

An examination of the MI10 cone-size points to the explanation: low-p_{T} muons will result in a larger cone with a maximum size of $\Delta R = 0.4$, if these happen to lie near to the jet they are very likely to be rejected. The non-resonant $t\bar{t}$ distribution exhibits a wider and lower dip in the efficiency. In other words the distance between the jet and the muon do not scale linearly with the muon p_{T} hence at lower boost the jet cone and the muon cone overlap significantly.

The χ^2_{match} tagger efficiency is very high and fairly stable with Z' mass as shown in Table 8.4. The inclusion of the overlap removal decreases the efficiency by approximately 7 %–10 % depending on the mass point examined. In comparison, the mini-isolation efficiency is lower across the mass range, with and without overlap, but only by 2 %–10 % depending on the mass point examined. Crucially, the efficiency of both taggers at higher Z' masses are very similar. This means that the gains in acceptance provided by χ^2_{match} is small in the $m_{Z'}$ that has yet to be experimentally excluded. Also note that both methodologies have a higher efficiency than the resolved isolation shown in Table 8.3.

$m_{Z'}$ [GeV]	Efficiency [%]			
	$\epsilon_{\chi^2_{\mathrm{match}}}$	ϵ_{MI10}	$\epsilon_{\chi^2_{\mathrm{match}}+\mathrm{overlap}}$	$\epsilon_{\mathrm{MI10+overlap}}$
1000	94.5 ± 0.5	83.1 ± 0.8	80.4 ± 0.8	70.2 ± 1.0
1300	95.7 ± 0.3	89.0 ± 0.5	84.9 ± 0.6	79.4 ± 0.6
1600	95.7 ± 0.3	90.9 ± 0.4	85.8 ± 0.5	82.1 ± 0.6
2000	96.0 ± 0.3	92.0 ± 0.3	87.8 ± 0.4	85.5 ± 0.4
2500	96.2 ± 0.5	92.4 ± 0.7	87.1 ± 0.9	85.1 ± 0.9
3000	96.3 ± 0.2	92.5 ± 0.3	87.6 ± 0.4	85.1 ± 0.4

Table 8.4: Efficiency of selecting a muon by using the χ^2_{match} tagger against MI, including the additional acceptance provided by the χ^2_{match} tagger. Uncertainty is statistical only.

8.5.1 Background

A preliminary estimation of the fake-rate for the χ^2_{match} tagger and mini-isolation in a boosted environment was carried out.

The dominant backgrounds for boosted $t\bar{t}$ events include multijet events and SM resolved $t\bar{t}$. A measure of the acceptance of multijet background is provided here.

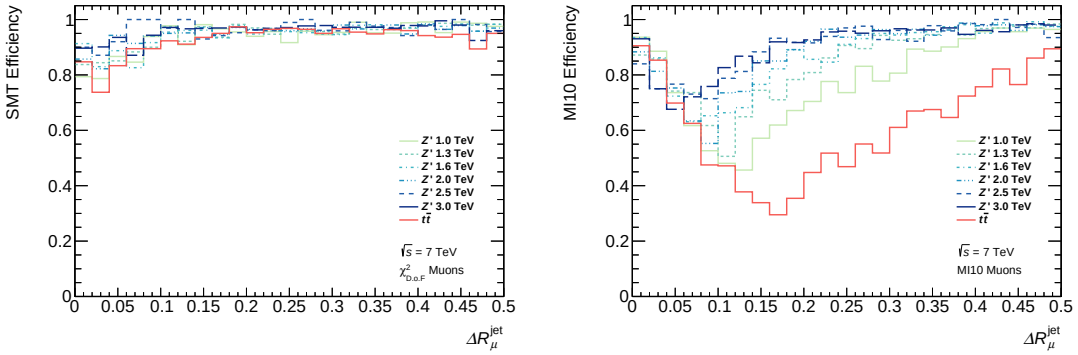

(a) χ^2_{match} muon tagger **(b)** MI10

Figure 8.8: Efficiency of MI10 and χ^2_{match} tagger as a function of the angular separation between the reconstructed muon and the nearest reconstructed jet. Uncertainties are omitted for clarity. The dip in the MI efficiency at low ΔR is removed in the nominal analysis by cutting at $\Delta R < 0.1$

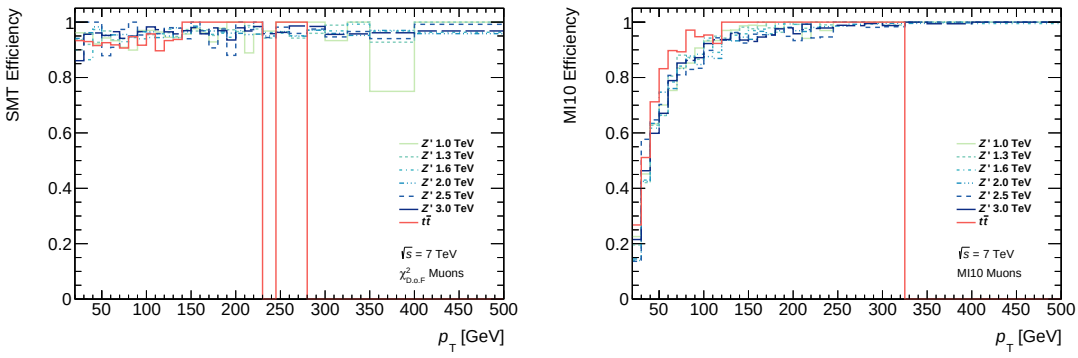

(a) χ^2_{match} muon tagger **(b)** MI10

Figure 8.9: Efficiency of MI10 and the χ^2_{match} muon tagger as a function of the transverse momentum of the muon. Uncertainties are omitted for clarity. The missing bins are due to lack of data in that region of phase-space.

This source is normally estimated using complex data-driven methods, however as this is a preliminary study, a simulated sample of all-hadronic events is used instead. The all-hadronic sample is constructed by requiring that no truth W muons be present. These events do not perfectly represent the dominant multijet sources such as $b\bar{b}$ production, but the lack of a signal W muon make these events a suitable preliminary substitute.

The lack of an isolation requirement is expected to result in a substantial increase in the amount of background selected. Soft muons from the semileptonic decay of HF quarks will also be selected, this then increases acceptance to $b\bar{b}$ events.

The same efficiency definitions described in Section 8.4 are used here. No truth-matching is carried out here due to the lack of a W muon, so only the χ^2_{match} tagger and mini-isolation fake rates are shown.

As expected, MI exhibits a low fake rate while maintaining very high signal efficiency (Table 8.5) with or without overlap removal. In comparison, removing the isolation requirement entirely greatly increases the background acceptance when using the χ^2_{match} tagger. Introducing overlap removal does reduce the background substantially for both selections but χ^2_{match} fake rate remains above 20 %.

The increase in signal acceptance does not make this methodology sufficiently advantageous, particularly when considering the large increase in fake rate. An examination of the b-tagging potential of the χ^2_{match} tagger is presented in the next section.

$m_{Z'}$ [GeV]	Fake rate [%]			
	$\epsilon_{\chi^2_{\text{match}}}$	ϵ_{MI10}	$\epsilon_{\chi^2_{\text{match}}\text{+overlap}}$	$\epsilon_{\text{MI10+overlap}}$
1000	92.8 ± 0.3	4.1 ± 0.2	20.8 ± 0.5	2.4 ± 0.2
1300	92.4 ± 0.3	4.8 ± 0.2	28.9 ± 0.5	3.7 ± 0.2
1600	91.6 ± 0.3	5.5 ± 0.2	36.9 ± 0.5	4.5 ± 0.2
2000	91.1 ± 0.3	7.1 ± 0.2	45.5 ± 0.5	6.1 ± 0.2
2500	90.1 ± 0.6	6.4 ± 0.5	48.7 ± 1.1	5.6 ± 0.5
3000	90.1 ± 0.3	6.6 ± 0.2	46.1 ± 0.5	5.7 ± 0.2

Table 8.5: Fake rate of the χ^2_{match} tagger and mini-isolation with and without overlap removal as measured using all Z' mass points. The uncertainty is statistical only.

$m_{Z'}$ [GeV]	Number of b-quarks from top		$\epsilon_{b \text{ to jet}}$ [%]
	In the event	Matched to a jet	
1000	160 000	133 000	83.5 ± 0.1
1300	180 000	155 000	85.9 ± 0.1
1600	160 000	140 000	87.0 ± 0.1
2000	180 000	158 000	87.9 ± 0.1
2500	40 000	35 200	88.0 ± 0.2
3000	180 000	156 000	86.8 ± 0.1

Table 8.6: Summary of b-quark to jet matching efficiencies for all tested Z' masses. The uncertainty is statistical only.

8.6 B-tagging potential in boosted events

A study of the b-tagging performance of the SMT tagger was carried out and is presented here along with a comparison against the nominal MV1 tagger. The performance is estimated in simulation using the Z' samples described earlier. Using truth information, the b-quarks from the top decays are identified and then matched to reconstructed anti-k_t jets of cone-size $\Delta R = 0.4$. The matching is done by requiring the jet and b-quark lie within $\Delta R_b^{\text{jet}} < 0.3$ of each other. The value of the ΔR used here is a standard used at ATLAS for the purpose of flavour tagging of jets from simulated data. These matched jets then tentatively form a pool of jets on which the tagging performance can be measured. This matching procedure has an efficiency associated with it defined as

$$\epsilon_{b \text{ to jet}} = \frac{b \text{ quarks with } \Delta R_{\text{jet}}^{b} < 0.3}{b \text{ quarks from } t \to Wb} \tag{8.7}$$

The matching efficiency remains above $80\,\%$ through-out the tested mass range (Table 8.6), and there appears to be a trend of increasing matching efficiency with mass range.

The tagging efficiency can be defined in two ways. The first folds the effect of the low $b \to \mu$ branching ratio into the final efficiency. This makes the comparison with other taggers possible and is denoted by $\epsilon_{\text{Inc. SMT}}$.

The second definition separates the efficiency into two components: firstly, the jet is associated with a STACO combined muon by requiring $\Delta R_{\text{jet}}^{\mu} < 0.5$. The associated efficiency

defined as,

$$\epsilon_{\mu\text{-match}} = \frac{\text{Number of } b\text{-jets with an associated muon}}{\text{Number of } b\text{-jets}} \tag{8.8}$$

and then both the muon and the jet are required to pass the SMT tagger selection. This step has an associated efficiency:

$$\epsilon_{\text{SMT}} = \frac{\text{Number of jets/muons that pass the } \chi^2_{\text{match}} \text{ tagger selection}}{\text{Number of } b\text{-jets with an associated muon}} \tag{8.9}$$

The second definition provides a more apt description of the performance of the SMT tagger but makes comparisons with other taggers incorrect. The former definition of the efficiency is used here to allow for a proper comparison between the MV1 and SMT taggers.

As expected, as the boost increases the distance between the muon and the jet decreases as shown in Table 8.7. This leads to an increase in the muon-to-jet matching efficiency.

$m_{Z'}$ [GeV]	Jets matched to muon	$\epsilon_{\mu\text{-match}}$ [%]
1000	$22\,100 \pm 100$	17.1 ± 0.3
1300	$28\,400 \pm 200$	18.2 ± 0.2
1600	$27\,600 \pm 200$	20.4 ± 0.2
2000	$33\,500 \pm 200$	20.7 ± 0.2
2500	7540 ± 90	21.2 ± 0.5
3000	$32\,800 \pm 200$	21.5 ± 0.2

Table 8.7: Results of the muon to jet association in MC simulated inclusive Z' samples.

The tagging yields as well as the overlap yield between the taggers are shown in Table 8.8. As expected the MV1 tagger selects the vast majority of the b-jets while the effect of the semileptonic b-decay is also noted in the lower SMT yields.

The SMT tagging efficiency appears to increase with $m_{Z'}$ as shown in Table 8.9. Interestingly, the performance of the MV1 tagger degrades substantially with increasing $m_{Z'}$ mass. Also note that the overlap between the MV1 tagger and the SMT tagger decreases with $m_{Z'}$. This means that using the SMT tagger alongside the MV1 tagger can provide substantial increases in yields at higher Z' masses.

The efficiency for both taggers as a function of the jet p_{T} is shown in Figure 8.10. The performance of the MV1 tagger is clearly p_{T} dependant while the SMT tagger is more stable

$m_{Z'}$ [GeV]	Number of jets tagged by		
	SMT	MV1	Both
1000	$19\,600 \pm 100$	$96\,900 \pm 300$	$14\,800 \pm 100$
1300	$25\,000 \pm 200$	$109\,000 \pm 300$	$18\,100 \pm 100$
1600	$23\,900 \pm 200$	$93\,100 \pm 300$	$16\,300 \pm 100$
2000	$28\,300 \pm 200$	$96\,200 \pm 300$	$17\,800 \pm 100$
2500	6250 ± 80	$19\,800 \pm 100$	3690 ± 60
3000	$27\,200 \pm 200$	$89\,400 \pm 300$	$16\,200 \pm 100$

Table 8.8: Results of the b-jet tagging study. Shown are the number of jets tagged by the SMT tagger, the MV1 tagger, and both. These jets have been truth-matched to b-quarks.

$m_{Z'}$ [GeV]	ϵ_{SMT} [%]	ϵ_{MV1} [%]	Overlap [%]	Added Acceptance [%]
1000	14.7 ± 0.1	72.7 ± 0.1	75.3 ± 0.1	5
1300	16.2 ± 0.1	70.7 ± 0.1	72.4 ± 0.1	6
1600	17.2 ± 0.1	66.9 ± 0.1	68.0 ± 0.1	8
2000	17.9 ± 0.1	60.9 ± 0.1	63.0 ± 0.1	11
2500	17.8 ± 0.2	56.3 ± 0.2	59.0 ± 0.2	13
3000	17.4 ± 0.1	57.3 ± 0.1	60.0 ± 0.1	12

Table 8.9: Results of the b-tagging efficiency estimation for the MV1 and SMT taggers. The amount of overlap is shown out of the SMT tagged jets, while the added acceptance is measured as the number of jets tagged only by SMT over the number of MV1 tagged jets. The uncertainties are statistical only.

with respect to jet p_{T}. The performance of the MV1 tagger is lower at both extremes of the momentum distribution. At low jet p_{T} the performance of secondary vertex reconstruction is degraded due to the lower decay length. In contrast, at high jet p_{T} the primary source of b-tagging efficiency loss comes from the shift in the jet axis away from the the B-hadron direction. If the shift is very large, some of the B-hadron components may not be associated with the jet and not enter into the discriminants that make up the MV1 tagger [109].

The performance of the SMT tagger in a boosted environment looks promising from this preliminary study, however a more careful measurement of the performance needs to be conducted. In addition, it is important to also perform a fake-rate study in such a boosted environment. As was observed in the calibration of the tagger on both 2012 and 2011 data, the efficiency of tagging a soft muon is not affected by the isolation of that muon.

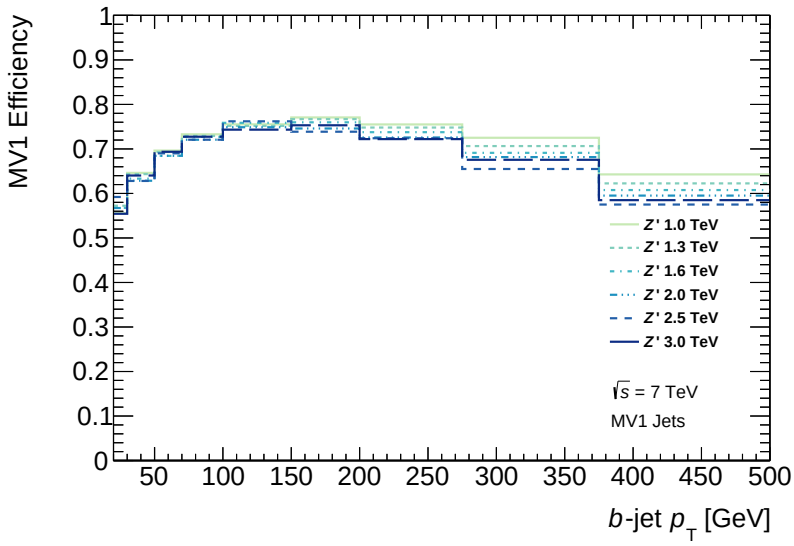

(a) MV1 Tagger

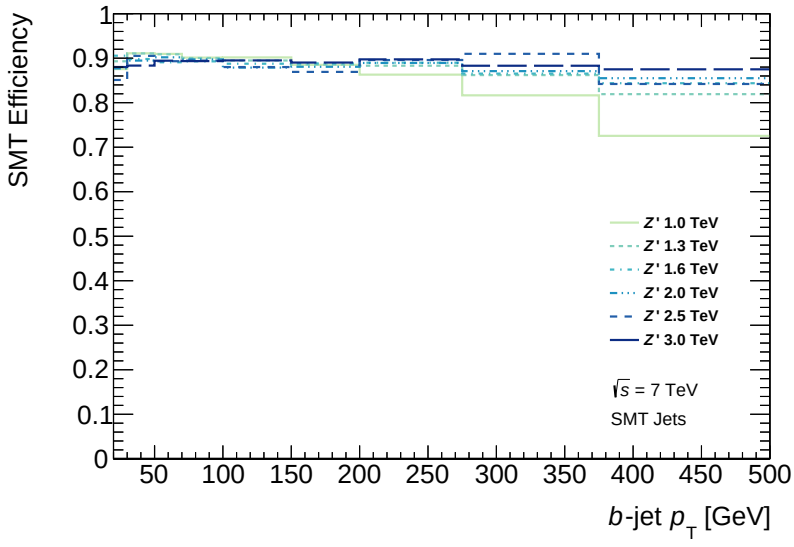

(b) SMT Tagger

Figure 8.10: The b-tagging efficiency distributions as a function of jet p_{T} for the MV1 tagger and the SMT tagger as measured in all Z' mass points.

Chapter 9

Conclusions

This thesis explored alternative method for b-tagging and muon selection known as the χ^2_{match}-based soft muon tagger. The SMT tagger exploits the quality of the match between the ID track and the MS track to tag soft muons produced in the decay of b-quarks. The tagger was calibrated on 2012 ATLAS data and used as part of two $t\bar{t}$ measurements. The first was the measurement of the SM $t\bar{t}$ production cross section in the lepton plus jets channel at $\sqrt{s} = 7\,\text{TeV}$ using the χ^2_{match}-based SMT tagger. The second tested the viability of using the χ^2_{match}-tagger in the realm of boosted $t\bar{t}$ searches at $\sqrt{s} = 8\,\text{TeV}$.

The calibration of the χ^2_{match}-based SMT tagger was carried out using low-p_{T} muons from J/ψ decays on 2012 ATLAS data at $\sqrt{s} = 8\,\text{TeV}$. A tag and probe method was used to construct a pool of muons on which to measure the efficiency of the SMT tagger. The efficiency of the tagger monitored as a function of the angular position, the isolation, and the transverse momentum of the candidate muons. No dependence was observed on the isolation of the muon, this makes the calibration on the isolated J/ψ muons applicable to $t\bar{t}$ events. No dependence was observed with respect to the azimuthal angle. As in the previous calibration, a dependence on the transverse momentum is observed, as well as a dependence on the pseudorapidity which is asymmetric between the positive and negative sides of the detector. The distribution of the STACO combined χ^2_{DoF} appears to be mismodelled in simulation compared to data. This results in a scale factor that deviates from unity by as much as 20 %. The discrepancy in χ^2_{DoF} appears to originate from a mismodelling of the transverse impact parameter or the correlated polar angle. The effects of the detector alignment description on the χ^2_{DoF} were noted. Differences

between the 2011 and 2012 simulation change the distribution significantly. A more thorough examination of the alignment effects needs to be conducted to determine if this is the source of the discrepancy.

The SM $t\bar{t}$ production cross section at $\sqrt{s} = 7\,\text{TeV}$ has been measured in the lepton plus jets channel using the χ^2_{match}-based SMT tagger. The multijet background component in the electron channel was measured using the matrix method and the ABCD method. The results of both methodologies are in agreement within their uncertainties. The cross section measured agrees with the latest theoretical predictions and results from other ATLAS and CMS measurements. The soft muon tagger contributes an uncertainty which is comparable to or smaller than other taggers used in other ATLAS $t\bar{t}$ cross section measurements.

The performance of the SMT tagger in a boosted environment has been measured in a preliminary study using only simulated data. Using the tagger to select muons from W bosons yielded some additional acceptance to the mini-isolation approach, however the increase in fake rate makes this methodology less advantageous, particularly since a dedicated treatment of the background would have to be devised.

The SMT tagger appears to function well as a b-tagger in a boosted environment. Using the SMT tagger alongside the MV1 yields an 10 % increase in the number of tagged b-jets compared to the MV1 tagger alone. If the uncertainties due to the tagger remain similar to those estimated in the SM $t\bar{t}$ cross section measurement, it would be possible to repeat the resonant $t\bar{t}$ search using the SMT tagger instead. This would require a more thorough examination of the data/MC discrepancy noted in the calibration, or the use of another variable in lieu of the χ^2_{DoF}. The latter is now being explored using the momentum imbalance which exhibits a similar performance and is better modelled in simulation.

Appendices

Appendix A

Electron identification criteria

Three sets of identification criteria are defined and labelled as loose, medium and tight [110]. The selection criteria include tracking, calorimeter and track-cluster variables as detailed below.

Category	Description	Variable
	Loose	
Acceptance	$\|\eta\| < 2.47$	
Hadronic leakage	In $\|\eta\| < 0.8$ and $\|\eta\| > 1.37$: ratio of E_{T} in the first layer of the hadronic calorimeter to E_{T} of the EM cluster	$R_{\mathrm{had,1}}$
	In $0.8 < \|\eta\| < 1.37$: ratio of E_{T} in whole hadronic calorimeter to E_{T} of the EM cluster	R_{had}
Middle layer of the EM	Ratio of energies in 3×7 cells over 7×7 cells	R_{η}
	Lateral width of the shower	$\omega_{\eta 2}$
Front layer of EM	Total shower width	ω_{stot}
	Energy difference of the largest and second largest energy deposits in the cluster divided by their sum	E_{ratio}
Track quality and track-cluster matching	Number of hits in the pixel detector (> 0)	
	Number of hits int he silicon detectors (≥ 7)	
	$\|\Delta\eta\|$ between the cluster position in the first layer and the extrapolated track (< 0.015)	$\Delta\eta_1$

Table A.1: Loose electron identification criteria.

Category	Description	Variable
	Medium	
Track quality and track-cluster matching	Number of hits in the b-layer > 0 for $\|\eta\| < 2.01$	
	Number of hits in the pixel detector > 1 for $\|\eta\| < 2.01$	
	Transverse impact parameter $\|d_0\| < 5\,\text{mm}$	d_0
	Tighter $\|\eta_1\|$ cut (< 0.005)	
TRT	Loose cut on TRT high-threshold fraction	

Table A.2: Medium electron identification criteria.

Category	Description	Variable
	Tight	
Track quality and track-cluster matching	Transverse impact parameter cut $\|d_0\| < 1\,\text{mm}$	
	Asymmetric cut on $\Delta\phi$ between the cluster position in the middle layer and the extrapolated track	$\Delta\phi$
	Ratio of the cluster energy to the track momentum	E/p
TRT	Total number of hits in the TRT	
	Tighter cut on the TRT high-threshold fraction	
Conversions	Reject electron candidates matched to reconstructed photon conversions	

Table A.3: Tight electron identification criteria.

Appendix B

Muon identification criteria

Muon identification criteria are defined for MUID are presented below:

- **Tight**:
  - Passes MUID Combined selection **OR**
  - MUID Standalone at $|\eta| > 2.5$ **AND** has atleast three MDT+CSC stations **OR**
  - MuGirl with extended track **AND** (at least two MDT+CSC stations **OR** less than six MDT+CSC holes on track)
- **Medium**:
  - Tight **OR**
  - MuGirl with extended track **OR** $|\eta| < 0.2$ **OR** has at least two muon track segments **OR**
  - MuTagIMO at $|\eta| < 0.2$ **OR** has at least two muon track segments
- **Loose**:
  - Medium **OR**
  - MuGirl **OR**
  - MuTagIMO **OR**
  - MuidStandalone

Appendix C

STACO Combined covariance matrix

The STACO CB covariance matrix encodes the uncertainty on each of the five track parameters (diagonal terms) as well as the correlation in the uncertainty between parameters (off-diagonal terms). Given the five track parameters:

$$\mathbf{T} = (d_0, z_0, \phi, \theta, q/p) \tag{C.1}$$

the covariance matrix is:

$$\mathbf{C}_{\text{MS/ID}} = \begin{pmatrix} \sigma^2(d_0) & cov(d_0, z_0) & cov(d_0, \phi) & cov(d_0, \theta) & cov(d_0, q/p) \\ . & \sigma^2(z_0) & cov(z_0, \phi) & cov(z_0, \theta) & cov(z_0, q/p) \\ . & . & \sigma^2(\phi) & cov(\phi, \theta) & cov(\phi, q/p) \\ . & . & . & \sigma^2(\theta) & cov(\theta, q/p) \\ . & . & . & . & \sigma^2(q/p) \end{pmatrix} \tag{C.2}$$

A covariance matrix is associated with each set of parameters, those measured in the inner detector, and those measured in the muon systems.

Appendix D

List of triggers used in calibration

The calibration analysis makes use of an OR of the triggers listed below. The triggers fire based on a set of criteria summarized in the trigger name following the ATLAS trigger naming convention. The list includes generic single low-p_T muon triggers such as EF_mu6 and EF_mu15, single high-p_T muons & jets triggers such as EF_mu24_j65_a4tchad and the specialized J/ψ trigger EF_mu6_Trk_Jpsi_loose.

- EF_mu24_j65_a4tchad_EFxe40_tclcw
- EF_mu4T_j65_a4tchad_xe60_tclcw_loose
- EF_mu24_j65_a4tchad
- EF_mu18_tight_e7_medium1
- EF_mu4T_j65_a4tchad_xe70_tclcw_veryloose
- EF_mu24_j65_a4tchad_EFxe60_tclcw
- EF_mu24_tight_b35_mediumEF_j35_a4tchad
- EF_mu20i_tight_g5_loose_TauMass
- EF_mu6_Trk_Jpsi_loose
- EF_mu24i_tight
- EF_mu24i_tight_MuonEF

- EF_mu24i_tight_MG
- EF_mu24i_tight_l2muonSA
- EF_mu24_tight_3j35_a4tchad
- EF_mu24_g20vh_loose
- EF_mu40_MSonly_barrel_tight
- EF_mu50_MSonly_barrel_tight
- EF_mu24_tight_EFxe40
- EF_mu24_tight_L2StarB
- EF_mu18_medium
- EF_mu24_medium
- EF_mu24_tight
- EF_mu24_tight_MuonEF
- EF_mu24_tight_MG
- EF_mu24_tight_L2StarC
- EF_mu36_tight
- EF_mu40_tight
- EF_mu20it_tight
- EF_mu24_g20vh_medium
- EF_mu18_2g10_medium
- EF_mu24_muCombTag_NoEF_tight
- EF_mu10i_loose_g12Tvh_medium
- EF_mu10i_loose_g12Tvh_medium_TauMass

- EF_mu18_2g10_loose
- EF_mu10i_g10_medium_TauMass
- EF_mu20i_tight_g5_medium_TauMass
- EF_mu24_tight_3j45_a4tchad
- EF_mu24_tight_4j45_a4tchad
- EF_mu24_tight_4j35_a4tchad
- EF_mu4T
- EF_mu6
- EF_mu15
- EF_mu40_slow_tight
- EF_mu60_slow_tight1
- EF_mu22_IDTrkNoCut_tight
- EF_mu8_4j45_a4tchad_L2FS
- EF_mu6_Trk_Jpsi_loose_L2StarB
- EF_mu6_Trk_Jpsi_loose_L2StarA
- EF_mu24_j65_a4tchad_EFxe40wMu_tclcw
- EF_mu24_j65_a4tchad_EFxe60wMu_tclcw
- EF_mu6T_2b55_medium_2j55_a4tchad_L1J20_matched
- EF_mu24i_tight_muFast
- EF_mu4T_L2StarB
- EF_mu6_L2StarB
- EF_mu15_vbf_L1TAU8_MU10

Appendix E

List of Muon Combined Performance cuts

The following selection is the recommended track-based quality criteria as defined by the muon combined performance group [111].

- Require a pixel b-layer hit on the muon EXCEPT where the extrapolated muon track passed an uninstrumented or dead area of the b-layer.
- Number of pixel hits + number of crossed dead pixel sensors > 0.
- Number of SCT hits + number of crossed dead SCT sensors > 4.
- Number of pixel holes + number of SCT holes < 3.
- A successful TRT extension where expected (i.e. in the η acceptance of the TRT). An unsuccessful extension corresponds to either no TRT hit associated, or a set of TRT hits associated as outliers. Let $N_{\text{TRT hits}}$ denote the number of TRT hits on the muon track, $N_{\text{TRT outliers}}$ the number of TRT outliers on the muon track, and $n = N_{\text{TRT hits}} + N_{\text{TRT outliers}}$:
  - **Case 1**: $0.1 < |\eta| < 1.9$. Require $n > 5$ and $N_{\text{TRT outliers}} < 0.9n$.
  - **Case 2**: $|\eta| \geq 0.1$ or $|\eta| \leq 1.9$. If $n > 5$, then require $N_{\text{TRT outliers}} < 0.9n$.

Bibliography

[1] J Blanco et al. "Measurement of the top quark pair production cross-section with ATLAS in pp collisions at $\sqrt{s} = 7$ TeV in the single-lepton channel using semileptonic b decays". In: ATLAS-COM-CONF-2012-056 (Mar. 2012).

[2] Lyndon Evans and Philip Bryant. "LHC Machine". In: *Journal of Instrumentation* 3.08 (2008), S08001. ISSN: 1748-0221. DOI: http://dx.doi.org/10.1088/1748-0221/3/08/S08001. URL: http://iopscience.iop.org/1748-0221/3/08/S08001.

[3] D. Griffiths. *Introduction to Elementary Particles*. 2nd, Revised Edition edition. John Wiley & Sons, Inc, Aug. 2008. ISBN: 9783-527-4060-1-2.

[4] Anderson, P. "Plasmons, Gauge Invariance, and Mass". In: *Phys. Rev.* 130 (1 Apr. 1963), pp. 439–442. DOI: http://dx.doi.org/10.1103/PhysRev.130.439. URL: http://link.aps.org/doi/10.1103/PhysRev.130.439.

[5] F. Englert and R. Brout. "Broken Symmetry and the Mass of Gauge Vector Mesons". In: *Phys. Rev. Lett.* 13 (9 Aug. 1964), pp. 321–323. DOI: http://dx.doi.org/10.1103/PhysRevLett.13.321. URL: http://link.aps.org/doi/10.1103/PhysRevLett.13.321.

[6] G. Guralnik, C. Hagen, and T. Kibble. "Global Conservation Laws and Massless Particles". In: *Phys. Rev. Lett.* 13 (20 Nov. 1964), pp. 585–587. DOI: http://dx.doi.org/10.1103/PhysRevLett.13.585. URL: http://link.aps.org/doi/10.1103/PhysRevLett.13.585.

[7] Peter Higgs. "Broken Symmetries and the Masses of Gauge Bosons". In: *Phys. Rev. Lett.* 13 (16 Oct. 1964), pp. 508–509. DOI: http://dx.doi.org/10.1103/PhysRevLett.13.508. URL: http://link.aps.org/doi/10.1103/PhysRevLett.13.508.

[8] Gerard 't Hooft. "Renormalizable Lagrangians for Massive Yang-Mills Fields". In: *Nucl.Phys.* B35 (1971), pp. 167–188. DOI: http://dx.doi.org/10.1016/0550-3213(71)90139-8.

[9] The ATLAS Collaboration. "The ATLAS Experiment at the CERN Large Hadron Collider". In: *Journal of Instrumentation* 3.08 (2008), S08003. URL: http://stacks.iop.org/1748-0221/3/i=08/a=S08003.

[10] The CMS Collaboration et al. "The CMS experiment at the CERN LHC". In: *Journal of Instrumentation* 3.08 (2008), S08004. URL: http://stacks.iop.org/1748-0221/3/i=08/a=S08004.

[11] The ATLAS Collaboration. "Observation of a new particle in the search for the Standard Model Higgs boson with the ATLAS detector at the LHC". In: *Physics Letters B* 716.1 (2012), pp. 1–29.

[12] The CMS Collaboration. "Observation of a new boson at a mass of 125 GeV with the CMS experiment at the LHC". In: *Physics Letters B* 716.1 (2012), pp. 30–61.

[13] Hill, Christopher T. "Topcolor assisted technicolor". In: *Phys.Lett.* B345 (1995), pp. 483–489. DOI: http://dx.doi.org/10.1016/0370-2693(94)01660-5. arXiv: hep-ph/9411426 [hep-ph].

[14] Kenneth Lane and Estia Eichten. "Natural topcolor-assisted technicolor". In: *Physics Letters B* 352.3–4 (1995), pp. 382–387. ISSN: 0370-2693. DOI: http://dx.doi.org/10.1016/0370-2693(95)00482-Z. URL: http://www.sciencedirect.com/science/article/pii/037026939500482Z.

[15] Harris, Robert M. and Supriya Jain. "Cross sections for leptophobic topcolor Z' decaying to top–antitop". In: *The European Physical Journal C* 72.7 (2012). ISSN: 1434-6044. DOI: http://dx.doi.org/10.1140/epjc/s10052-012-2072-4.

[16] B. Odom et al. "New Measurement of the Electron Magnetic Moment Using a One-Electron Quantum Cyclotron". In: *Physical Review Letters* 97 (3 July 2006), p. 030801. DOI: http://dx.doi.org/10.1103/PhysRevLett.97.030801. URL: http://link.aps.org/doi/10.1103/PhysRevLett.97.030801.

[17] P. A. R. Ade et al. "Overview of products and scientific results". In: *Planck 2013 results* I (2013).

[18] D. H. Perkins. *Introduction to High Energy Physics*. Cambridge University Pres, 2000.

[19] J. Beringer et al. "Review of Particle Physics". In: *Physical Review D* 86 (1 July 2012), p. 010001. DOI: http://dx.doi.org/10.1103/PhysRevD.86.010001. URL: http://link.aps.org/doi/10.1103/PhysRevD.86.010001.

[20] N. Cabibbo. "Unitary Symmetry and Leptonic Decays". In: *Physical Review Letters* 10 (12 June 1963), pp. 531–533.

[21] M. Kobayashi and T. Maskawa. "CP-Violation in the Renormalizable Theory of Weak Interaction". In: *Progress of Theoretical Physics* 49.2 (1973), pp. 652–657.

[22] L. L. Chau and W. Y. Keung. "Comments on the Parametrization of the Kobayashi-Maskawa Matrix". In: *Physical Review Letters* 53 (1984), p. 1802. DOI: http://dx.doi.org/10.1103/PhysRevLett.53.1802.

[23] L. Wolfenstein. "Parametrization of the Kobayashi-Maskawa Matrix". In: *Physical Review Letters* 51 (21 Nov. 1983), pp. 1945–1947. DOI: http://dx.doi.org/10.1103/PhysRevLett.51.1945.

[24] K. Marathe. *Topics in Physical Mathematics*. Springer, 2010. ISBN: 9781-8488-293-8-1. URL: http://books.google.co.uk/books?id=Rf7pqYEb4PQC.

[25] C. S. Wu et al. "Experimental Test of Parity Conservation in Beta Decay". In: *Physical Review* 105.4 (1957), pp. 1413–1415. DOI: http://dx.doi.org/10.1103/PhysRev.105.1413. URL: http://link.aps.org/doi/10.1103/PhysRev.105.1413.

[26] J. H. Christenson et al. "Evidence for the 2π Decay of the K_2^0 Meson". In: *Physical Review Letters* 13.4 (1964), pp. 138–140. DOI: http://dx.doi.org/10.1103/PhysRevLett.13.138. URL: http://link.aps.org/doi/10.1103/PhysRevLett.13.138.

[27] S. Weinberg. "A Model of Leptons". In: *Physical Review Letters* 19.21 (1967), pp. 1264–1266. DOI: http://dx.doi.org/10.1103/PhysRevLett.19.1264. URL: http://link.aps.org/doi/10.1103/PhysRevLett.19.1264.

[28] S.L. Glashow. "Partial-symmetries of weak interactions". In: *Nuclear Physics* 22.4 (1961), pp. 579–588. ISSN: 0029-5582. DOI: http://dx.doi.org/10.1016/0029-5582(61)90469-2. URL: http://www.sciencedirect.com/science/article/pii/0029558261904692.

[29] A. Salam. "Weak and Electromagnetic Interactions". In: *Conference Proceedings* C680519 (1968), pp. 367–377.

[30] G. Arnison et al. "Experimental observation of isolated large transverse energy electrons with associated missing energy at $\sqrt{s} = 540\,\text{GeV}$". In: *Physics Letters B* 122.1 (1983), pp. 103–116. ISSN: 0370-2693.

[31] The ATLAS Collaboration. "Measurement of the Higgs boson mass from the $H \to \gamma\gamma$ and $H \to ZZ^* \to 4\ell$ channels with the ATLAS detector using 25 fb^{-1} of pp collision data". In: (2014).

[32] S. W. Herb et al. "Observation of a Dimuon Resonance at $9.5\,\text{GeV}$ in $400\,\text{GeV}$ Proton-Nucleus Collisions". In: *Physical Review Letters* 39 (5 Aug. 1977), pp. 252–255. DOI: http://dx.doi.org/10.1103/PhysRevLett.39.252. URL: http://link.aps.org/doi/10.1103/PhysRevLett.39.252.

[33] G. Montagna et al. "The Top quark and the Higgs boson mass from LEP SLC and CDF data". In: *Physics Letters* B335 (1994), pp. 484–489. DOI: http://dx.doi.org/10.1016/0370-2693(94)90381-6. arXiv: hep-ph/9407246 [hep-ph].

[34] CDF Collaboration. "Observation of Top Quark Production in $p\bar{p}$ Collisions with the Collider Detector at Fermilab". In: *Physical Review Letters* 74 (14 Apr. 1995), pp. 2626–2631. DOI: http://dx.doi.org/10.1103/PhysRevLett.74.2626.

[35] D0 Collaboration. "Search for High Mass Top Quark Production in $p\bar{p}$ Collisions at $\sqrt{s} = 1.8\,\text{TeV}$". In: *Physical Review Letters* 74 (13 Mar. 1995), pp. 2422–2426. DOI: http://dx.doi.org/10.1103/PhysRevLett.74.2422.

[36] The ATLAS Collaboration. *Search for top pair candidate events in ATLAS at $\sqrt{s}$=7 TeV*. ATLAS-CONF-2010-063. Geneva: CERN, July 2010.

[37] The CMS Collaboration. *Selection of top-like events in the dilepton and lepton-plus-Jets channels in early 7 TeV Data*. CMS-PAS-TOP-10-004. Geneva: CERN, 2010.

[38] J. H. Kuhn, A. Reiter, and P. M. Zerwas. "Z Decays to Top Quarks". In: *Nuclear Physics* B272 (1986), p. 560. DOI: http://dx.doi.org/10.1016/0550-3213(86)90235-X.

[39] M. Aliev et al. "HATHOR: HAdronic Top and Heavy quarks crOss section calculatoR". In: *Computer Physics Communications* 182 (2011), pp. 1034–1046. DOI: http://dx.doi.org/10.1016/j.cpc.2010.12.040.

[40] Matteo Cacciari et al. "Top-pair production at hadron colliders with next-to-next-to-leading logarithmic soft-gluon resummation". In: *arXiv:1111.5869 [hep-ph]* (2011). URL: http://arxiv.org/abs/1111.5869.

[41] *Combination of ATLAS and CMS top quark pair cross section measurements in the $e\mu$ final state using proton-proton collisions at $\sqrt{s}$= 8 TeV*. Tech. rep. ATLAS-CONF-2014-054. Geneva: CERN, Sept. 2014.

[42] N. Kidonakis. "NNLL threshold resummation for top-pair and single-top production". In: *Phys.Part.Nucl.* 45.4 (2014), pp. 714–722. DOI: http://dx.doi.org/10.1134/S1063779614040091.

[43] John M. Campbell and Francesco Tramontano. "Next-to-leading order corrections to Wt production and decay". In: *Nucl.Phys.* B726 (2005), pp. 109–130. DOI: http://dx.doi.org/10.1016/j.nuclphysb.2005.08.015. arXiv: hep-ph/0506289 [hep-ph].

[44] Nikolaos Kidonakis. "Two-loop soft anomalous dimensions for single top quark associated production with a W- or H-". In: *Phys.Rev.* D82 (2010), p. 054018. DOI: http://dx.doi.org/10.1103/PhysRevD.82.054018. arXiv: 1005.4451 [hep-ph].

[45] S. Zhu. "Next-to-leading order QCD corrections to $bg \to tW$ at the CERN Large Hadron Collider". In: *Phys.Lett.* B524 (2002), pp. 283–288. DOI: http://dx.doi.org/10.1016/S0370-2693(01)01404-6.

[46] Walter T. Giele, Stephane Keller, and Eric Laenen. "QCD corrections to W boson plus heavy quark production at the Tevatron". In: *Phys.Lett.* B372 (1996), pp. 141–149. DOI: http://dx.doi.org/10.1016/0370-2693(96)00078-0. arXiv: hep-ph/9511449 [hep-ph].

[47] The ATLAS Collaboration. *Summary plots from the ATLAS Top physics group*. https://atlas.web.cern.ch/Atlas/GROUPS/PHYSICS/CombinedSummaryPlots/TOP/. Accessed: 06/06/2014. 2013.

[48] The ATLAS and CMS Collaborations. *Combination of ATLAS and CMS results on the mass of the top-quark using up to $4.9\,\text{fb}^{-1}$ of $\sqrt{s} = 7\,\text{TeV}$ LHC data*. ATLAS-CONF-2013-102. Geneva: CERN, Sept. 2013.

[49] The ATLAS Collaboration. "Search for $t\bar{t}$ resonances in the lepton plus jets final state with ATLAS using 4.7 fb^{-1} of pp collisions at $\sqrt{s} = 7$ TeV". In: *Physical Reviews* D88.1

(2013), p. 012004. DOI: http://dx.doi.org/10.1103/PhysRevD.88.012004. arXiv: 2.2756 [hep-ex].

[50] Agashe, Kaustubh and Alexander Belyaev and Tadas Krupovnickas and Gilad Perez and Joseph Virzi. "CERN LHC signals from warped extra dimensions". In: *Phys. Rev. D* 77 (1 Jan. 2008), p. 015003. DOI: http://dx.doi.org/10.1103/PhysRevD.77.015003. URL: %7Bhttp://link.aps.org/doi/10.1103/PhysRevD.77.015003%7D.

[51] Lillie, Ben and Jing Shu and Timothy M. P. Tait. "Kaluza-Klein gluons as a diagnostic of warped models". In: *Phys. Rev. D* 76 (11 Dec. 2007), p. 115016. DOI: http://dx.doi.org/10.1103/PhysRevD.76.115016.

[52] Agashe, Kaustubh and Hooman Davoudiasl and Gilad Perez and Amarjit Soni. "Warped gravitons at the CERN LHC and beyond". In: *Phys. Rev. D* 76 (3 Aug. 2007), p. 036006. DOI: http://dx.doi.org/10.1103/PhysRevD.76.036006.

[53] Abdelhak Djouadi and Grégory Moreau and Ritesh K. Singh. "Kaluza–Klein excitations of gauge bosons at the {LHC}". In: *Nuclear Physics B* 797.1–2 (2008), pp. 1–26. ISSN: 0550-3213. DOI: http://dx.doi.org/10.1016/j.nuclphysb.2007.12.024.

[54] Ben Lillie and Lisa Randall and Lian-Tao Wang. "The Bulk RS KK-gluon at the LHC". In: *Journal of High Energy Physics* 2007.09 (2007), p. 074.

[55] The ALICE Collaboration. "The ALICE experiment at the CERN LHC". In: *Journal of Instrumentation* 3.08 (2008), S08002. URL: http://stacks.iop.org/1748-0221/3/i=08/a=S08002.

[56] The LHCb Collaboration et al. "The LHCb Detector at the LHC". In: *Journal of Instrumentation* 3.08 (2008), S08005. URL: http://stacks.iop.org/1748-0221/3/i=08/a=S08005.

[57] Fabienne Marcastel. "CERN's Accelerator Complex. La chaîne des accélérateurs du CERN". In: (Oct. 2013). General Photo.

[58] The ATLAS Collaboration. *Luminosity Public Result*. https://twiki.cern.ch/twiki/bin/view/AtlasPublic/LuminosityPublicResults. Accessed: 2014-06-20. 2013.

[59] Georges Aad et al. "Luminosity Determination in pp Collisions at $\sqrt{s} = 7$ TeV Using the ATLAS Detector at the LHC". In: *Eur.Phys.J.* C71 (2011), p. 1630. DOI: http://dx.doi.org/10.1140/epjc/s10052-011-1630-5. eprint: 1101.2185.

[60] Manfred Kochsief Michael Glaser. *Handbook of Metrology*. Wiley-VCH, 2010.

[61] The ATLAS Collaboration. "Expected Performance of the ATLAS Experiment - Detector, Trigger and Physics". In: CERN-OPEN-2008-020 (Dec. 2008).

[62] G. Aad et al. "Commissioning of the ATLAS Muon Spectrometer with Cosmic Rays". In: *Eur.Phys.J.* C70 (2010), pp. 875–916. DOI: http://dx.doi.org/10.1140/epjc/s10052-010-1415-2. eprint: 1006.4384.

[63] Diego Casadei. *Estimating the trigger efficiency. A Tutorial*. http://indico.cern.ch/event/109265/contribution/4/material/slides/2.pdf. Slides from the ATLAS Statistics Forum, Accessed: 03/12/14. Oct. 2010.

[64] The ATLAS Collaboration. "The ATLAS Simulation Infrastructure". In: *European Physics Journal C* 70 (2010), pp. 823–874. DOI: http://dx.doi.org/10.1140/epjc/s10052-010-1429-9.

[65] Dobbs, M.A. and S. Frixione and Eric Laenen and K. Tollefson and H. Baer and others. "Les Houches guidebook to Monte Carlo generators for hadron collider physics". In: (2004), pp. 411–459. eprint: hep-ph/0403045.

[66] A. Schaelicke et al. "Event Generator for Particle Production in High-Energy Collisions". In: *Progress in Particle and Nuclear Physics* 53.1 (2004), pp. 329–338. ISSN: 01466410. DOI: http://dx.doi.org/10.1016/j.ppnp.2004.02.031. URL: http://arxiv.org/abs/hep-ph/0311270.

[67] S. Agostinelli et al. "GEANT4—a simulation toolkit". In: *Nuclear Instruments and Methods in Physics Research Section A* 506.3 (2003), pp. 250–303. ISSN: 0168-9002. DOI: http://dx.doi.org/10.1016/S0168-9002(03)01368-8.

[68] The ATLAS Collaboration. "Electron reconstruction and identification efficiency measurements with the ATLAS detector using the 2011 LHC proton-proton collision data". In: *European Physical Journal C* 74.7 (2014), p. 2941. DOI: http://dx.doi.org/10.1140/epjc/s10052-014-2941-0.

[69] The ATLAS Collaboration. "Electron efficiency measurements with the ATLAS detector using the 2012 LHC proton-proton collision data". In: ATLAS-CONF-2014-032 (June 2014).

[70] B. Resende. "Muon identification algorithms in ATLAS". In: ATL-PHYS-PROC-2009-113 (Sept. 2009).

[71] R Nicolaidou et al. "Muon identification procedure for the ATLAS detector at the LHC using Muonboy reconstruction package and tests of its performance using cosmic rays and single beam data". In: *Journal of Physics: Conference Series* 219.3 (2010), p. 032052. URL: http://stacks.iop.org/1742-6596/219/i=3/a=032052.

[72] D. Adams et al. "Track reconstruction in the ATLAS Muon Spectrometer with MOORE 007". In: ATL-SOFT-2003-007, ATL-COM-SOFT-2003-008, CERN-ATL-SOFT-2003-007 (2003).

[73] Tarem, S. and Z. Tarem and N. Panikashvili and O. Belkind. "MuGirl – Muon identification in the ATLAS detector from the inside out". In: *Nuclear Science Symposium Conference Record, 2006. IEEE*. Vol. 1. Oct. 2006, pp. 617–621. DOI: http://dx.doi.org/10.1109/NSSMIC.2006.356230.

[74] M. Cacciari, G. P. Salam, and G. Soyez. "The Anti-k(t) jet clustering algorithm". In: *JHEP* 2008.04 (2008), p. 063. DOI: http://dx.doi.org/10.1088/1126-6708/2008/04/063.

[75] M. Cacciari and G. P. Salam. "Dispelling the N^3 myth for the k_t jet-finder". In: *Physics Letters B* 641 (2006), pp. 57–61. DOI: http://dx.doi.org/10.1016/j.physletb.2006.08.037.

[76] W. Bhimji et al. "Jet energy measurement with the ATLAS detector in proton-proton collisions at $\sqrt{s} = 7$ TeV". In: *European Physical Journal C* 73 (2013). CERN-PH-EP-2011-191, p. 2304. DOI: http://dx.doi.org/10.1140/epjc/s10052-013-2304-2.

[77] Georges Aad et al. "Jet energy measurement with the ATLAS detector in proton-proton collisions at $\sqrt{s} = 7$ TeV". In: *European Physics Journal C* 73 (2013), p. 2304. DOI: http://dx.doi.org/10.1140/epjc/s10052-013-2304-2.

[78] The ATLAS Collaboration. "Commissioning of the ATLAS high-performance b-tagging algorithms in the 7 TeV collision data". In: ATLAS-CONF-2011-102 (July 2011).

[79] The ATLAS Collaboration. "Performance of the ATLAS Secondary Vertex b-tagging Algorithm in 7 TeV Collision Data". In: ATLAS-CONF-2010-042 (July 2010).

[80] The ATLAS Collaboration. "Measurement of the Mistag Rate with $5\,\text{fb}^{-1}$ of data collected by the ATLAS Detector". In: ATLAS-CONF-2012-040 (Mar. 2012).

[81] The ATLAS Collaboration. *Measurement of the b-tag Efficiency in a Sample of Jets Containing Muons with 5 fb^{-1} of Data from the ATLAS Detector*. ATLAS-CONF-2012-043. CERN, 2012.

[82] The ATLAS Collaboration. "Performance of Missing Transverse Momentum Reconstruction in Proton-Proton Collisions at 7 TeV with ATLAS". In: *Eur.Phys.J.* C72 (2012), p. 1844. DOI: http://dx.doi.org/10.1140/epjc/s10052-011-1844-6. eprint: 1108.5602.

[83] M. Rose. "Development of a new Soft Muon Tagger for the Identification of b quarks, applied to a Top Quark Pair Production Cross Section Measurement, using the ATLAS Detector at CERN". PhD thesis. Royal Holloway, University of London, 2013.

[84] Fuenfundachtzig. *CrystalBallFunction*. http://commons.wikimedia.org/wiki/File:CrystalBallFunction.svg. Accessed: 28/07/2014. 2010.

[85] A. Salzburger. *Track and Vertex Reconstruction*. https://indico.fnal.gov/getFile.py/access?sessionId=12&resId=0&materialId=0&confId=8769. Slides from HCP Summer School 2014. Aug. 2014.

[86] S. Frixione and B. R. Webber. "Matching NLO QCD computations and parton shower simulations". In: *JHEP* 2002.06 (2002), p. 029. DOI: http://dx.doi.org/10.1088/1126-6708/2002/06/029.

[87] S. Frixione, P. Nason, and B. R. Webber. "Matching NLO QCD and parton showers in heavy flavor production". In: *JHEP* 2003.08 (2003), p. 007. DOI: http://dx.doi.org/10.1088/1126-6708/2003/08/007. arXiv: hep-ph/0305252 [hep-ph].

[88] G. Corcella et al. "HERWIG 6.5: an event generator for Hadron Emission Reactions With Interfering Gluons (including supersymmetric processes)". In: *Journal of High Energy Physics* 2001.01 (2001), pp. 010–010. ISSN: 1029-8479. DOI: http://dx.doi.org/10.1088/1126-6708/2001/01/010. URL: http://arxiv.org/abs/hep-ph/0011363.

[89] J. M. Butterworth, J. R. Forshaw, and M. H. Seymour. "Multiparton interactions in photoproduction at HERA". In: *Zeitschrift für Physik* C72 (1996), pp. 637–646. DOI: http://dx.doi.org/10.1007/s002880050286.

[90] M. L. Mangano et al. "ALPGEN, a generator for hard multiparton processes in hadronic collisions". In: *JHEP* 2003.07 (2003), p. 001.

[91] B. P. Kersevan and E. Richter-Was. "The Monte Carlo event generator AcerMC versions 2.0 to 3.8 with interfaces to PYTHIA 6.4, HERWIG 6.5 and ARIADNE 4.1". In: *Computer Physics Communications* 184 (2013), pp. 919–985. DOI: http://dx.doi.org/10.1016/j.cpc.2012.10.032.

[92] Torbjorn Sjostrand, Stephen Mrenna, and Peter Skands. "PYTHIA 6.4 Physics and Manual". In: *Journal of High Energy Physics* 2006.05 (2006), pp. 026–026. ISSN: 1029-8479. DOI: http://dx.doi.org/10.1088/1126-6708/2006/05/026. URL: http://arxiv.org/abs/hep-ph/0603175.

[93] The ATLAS Collaboration. "Background studies for top-pair production in lepton plus jets final states in $\sqrt{s} = 7$ TeV ATLAS data". In: ATLAS-CONF-2010-087, ATLAS-COM-CONF-2010-085 (2010).

[94] ATLAS Collaboration. "Measurement of the charge asymmetry in top quark pair production in pp collisions at $\sqrt{s} = 7$ TeV using the ATLAS detector". In: *The European Physical Journal C* 72.6 (2012). ISSN: 1434-6044, 1434-6052. DOI: http://dx.doi.org/10.1140/epjc/s10052-012-2039-5. URL: http://arxiv.org/abs/1203.4211.

[95] C.-H. Kom and W. J. Stirling. "Charge asymmetry in W + jets production at the LHC". In: *European Physical Journal C* 69.1-2 (2010), pp. 67–73. DOI: http://dx.doi.org/10.1140/epjc/s10052-010-1353-z.

[96] P. Nason. "A New method for combining NLO QCD with shower Monte Carlo algorithms". In: *JHEP* 2004.11 (2004), p. 040. DOI: http://dx.doi.org/10.1088/1126-6708/2004/11/040. arXiv: hep-ph/0409146 [hep-ph].

[97] S. Frixione, P. Nason, and C. Oleari. "Matching NLO QCD computations with Parton Shower simulations: the POWHEG method". In: *JHEP* 2007 (2007), p. 070. DOI: http://dx.doi.org/10.1088/1126-6708/2007/11/070. arXiv: 0709.2092 [hep-ph].

[98] The ATLAS Collaboration. "Measurement of $t\bar{t}$ production with a veto on additional central jet activity in pp collisions at $\sqrt{s} = 7$ TeV using the ATLAS detector". In: *European Physical Journal C* 72 (2012), p. 2043. DOI: http://dx.doi.org/10.1140/epjc/s10052-012-2043-9. arXiv: 1203.5015 [hep-ex].

[99] The ATLAS Collaboration. "Measurement of dijet production with a veto on additional central jet activity in pp collisions at $\sqrt{s} = 7$ TeV using the ATLAS detector". In: *JHEP* 2011.09 (2011), p. 053. DOI: http://dx.doi.org/10.1007/JHEP09(2011)053.

[100] H.-L. Lai et al. "New parton distributions for collider physics". In: *Physical Reviews D* 82 (2010), p. 074024. DOI: http://dx.doi.org/10.1103/PhysRevD.82.074024.

[101] A. D. Martin et al. "Uncertainties on alpha(S) in global PDF analyses and implications for predicted hadronic cross sections". In: *European Physical Journal C* 64 (2009), pp. 653–680. DOI: http://dx.doi.org/10.1140/epjc/s10052-009-1164-2.

[102] R. D. Ball et al. "Impact of Heavy Quark Masses on Parton Distributions and LHC Phenomenology". In: *Nuclear Physics B* 849 (2011), pp. 296–363. DOI: http://dx.doi.org/10.1016/j.nuclphysb.2011.03.021. arXiv: 1101.1300 [hep-ph].

[103] The ATLAS Collaboration. "Measurement of the top quark pair production cross-section with ATLAS in the single lepton channel". In: *Physics Letters B* 711.3–4 (2012), pp. 244–263. ISSN: 0370-2693. DOI: http://dx.doi.org/10.1016/j.physletb.2012.03.083. URL: http://www.sciencedirect.com/science/article/pii/S0370269312003814.

[104] "A search for $t\bar{t}$ resonances in the lepton plus jets final state with ATLAS using $14\,\text{fb}^{-1}$ of pp collisions at $\sqrt{s} = 8$ TeV". In: ATLAS-CONF-2013-052 (May 2013). Not published in the proceedings.

[105] S. Chatrchyan et al. "Search for Z' resonances decaying to $t\bar{t}$ in dilepton+jets final states in pp collisions at $\sqrt{s} = 7$ TeV". In: *Physical Reviews D* 87 (7 Apr. 2013), p. 072002. DOI: http://dx.doi.org/10.1103/PhysRevD.87.072002. URL: http://link.aps.org/doi/10.1103/PhysRevD.87.072002.

[106] S. Chatrchyan et al. "Search for anomalous $t\bar{t}$ production in the highly-boosted all-hadronic final state". In: *JHEP* 2012.9 (2012), p. 29. DOI: http://dx.doi.org/10.1007/JHEP09(2012)029. eprint: 1204.2488.

[107] The CMS Collaboration. "Search for $t\bar{t}$ resonances in semileptonic final state". In: CMS-PAS-B2G-12-006 (2013).

[108] J. Pumplin et al. "New generation of parton distributions with uncertainties from global QCD analysis". In: *JHEP* 2002.07 (2002), p. 012. DOI: http://dx.doi.org/10.1088/1126-6708/2002/07/012.

[109] The ALTAS Collaboration. "b-tagging in dense environments". In: ATL-PHYS-PUB-2014-014 (Aug. 2014). URL: https://cds.cern.ch/record/1750682.

[110] The ATLAS Collaboration. "Electron performance measurements with the ATLAS detector using the 2010 LHC proton-proton collision data". In: *European Physical Journal C* 72 (2012), p. 1909. DOI: http://dx.doi.org/10.1140/epjc/s10052-012-1909-1. eprint: 1110.3174.

[111] "Preliminary results on the muon reconstruction efficiency, momentum resolution, and momentum scale in ATLAS 2012 pp collision data". In: ATLAS-CONF-2013-088 (Aug. 2013).